

Fakultät für Medizin der Technischen Universität München
Experimentelle und Molekulare Kinderkardiologie am Deutschen Herzzentrum München

The role of the essential NADPH oxidase subunit p22phox and reactive oxygen species in
the pathogenesis of hypoxia-induced pulmonary hypertension

Benjamin Siegfried Trautz

Vollständiger Abdruck der von der Fakultät für Medizin
der Technischen Universität München zur Erlangung des akademischen Grades
eines Doktors der Medizinischen Wissenschaft (Dr. med. sci.)
genehmigten Dissertation.

Vorsitzender:

apl. Prof. Dr. Klaus-Peter Janssen

Prüfende der Dissertation:

1. Prof. Dr. Agnes Görlach

2. Prof. Dr. Hendrik Sager

Die Dissertation wurde am 28.05.2020 bei der Technischen Universität München
eingereicht und durch die Fakultät für Medizin am 07.10.2020 angenommen.

Acknowledgment

First of all, I would like to thank my supervisor, Prof. Agnes Görlach for giving me the opportunity to do this research project under her guidance at Deutsches Herzzentrum München.

I want to thank Dr. Andreas Petry and Dr. Zuwen Zhang for their overall support and constant help during the experimental and writing phase.

To my colleagues from the laboratory, I want to especially thank Frederick Vogel, Anna Knirsch, Linda Li and Katharina Hochkogler, for our constructive discussions and for offering a helping hand whenever needed.

Last but not least I want to thank my parents and my brother for their invaluable support and love throughout my life. And I would like to thank my partner and my friends for their constant encouragement and understanding. Thank you for always being there for me.

INDEX

1. Summary	7
2. Introduction	8
2.1. Pulmonary hypertension	8
2.1.1. Clinical classification	8
2.1.2. Clinical appearance and diagnosis	10
2.1.3. Pathogenesis of pulmonary hypertension.....	11
2.1.4. Therapeutic approaches towards pulmonary hypertension	13
2.1.5. Animal models of pulmonary hypertension	13
2.1.5.1. Chronic hypoxia	14
2.1.5.2. Monocrotaline injury	14
2.1.5.3. Sugen 5416	15
2.2. Hypoxia and HIFs	16
2.3. Reactive oxygen species and NADPH oxidases	17
2.3.1. Generation of reactive oxygen species.....	17
2.3.2. NADPH oxidases	18
2.3.3. Further sources of reactive oxygen species.....	21
2.4. Reactive oxygen species and disease	22
2.5. Aim of the study	23
3. Material und Methods	24
3.1. Material	24
3.1.1. Equipment	24
3.1.2. Chemicals.....	26
3.1.3. Cell culture reagents.....	28
3.1.4. Consumables	29
3.1.5. Enzymes	30
3.1.6. Kits and ready-to-use reagents	30
3.1.7. Antibodies	31
3.1.8. Primers	32
3.1.8.1. Primers for genotyping	32
3.1.8.2. Primers for qPCR.....	32
3.1.9. Buffers and solutions.....	33
3.1.9.1. Western blot solutions	35
3.1.9.2. Solutions for histology.....	36
3.1.10. Software	37

3.2. Methods	38
3.2.1. Molecular biological methods.....	38
3.2.1.1. DNA analysis and genotyping.....	38
3.2.1.1.1. DNA extraction from animal tissue.....	38
3.2.1.1.2. PCR.....	38
3.2.1.1.3. Electrophoresis.....	40
3.2.1.2. Tissue and cell lysis.....	40
3.2.1.2.1. Sand grinding.....	41
3.2.1.2.2. Automatic homogenizer.....	41
3.2.1.2.3. Tip sonicator.....	41
3.2.1.2.4. Cell lysis.....	42
3.2.1.3. RNA-related methods.....	42
3.2.1.3.1. RNA isolation and quantification.....	42
3.2.1.3.2. RT-PCR.....	43
3.2.1.3.3. qPCR.....	44
3.2.1.4. Protein-related methods.....	46
3.2.1.4.1. Protein quantification.....	46
3.2.1.4.1.1. Dot blot.....	46
3.2.1.4.1.2. Bradford assay.....	46
3.2.1.4.2. Western blot analysis.....	47
3.2.1.5. Measurement of reactive oxygen species.....	50
3.2.2. Animal experiments.....	50
3.2.2.1. Mouse lines.....	51
3.2.2.1.1. NMF333 mice.....	51
3.2.2.1.2. NOX1-K.O. mice.....	52
3.2.2.2. Mouse keeping.....	54
3.2.2.3. Hypoxia.....	54
3.2.2.4. Haemodynamic measurements.....	55
3.2.2.4.1. Pressure transducer system.....	56
3.2.2.4.2. Anaesthesia system.....	56
3.2.2.4.3. Haemodynamic measurement procedure.....	56
3.2.2.5. Euthanasia and organ collection.....	58
3.2.2.5.1. Special preparation of the heart.....	58
3.2.2.5.2. Special preparation of the lung.....	59
3.2.2.6. Evaluation of the animal experiments.....	59
3.2.2.6.1. Haemodynamic measurements.....	59
3.2.2.6.2. Fulton index.....	60
3.2.2.7. In-vivo Matrigel angiogenesis assay.....	60
3.2.2.8. Blood.....	60
3.2.2.8.1. Routine blood work.....	61
3.2.2.8.2. Purification of mononuclear cells.....	61

3.2.2.9.	Measurement of metabolic activity	62
3.2.3.	Cell culture	63
3.2.3.1.	Cell lines	63
3.2.3.1.3.	HMEC-1	63
3.2.3.1.4.	Mouse embryonic stem cells	64
3.2.3.2.	Hypoxia cell culture.....	65
3.2.3.3.	Transfection of HMEC-1.....	65
3.2.4.	Histology	66
3.2.4.1.	Standard procedures	66
3.2.4.1.1.	Formalin fixation and paraffin embedding.....	66
3.2.4.1.2.	Cryo fixation	69
3.2.4.2.	Staining.....	70
3.2.4.2.1.	Chemical staining.....	70
3.2.4.2.2.	Immunostaining.....	71
3.2.4.2.3.	Wheat germ agglutinin staining	74
3.2.4.3.	Evaluation.....	74
3.2.4.3.1.	Heart – H&E staining.....	75
3.2.4.3.2.	Heart – WGA staining.....	75
3.2.4.3.3.	Lung – α -smooth muscle actin staining	75
3.2.4.3.4.	Lung – KI67/ α -smooth muscle actin double staining	76
3.3.	Statistics	76
4.	Results	77
4.1.	Link between hypoxia and p22phox.....	77
4.1.1.	Regulation of p22phox gene expression by hypoxia	77
4.1.2.	Regulation of p22phox protein levels by hypoxia	78
4.2.	Characterization of the NMF333 mouse line.....	79
4.2.1.	P22phox gene expression in NMF333 mice	79
4.2.2.	P22phox protein levels in NMF333 mice	80
4.2.3.	ROS production in mononuclear cells	81
4.2.4.	Vessel-forming capacity in wildtype and NMF333 mice	81
4.3.	Effect of chronic hypoxia on NMF333 and WT mice	83
4.3.1.	Blood parameters.....	83
4.3.2.	P22phox gene expression in hypoxic mice	84
4.3.3.	P22phox protein levels in hypoxic mice	84
4.3.4.	Haemodynamic measurements in normoxic and hypoxia-stimulated mice.....	85
4.3.5.	Cardiac responses to chronic hypoxia.....	88
4.3.5.1.	Determination of ventricular mass	88
4.3.5.2.	Ventricular wall diameter	89
4.3.5.3.	Size determination of cardiomyocytes	91

4.3.5.4.	Hypertrophy-linked gene expression of the right ventricle	92
4.3.6.	Pulmonary vascular responses to chronic hypoxia	93
4.3.6.1.	Pulmonary vascular remodeling	93
4.3.6.2.	Pulmonary vascular proliferation	95
4.3.7.	Pulmonary and cardiac ¹⁸ F-FDG uptake	96
4.4.	Regulation of HIF1α	98
4.4.1.	Regulation of HIF1 α gene expression by hypoxia	98
4.4.2.	Regulation of HIF1 α protein levels by hypoxia	99
4.4.3.	HIF1 α gene expression in hypoxic mice	99
4.4.4.	HIF1 α protein levels in hypoxic mice	100
4.4.5.	Effect of p22phox silencing on HIF1 target gene expression	101
4.5.	NOX1-K.O. mice and chronic hypoxia	103
4.5.1.	Haemodynamic measurements	103
4.5.2.	Cardiac response to chronic hypoxia	104
4.5.3.	Pulmonary vascular remodelling	104
5.	Discussion	106
5.1.	Regulation of p22phox	106
5.1.1.	Hypoxic regulation of p22phox	106
5.1.2.	Y121H mutation and p22phox expression	107
5.2.	P22phox and HIF	108
5.3.	Effects of p22phox	111
5.3.1.	P22phox promotes angiogenesis	111
5.3.2.	P22phox and pulmonary hypertension	112
5.3.3.	P22phox and pulmonary vascular remodelling	115
5.3.4.	P22phox and right ventricular hypertrophy	116
5.4.	Role of NOX1 in hypoxia-induced pulmonary hypertension	118
5.5.	Limitations of the study	119
5.6.	Conclusion	119
6.	References	121
7.	Appendix	135
7.1.	List of figures	135
7.2.	List of abbreviations	137

1. Summary

Pulmonary hypertension (PH) is a progressive disease with no curative treatment so far, characterized by pulmonary vascular remodelling, elevated pulmonary arterial pressure and right ventricular hypertrophy.

Since reactive oxygen species (ROS) might contribute to PH, the role of NADPH oxidases in the pathogenesis of PH was analysed. We found that loss of the NADPH oxidase subunit p22phox protected mice against the development of hypoxia-induced PH.

Thus, NADPH oxidases may serve as targets for new therapeutic approaches.

Pulmonale Hypertonie (PH) ist eine progressive, bisher unheilbare Erkrankung, die mit pulmonal-vaskulärem Remodeling, erhöhtem pulmonal-arteriellem Druck und rechtsventrikulärer Hypertrophie einhergeht.

Da reaktive Sauerstoffspezies (ROS) eine Rolle bei PH spielen könnten, wurde der Einfluss der NADPH Oxidasen in der Pathogenese der PH untersucht. Es konnte gezeigt werden, dass der Verlust der NADPH Oxidase Untereinheit p22phox vor der Entwicklung von Hypoxie-induzierter PH in der Maus schützte. Dies könnte ein Ansatz für neue Therapien sein.

2. Introduction

2.1. Pulmonary hypertension

The clinical picture of pulmonary hypertension (PH) is defined as constantly elevated mean pulmonary artery pressure ≥ 25 mmHg. The elevated pressure leads to consecutive right ventricular hypertrophy, ultimately resulting in death due to right heart failure. Thereby, primary forms must be distinguished from secondary forms due to other diseases. Thus, the term of pulmonary hypertension covers a wide range of different entities. Generally, about one in a hundred adults suffer from PH [84]. The molecular mechanisms and pathways leading to this incurable disease are still not completely understood [189].

2.1.1. Clinical classification

In 2013, the currently valid “Nice”-classification of pulmonary hypertension was established based upon the former clinical classification from 1998. Hereby, the symptom of pulmonary hypertension is categorized into 5 big groups based upon similar pathophysiological mechanisms, underlying aetiologies and therapeutic approaches: (1) pulmonary arterial hypertension (PAH), (2) pulmonary hypertension due to left heart disease, (3) pulmonary hypertension due to lung disease or hypoxia, (4) chronic thromboembolic pulmonary hypertension (CTEPH) and (5) pulmonary hypertension with unclear multifactorial mechanisms (Tab. 1) [168]. Whereas the syndrome of pulmonary hypertension is found quite commonly, affecting between 1% to 10% of the global population, the occurrence of the different types varies tremendously [84]. Group 1 and 4 must be counted to the more rare occurring forms. An incidence of 3.9 per 1 million and a prevalence of 25.9 per 1 million adults for Group 1 PH were reported for Germany in 2014 [86]. PAH is a progressive disease, characterized by increased pulmonary arterial pressure due to vascular remodelling. Untreated, the prognosis is poor with a median survival time of about three years [169]. For CTEPH an incidence of 4 per 1 million adults was measured in the same period of time [85]. With 34.2% of total cases the most common type of PH is found in group 2 – due to left heart diseases [208]. Systemic hypertension and left heart malfunctions lead to an insufficient cardiac output. The result is a dilatation of the left atrium and a backlog of venous blood into the lung. 73% of patients suffering from left heart failure with reduced

ejection fraction were diagnosed with PH [14]. Group 3 – PH related to lung diseases – is responsible for another 30% of PH cases, making it the second largest group [208]. Group 5 PH encloses a heterogenous group of haematological, systemic and metabolic disorders. The true incidence and prevalence of PH in context of these diseases is unknown and difficult to determine. However, PH is assumed to be a common complication and associated with an unfavourable prognosis [103].

Table 1 Clinical classification of pulmonary hypertension (PH)

1.	Pulmonary arterial hypertension (PAH)
1.1	Idiopathic PAH
1.2	Heritable PAH
1.2.1	BMPR2
1.2.2	ALK-1, ENG, SMAD9, CAV1, KCNK3
1.2.3	Unknown
1.3	Drug and toxin induced
1.4	Associated with:
1.4.1	Connective tissue disease
1.4.2	HIV infection
1.4.3	Portal hypertension
1.4.4	Congenital heart disease
1.4.5	Schistosomiasis
1'	Pulmonary veno-occlusive disease and/ or pulmonary capillary hemangiomatosis
1''	Persistent pulmonary hypertension of the new-born (PPHN)
2.	Pulmonary hypertension due to left heart disease
2.1	Left ventricular systolic dysfunction
2.2	Left ventricular diastolic dysfunction
2.3	Valvular disease
2.4	Congenital/ acquired left heart inflow/ outflow tract obstruction and congenital cardiomyopathy
3.	Pulmonary hypertension due to lung disease and/ or hypoxia
3.1	Chronic obstructive pulmonary disease
3.2	Interstitial lung disease
3.3	Other pulmonary disease with mixed restrictive and obstructive pattern
3.4	Sleep-disorder breathing
3.5	Alveolar hypoventilation disorders
3.6	Chronic exposure to high altitude
3.7	Developmental lung disease
4.	Chronic thromboembolic pulmonary hypertension (CTEPH)
5.	Pulmonary hypertension with unclear multifactorial mechanisms
5.1	Hematologic disorders: chronic haemolytic anaemia , myeloproliferative disorders, splenectomy
5.2	Systemic disorders: sarcoidosis, pulmonary histiocytosis, lymphangioleiomyomatosis
5.3	Metabolic disorders: glycogen storage disease, Gaucher disease, thyroid disorders
5.4	Others: tumoral obstruction, fibrosing mediastinitis, chronic renal failure, segmental PH

*5th WSPH Nice 2013, Main modifications to the previous Dana Point classification are in **bold**. BMPR = bone morphogenic protein receptor type II; CAV1 = caveolin-; ENG = endoglin; HIV = human immunodeficiency virus; PAH = pulmonary arterial hypertension. Modified after [168].*

2.1.2. Clinical appearance and diagnosis

Generally seen, patients with PH suffer from exercise dyspnoea, shortness of breath, fatigue and exhaustion [84]. Furthermore, symptoms of right heart failure like oedema, hepatomegaly, ascites and jugular vein pulsation can come along, depending on the severity of the disease [68]. However, these symptoms are merely unspecific, thus the final diagnosis is often made with delay. Echocardiography can already visualize signs of right heart overload. Nevertheless, right heart catheterization (RHC) remains the gold standard and is required to confirm the diagnosis of pulmonary hypertension, to assess the severity of the disease and to collect information for correct subcategorization [68, 84]. Besides the mean arterial pressure, especially the pulmonary artery wedge pressure (PAWP) is necessary to distinguish post capillary hypertension (group 2 PH) and precapillary hypertension (group 1, 3,4,5 PH) [14]. During RHC a small balloon is inflated to occlude a small pulmonary vessel. In this state of blocked blood flow the pressure transducer, which is installed behind the balloon, measures the post occlusive pressure (= wedge pressure). These pressure values represent the venous side up to the left atrium, which do not exceed 15 mmHg under normal conditions. In group 2 PH, which is caused by a backlog of blood, this wedge pressure is measured greater than 15 mmHg (Tab. 2). Moreover, imaging techniques like MRI and CT as well as blood parameters are used to complete the picture.

The diagnosis of pulmonary arterial hypertension requires a mean pulmonary arterial pressure of greater than 25 mmHg, a normal pulmonary artery wedge pressure and a pulmonary vascular resistance of greater than 3 WU (Tab. 2). Furthermore, cardiac failure, structural lung diseases, chronic thromboembolic as well as other systemic diseases must be excluded. Besides, typical histopathological findings include plexiform lesions and a hypertrophic and fibrotic vasculopathy of the distal arteries and arterioles [130, 173].

Table 2 Haemodynamic classification of pulmonary hypertension

Group	Recommended terminology	Old used terminology	mPAP (mmHg)	PAWP (mmHg)	DPG (mmHG)	PVR (WU)
1	Precapillary PH		≥25	≤15		≥3
3,4,5	Precapillary PH		≥25	≤15		
2	Isolated postcapillary PH	Pulmonary venous hypertension	≥25	>15	<7	≤3
	Combined pre- and postcapillary hypertension	Mixed PH	≥25	>15	≥7	>3

mPAP – mean pulmonary arterial pressure; PAWP – pulmonary artery wedge pressure; DPG – diastolic pulmonary vascular pressure gradient; PVR – pulmonary vascular resistance; WU – wood units. Adapted after [14].

2.1.3. Pathogenesis of pulmonary hypertension

Although the exact mechanisms leading to the development of PAH are not discovered so far, a disturbed balance between vasoconstrictive and dilatative factors is assumed. Three main pathways are known to contribute to the control of vascular resistance and tone: the nitric oxide pathway, the prostacyclin pathway and the endothelin pathway [136] (Fig. 1).

The short living radical nitric oxide ($\cdot\text{NO}$) is produced in endothelial cells by the endothelial nitric oxide synthase (eNOS) from the amino acid L-arginine. However, it unfolds its effects in the adjacent smooth muscle cells of the media, where $\cdot\text{NO}$ diffuses and increases the cGMP concentration leading to relaxation of the smooth muscle cells with consecutive vasodilation [167]. Finally, cGMP is broken down by the enzyme phosphodiesterase type 5. Indeed, already early studies could show reduced levels of eNOS in lung arteries from patients suffering from PAH [65]. On the other hand, studies found conflicting data with no changes or even elevated levels of eNOS [133, 212].

Prostacyclin or prostaglandin-I₂ (PGI₂) belong to the group of eicosanoids, which are produced by cyclooxygenase (COX) from arachidonic acid (AA) in endothelial cells. They

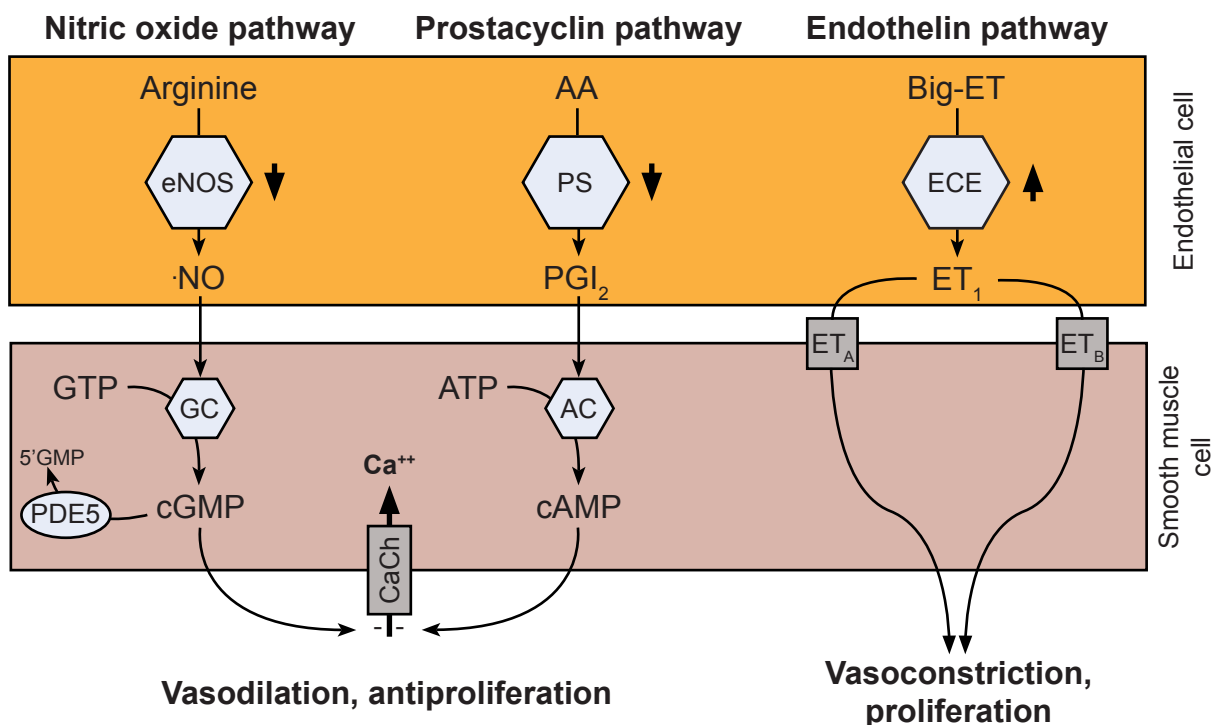


Figure 1 Pathways involved in the development of pulmonary hypertension

Illustration of the three known pathways, contributing to the development and targeted in the therapy of PAH. AA – arachidonic acid; eNOS – endothelial nitric oxide synthase; $\cdot\text{NO}$ – nitric oxide; PGI₂ – Prostacycline, PS – prostacyclin synthase; Big-ET – Pro-endothelin; ECE – endothelin converting enzyme; ET₁ – endothelin 1; GTP – guanylate triphosphate; cGMP – cyclic guanylate monophosphate; GC – guanylate cyclase; PDE5 – phosphodiesterase-5; ATP – adenosine triphosphate; AC – adenylate cyclase; cAMP cyclic adenosine monophosphate; CaCh – Calcium channel; ET_A and ET_B receptor. Adapted from [136].

promote strong protective cardiovascular and antithrombotic effects [106]. Similar to NO, they act in the smooth muscle cells, where they activate the G-protein coupled prostacyclin receptor (IP) and the intracellular peroxisome proliferator-activated receptor (PPAR). Among others, the cAMP concentration is increased, leading to vessel dilation [56]. Interestingly, the prostaglandin thromboxane mediates a completely opposite response including vasoconstriction and stimulation of thrombocytes via the thromboxane receptor (TP). Furthermore, for other types of prostaglandins like PGE₂, the response merely depends on the expressed receptor subtype. While activation of prostaglandin E₂ receptor 2 (EP₂), prostaglandin E₂ receptor 4 (EP₄) and prostaglandin D₂ receptor (DP₂) leads to an IP-receptor like response [139], prostaglandin E₂ receptor 1 (EP₁) and prostaglandin E₂ receptor 3 (EP₃) stimulation will again result in vasoconstriction [146], making the prostaglandins an extremely heterogenous and complex group of mediators.

Finally, the peptide hormone endothelin-1 (ET1) serves as one of the most potent vasoconstrictive substances in the body and is the strongest beyond the three existing endothelin isoforms. Endothelin-1 is cleaved from the precursor peptides preproendothelin and Big-ET-1 by the endothelin-converting-enzyme (ECE) in endothelial cells [32]. ET1 was found to be highly expressed in lung, with expression levels up to five times higher compared to other tissues [135]. In patients suffering from PAH, even higher levels of ET1 were found in pulmonary muscular arteries as well as in plexiform lesions [66]. The released peptide binds to G-protein coupled endothelin receptors ET_A and ET_B expressed by the adjacent smooth muscle cells. Both receptors mediate vasoconstriction via a phospholipase C dependent increase of the intracellular Ca²⁺ concentration and promote proliferation [32]. However, ET_B receptors are found on endothelial cells, too. There, they lead to a stimulation of NO release, as though limiting the vasoconstrictive effect. Moreover, the ET1-ET_B receptor-complex is internalized by endothelial cells, thus playing an important role in the clearance of ET1 [153].

Beside these pathways, hypoxic states lead to vasoconstriction, too – a condition known as Euler-Liljestrand mechanism or hypoxic pulmonary vasoconstriction (HPV) [171]. The rationale behind this physiologic reaction is to enhance the ventilation/ perfusion ratio by redirecting the blood flow from poorly-ventilated to well-ventilated lung areas and thus reducing the right-to-left shunt. Thereby, the pulmonary vasculature presents a unique reaction, since vessels of the systemic circulation dilate at hypoxia [1]. Although this mechanism is beneficial in terms of regional hypoxia, chronic and global hypoxia will eventually lead to the development of pulmonary hypertension [53]. The hypoxic pulmonary

vasoconstriction has already been described in 1946, however, the exact cellular mechanisms remain unclear [1, 171]. It is assumed, that increased shear stress due to prolonged vasoconstriction occurs at the endothelium, triggering endothelial dysfunction with consecutive vascular remodelling [198].

2.1.4. Therapeutic approaches towards pulmonary hypertension

Due to intense research in the past time, significant advances have been reached in the treatment of PAH in the context of clinical progression, symptomatic status and survival rate (86,4% vs. 68% after one year, 72,9% vs. 48% after three years) [110]. Nevertheless, PAH remains a chronic and life limiting disease that cannot be cured so far [96].

The therapeutic strategies that are used to cope with the disease mainly target the key points in these three pathways. In general, vasodilation pathways are enhanced while vasoconstriction is impeded. The used substances include endothelin receptor antagonists, hindering the activation of ET receptors and the ET1-dependent vasoconstriction [9]. Phosphodiesterase-5 inhibitors like sildenafil impede the breakdown of the second messenger cGMP from the NO pathway, while soluble guanylate cyclase stimulators increase NO production [174]. Targeting the third pathway, synthetic prostacyclin analogues can be administered. Moreover, calcium channel blockers have a vasodilatory effect and are used with success in the treatment of systemic hypertension and coronary heart disease. However, only a small proportion of PAH patients (about 5%) is reported to respond to the treatment with calcium channel blockers [137]. Nowadays, an individual combination of these different substance groups is used as standard approach in the therapy of PAH. Besides, new agents including mitochondrial modulators, anti-inflammatory, anti-proliferative and immunomodulatory therapies are currently tested [9].

2.1.5. Animal models of pulmonary hypertension

In order to study the complex pathogenesis of diseases and to find treatment approaches, animal models are unfortunately still necessary. Cell culture is a good method to minimise the number of required animals, however, this approach cannot depict the complex interactions between organ systems. In context of PAH, two classical animal models have often been described: the chronic hypoxia model and the inflammatory monocrotaline induced PAH model [177]. Usually rodents like mice and rats are used as experimental

animals in PAH research although they might react in a different way to the various stimuli compared to humans. Thus, it remains challenging to find a model that resemble human PAH closest [35]. Therefore, models of severe PAH were sought, for example the combined Sugen 5416 (SU-5416) and hypoxia model [185].

2.1.5.1. Chronic hypoxia

Exposure to chronic hypo- or normobaric hypoxia is a widely used model which leads to a reliable response within a few weeks, although the degree of the response depends on several parameters. First, the age of the animals is a critical factor, since younger animals are more susceptible to the stimulus [176]. Second, the response varies strongly between species. Calves are strongly affected and develop serious vascular remodelling. Mice on the other hand react fairly weak with a characteristic, but mild muscularization of previously non-muscularized small vessels. Right ventricular hypertrophy occurs, but a progression to right heart failure is usually not observed in mice. Furthermore, the effect is reversible under normoxic conditions [177]. Among rats, which already react stronger to chronic hypoxia by themselves compared to mice, the strain of fawn-hooded rats develops an atypically strong response [143]. The response in all species include an infiltration of the arterial wall with mononuclear cells, proportionally to the grade of vascular remodelling [23, 177]. Beyond the common models of PAH, the hypoxia model is one of the mildest in rodents. The characteristic plexiform lesions found in human PAH are not present. Therefore, it is probably not the model which reproduces the picture of human PAH closest [26]. Seen from its trigger stimulus, it is more connected to group 3 PH [35]. Nevertheless, it can provide valuable insight in mechanisms of vascular remodelling and might lead the way to new therapeutic approaches [198].

2.1.5.2. Monocrotaline injury

The monocrotaline (MCT) injury model is mainly used in rats. MCT is an alkaloid that causes an injury of the endothelium in the lung vasculature after cytochrome-dependent metabolism in the liver. The endothelial injury, caused by apoptosis of endothelial cells, goes along with inflammation and vasculitis, serving as trigger for the vascular remodelling processes [124]. Histological features include a narrowing of the lumen and medial hypertrophy, leading to a strong increase in pulmonary arterial pressure with consecutive

RV failure [177]. It is assumed to represent the group 1 PAH in a better way than the chronic hypoxia model [124]. Interestingly, it is reported, that both arteries and veins are affected by remodelling, an important difference compared to human PAH [209]. Besides, MCT is toxic for kidney and liver [209]. It is likely, that MCT causes an acute injury in a broad spectrum of small vessels in different organs, instead of a specific pulmonary vascular reaction. However, a new study reported no extrapulmonary effects after a low dose MCT administration [115]. Another important point is that the effect varies strongly between the species. In mice for instance, an early phase acute lung injury was observed, resulting in a mild lung fibrosis, but without the development of significant pulmonary hypertension [52].

2.1.5.3. Sugden 5416

The Sugden 5416 hypoxia model combines the administration of the VEGF receptor antagonist with exposure to chronic hypoxia. The model was established primarily in rats, but in contrast to the MCT-model, a SU-5416 model could be established in mice, too [33]. However, there remain distinct differences between the species. Already the application of SU-5416 alone leads to mild vascular remodelling and pulmonary hypertension in rats. In combination with chronic hypoxia, rats develop severe pulmonary hypertension and vascular remodelling with angio-obliterative lesions that resemble human plexiform lesions very closely, the hallmark of the human PAH [185]. They were even described as indistinguishable from human plexiform lesions [2]. Moreover, no extrapulmonary effects of the VEGF-inhibitor were observed. Interestingly, the disease worsened even after rats returned to normoxia [177]. Mice on the other hand develop aggravated PH and RV hypertrophy compared to hypoxia alone, which do not progress when mice are returned to normoxia. The hypertrophy even resolves, whereas rats partially die from right heart failure [188, 197]. Furthermore, the characteristic angio-obliterative lesions found in rats were not observed in mice [197].

The Sugden 5416 hypoxia model in rats mimics many features of the human PAH (including the formation of plexiform lesions and right heart failure) and thus can be connected to group 1 and 3 PH [124]. The Sugden 5416 mouse model, however, seems to be inferior in these points. Therefore, the search for the optimal model for human PAH will go on [197].

2.2. Hypoxia and HIFs

Hypoxia describes a state of reduced oxygen supply at tissue level. Thereby, generalized and local hypoxia can be distinguished. In contrast, hypoxaemia refers to a reduced oxygen concentration of the arterial blood [161]. Generalized hypoxia is mostly connected to an arterial hypoxemia occurring for example in high altitudes or in patients suffering from chronic lung diseases. Local hypoxia on the other hand is related to a reduced organ perfusion as we find for instance in coronary artery disease and myocardial infarction or peripheral artery disease. The normal alveolar partial pressure for oxygen is age dependent and ranges between 100 and 82 mmHg. Thereby the partial pressure at the mitochondrial level remains only 5 to 20 mmHg [117]. Hypoxia can be classified into 4 main groups: ischemic or stagnant hypoxia (reduced blood flow), hypoxic hypoxia (reduced arterial oxygen concentration), anaemic hypoxia (reduced blood volume) and histotoxic hypoxia (toxin-mediated impairment of cellular respiration) [24].

The mechanisms of the organism to cope with hypoxic conditions are mainly directed by HIF – the family of hypoxia-inducible factors. The functional transcription factor HIF is a heterodimer. The activation is regulated via the labile α -subunit that exists in three paralogues, HIF1 α , HIF2 α and HIF3 α . Among the three paralogues, HIF1 α is the prototype and most extensively studied [73]. The β -subunit, also referred to as ARNT (aryl hydrocarbon receptor nuclear translocator), is constitutively expressed and dimerizes with all three α -subunits. However, a paralogue of ARNT, ARNT2 was described, too, although its exact function remains to be elucidated [80, 127].

Under normoxic conditions, the α -subunit is hydroxylated by proline-hydroxylase 2 (PHD-2), which leads to binding of the von Hippel-Lindau protein (pVHL), which is part of the E3 ubiquitin ligase complex [154]. Therefore, binding of pVHL results in ubiquitination with consecutive proteasomal degradation of the HIF α -subunit. PHD-2 belongs to the family of Fe(II) 2-oxoglutarate dependent dioxygenases, that require molecular oxygen and iron for reaction, thus serving as oxygen sensor [30, 217]. In states of reduced oxygen supply, HIF1 α is not hydroxylated and escapes the proteasomal degradation. The α - and β -subunit form the active heterodimer and are translocated to the nucleus, where they bind to hypoxia responsive elements (HRE), driving the transcription of downstream genes like VEGF and PGK-1 [44, 149]. In general, the HIF response primes the metabolism for survival at hypoxic conditions, allowing oxygen independent ATP production and promoting angiogenesis [113,

117]. The upregulation of EPO that stimulates erythrocyte production to improve the oxygen binding capacity is another example for a typical HIF response [77, 97]. Furthermore, HIF is crucial for development, since a complete loss of HIF1 α results in intrauterine death [111]. It was also demonstrated that HIF1 contributes to the development of pulmonary hypertension [213].

2.3. Reactive oxygen species and NADPH oxidases

Reactive oxygen species are a group of oxygen-derived and very reactive molecules. On the one hand, they include free oxygen radicals like the superoxide anion ($O_2^{\cdot-}$) and the hydroxyl radical ($\cdot OH$), which are characterized by one or more unpaired electrons [158]. On the other hand, reactive molecules like hydrogen peroxide (H_2O_2) are counted as ROS, too. They occur naturally as a side product in metabolism in particular in the respiratory chain. ROS can promote damaging effects to nearly all cellular components, including DNA, RNA, lipids, amino acids and proteins. Therefore, they must be neutralized by antioxidant agents [163]. Besides, ROS are an important tool in the fight against bacteria and microorganism. During the so-called respiratory burst, cells of the innate immune system produce large amounts of reactive oxygen species by NADPH oxidases with the purpose to kill invading microorganisms [108]. Moreover, ROS have been associated with cardiovascular diseases and the process of aging [67, 82]. But ROS are not always toxic. When produced at lower levels, especially $O_2^{\cdot-}$ and H_2O_2 serve as second messengers and modulators in a broad range of signalling pathways, including inflammation, proliferation, angiogenesis, migration, oxygen sensing and many more [22, 192].

2.3.1. Generation of reactive oxygen species

Starting with molecular oxygen (O_2), the different types of ROS can be ordered in a reaction sequence of electron transfer. Single electron reduction of molecular oxygen forms the superoxide anion $O_2^{\cdot-}$. By adding another electron, hydrogen peroxide (H_2O_2) emerges, by definition no free radical, since it harbours no unpaired electron. It therefore can pass the cellular membrane, whereas the polar radicals need anion channels [64, 147]. By adding another single electron the extremely reactive hydroxyl radical ($\cdot OH$) is formed. In a last step, the hydroxyl radical is reduced to water (H_2O) [118]. This sequence describes how the

different radicals emerge from another. In biological systems different enzymes partially modulate the reactions in order to scavenge and deactivate ROS (Fig. 2). The superoxide dismutase (SOD) catalyses the reaction of the superoxide anion to hydrogen peroxide. At this point the enzymes catalase and glutathione-peroxidase (GPx) enable a shortcut reaction to minimize the formation of the highly reactive hydroxyl radical. Thereby hydrogen peroxide is converted to water (the catalase reaction produces additionally molecular oxygen). The GPx requires glutathione (GSH) as reducing agent, which is restored in a subsequent reaction by the glutathione-reductase (GRx) [82]. However, hydroxyl radicals will occur in context of the Fenton reaction. Hereby, hydrogen peroxide oxidizes Fe(II) to Fe(III). Furthermore, the superoxide anion ($O_2^{\cdot-}$) can react with nitrogen monoxide ($\cdot NO$), predominantly produced by endothelial cells, to form peroxynitrite ($ONOO^-$). It thereby reduces the bioavailability of the vasodilatory $\cdot NO$ [192].

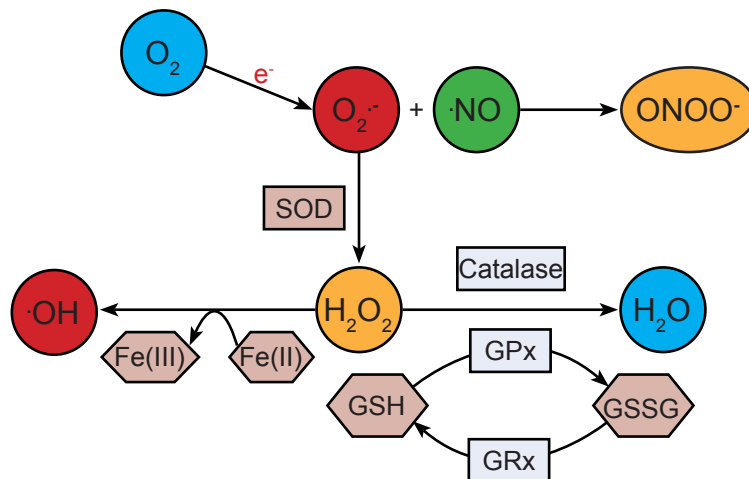


Figure 2 Reaction of ROS

Molecular oxygen (O_2) reacts to the superoxide anion radical ($O_2^{\cdot-}$) by single electron transfer. Superoxide scavenges nitrogen monoxide ($\cdot NO$), forming the radical peroxynitrite ($ONOO^-$). Superoxide dismutase (SOD) catalyses the reaction to hydrogen peroxide (H_2O_2). The reaction to water (H_2O) is catalysed by Catalase or glutathione peroxidase (GPx). Thereby glutathione (GSH) is used up and restored by the glutathione reductase (GRx) from glutathione disulphide (GSSG). However, H_2O_2 can be reduced to the hydroxyl radical ($\cdot OH$) by oxidizing iron (II) to iron (III).

2.3.2. NADPH oxidases

The family of NADPH oxidases covers a group of enzymes that produce superoxide anions from molecular oxygen. As the name already suggests, the coenzyme NADPH hereby serves as electron donor. They were first described in phagocytic cells and neutrophils, producing large amounts of ROS in the defence against invading bacteria. The membrane bound catalytic core cytochrome b558 is composed of two subunits, p22phox (encoded by the Cyba gene) and gp91phox (now termed NOX2, encoded by the Cybb gene), forming a

heterodimeric protein complex. Their activity is controlled by the regulatory cytosolic subunits p40phox, p47phox and p67phox, as well as the small GTP binding protein Rac [88]. Upon external stimuli, p47phox is phosphorylated and binds to the p22phox subunit of the cytochrome b558 complex after a change in conformation. Furthermore, GTP binding leads to activation of Rac, that triggers the translocation of p67phox to the NADPH oxidase complex [75]. Besides, the direct binding of active Rac is required for the electron transfer and full activation of ROS production [45] (Fig. 3). Mutations in any of the involved proteins can lead to a dysfunction of the superoxide production, resulting in a severe immunodeficiency called chronic granulomatous disease (CGD). Very recently, a newly found regulatory protein called “Eros” (essential for reactive oxygen species) was described to play an important role in cytochrome b558 stabilization and consecutively in an adequate respiratory burst [187]. By now, four more non-phagocytic gp91phox homologous were found and named NOXes. They are characterized by differences in their predominant tissue distribution and activity.

NOX1 was the first of the gp91phox homologous to be successfully cloned in 1991. It was found to be mainly expressed in colon epithelial cells, VSMCs and endothelial cells [22]. Furthermore, homologues of the regulatory subunits p47phox (NoxO1) and p67phox (NoxA1) were described in the interaction with NOX1. Thereby, the NoxO1 subunit serves as organizer and NoxA1 as enzyme activator [10], both are necessary for the full activation of NOX1. The NOX3 isoform is mainly expressed in the adult inner ear and involved in the

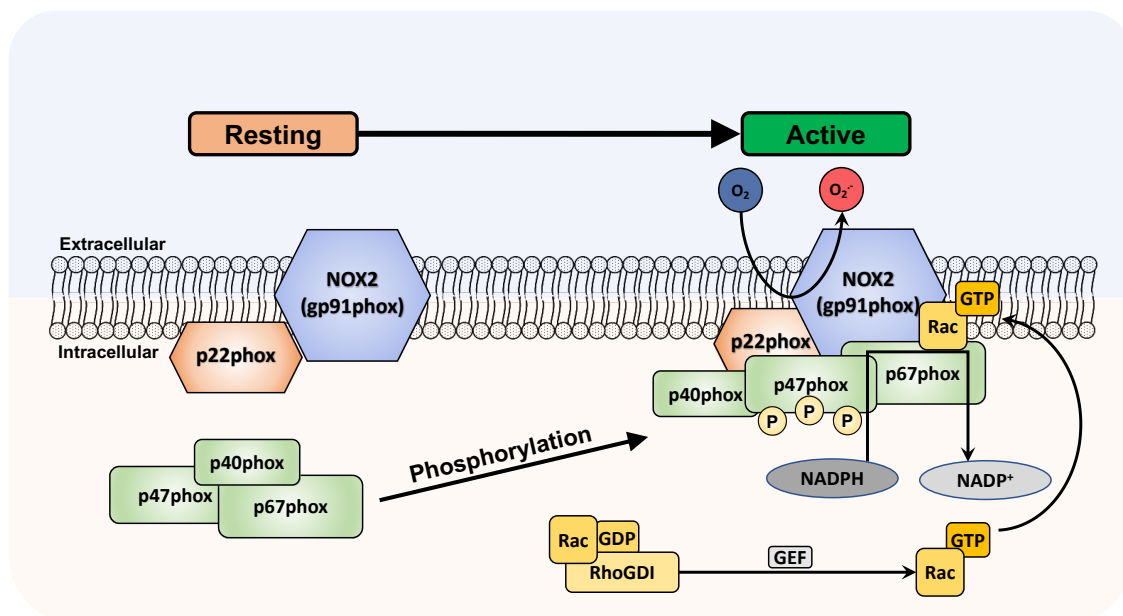


Figure 3 Structure of phagocyte NADPH oxidase complex

In resting cells, gp91phox and p22phox form the membrane-bound cytochrome b558 heterodimer. Upon stimulation and phosphorylation, the cytosolic subunits p40phox, p47phox, p67phox and Rac translocate to the membrane to form the activated NADPH complex (adapted after [150]).

otoconia and otolith formation, crystalline structures which are important for the sense of balance and gravity [122]. Overactivity of NOX3 is furthermore thought to be associated with an ototoxic hearing loss [11]. NOX4 was originally termed Renox, since it was discovered in large amounts in renal tissue. Beyond, it is expressed in many more cell types [22]. In contrast to the other NOXes it is said to be constitutively active without the necessity of regulatory subunits [132]. Beyond, it seems to be unique, since it was reported to be the only NOX to produce hydrogen peroxide instead of superoxide anions [8]. In 2001 the last homologue NOX5 has been discovered and described in lymphatic tissue, testis as well as in several cancer lines. However, it seems to be absent in rodents [22]. NOX1 to NOX4 all share the p22phox subunit, which is essential for forming and stabilizing cytochrome b558. Mutations of p22phox can lead to a severe autosomal form of CGD. Furthermore, p22phox is also absent in a X-linked form of CGD, which is caused by a mutation of the Cybb gene, thus showing the strong dependency of the heterodimer partners on each other [175]. All NOXes carry six transmembrane domains, as well as an intracellular NADPH and FAD binding domain. NOX5 on the other hand harbours additional four EF-hand domains, that have the ability to bind Ca^{2+} ions, putting NOX5 under the control of the intracellular calcium levels, instead of the cytosolic regulatory subunits [88] (Fig 4).

Beside the direct homologues, Duox1 and Duox2 containing a gp91phox-like domain complete the family of NADPH oxidases. In contrast to the NOXes, they are characterized by a further extracellular peroxidase domain and two Ca^{2+} -binding EF-hand motives similar

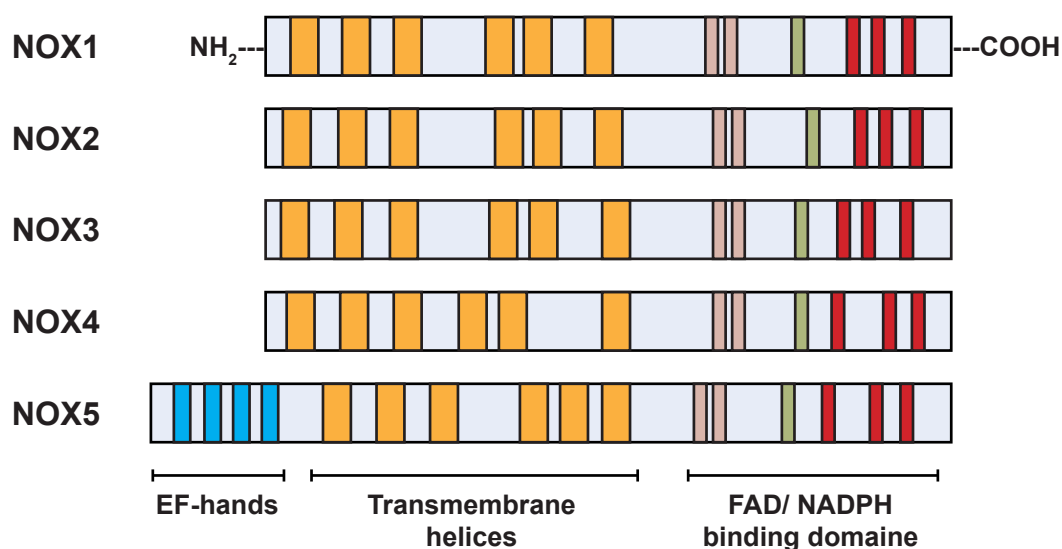


Figure 4 Schematic overview of the functional NOX domains

Structural overview of the different functional domains of the homologues NOX1 to NOX5. Similar domains are indicated by similar colours. Red – transmembrane domains; green – FAD binding domain; blue – NADPH binding domain; turquoise – Ca^{2+} binding domain (adapted after [150]).

to those known from NOX5. They are described to be mainly expressed in thyroid tissue, where hydrogen peroxide is used to oxidize iodide in context of the thyroid hormone synthesis [134].

2.3.3. Further sources of reactive oxygen species

As indicated above, reactive oxygen species are not only produced by NADPH oxidases but can also be generated as by-products during the metabolism. One important source of intracellular ROS is the respiratory chain of the mitochondria. Radicals are mainly formed at complex I and during the electron transfer from complex I and II to complex III. Hereby, the coenzyme ubiquinone is first reduced at complex I and II to ubiquinol, carrying two electrons. During the Q-cycle at complex III only one electron can be transferred from ubiquinol to cytochrome C at once, resulting in the intermediate formation of the semiquinone anion during the regeneration of ubiquinone. When reacting non-enzymatically with molecular oxygen, the semiquinone anion radical leads to the formation of superoxide in a rate proportional to the metabolic activity. Mitochondrial superoxide dismutase (SOD) and catalase intend to scavenge the free radicals immediately after formation [57]. Besides, further mitochondrial enzymes like α -ketoglutarate dehydrogenases, monoamine oxidases and glycerol phosphate dehydrogenases contribute to the mitochondrial ROS formation [152]. Therefore, mitochondria are counted as a main factor for the origin of intracellular oxidative stress [148].

Furthermore, ROS occur during the breakdown of wide range of metabolites, including the beta-oxidation of long chain fatty acids. These reactions take place in subcellular compartments, known as peroxisomes or microbodies, to shield the cell from the toxic side-products. As the name peroxisome already suggests, hydrogen peroxide is the main type of ROS produced. However, xanthine oxidases, which are important for the breakdown of purines to uric acid generate superoxide as well [20]. Moreover, the cytochrome P450 (CYP) oxidase family is another source of ROS. They are inter alia localized at the endoplasmatic reticulum of hepatocytes and are required for a wide range of metabolic reactions, including drug metabolism [152].

2.4. Reactive oxygen species and disease

In a healthy system, reactive oxygen species are held in a balanced range. A deviance in both directions can result in disease. Whereas a lack of ROS leads to immunodeficiency syndromes, an excess of ROS (also referred to as oxidative stress) contributes to a wide range of diseases including cardiovascular, neurodegenerative and chronic inflammatory diseases as well as cancer [21]. Oxidative stress can either be caused by an increased ROS production or by an impairment of the antioxidant systems [118]. However, the simple supplementation with antioxidant agents showed little or no effect in clinical studies, suggesting a complex pathophysiological context [21, 82].

Mechanistically most obvious, the direct damaging effect of ROS on DNA can result in mutations, thereby leading to the initiation, aggravation and progression of carcinogenesis [206]. Furthermore, high ROS levels appear to be associated with neurotoxicity and degeneration of neurons. Examples of associated diseases are Alzheimer's and Parkinson's disease. Hereby, NOX2 was found to be upregulated mainly in microglia [19, 172]. Moreover, increased NOX2 expression with elevated ROS levels were observed in psychiatric diseases, too. In this context, schizophrenia was extensively studied [204].

The family of cardiovascular diseases covers another big group of diseases associated with oxidative stress. Nearly all NOX homologues can be expressed by endothelial cells [21]. NOX2-produced ROS for instance were found to be involved in the vascular response to states of ischemia and reperfusion like coronary artery disease [121]. Although generally counted as metabolic disease, diabetes strongly affects the vasculature. It was demonstrated, that hyperglycaemia and advanced glycation end products result in increased ROS levels that lead to endothelial dysfunction and mediate diabetes-typical macro- and microangiopathic complications [58, 199]. It is assumed that mitochondrial dysfunction is the main cause for the hyperglycaemia-associated oxidative stress. However, an increase in NOX1 expression was found, too [74, 159]. Furthermore, hypertension is associated with oxidative stress [12]. Although the exact molecular mechanisms are not resolved to date, it is known, that ROS reduce the bioavailability of the vasodilatory nitric oxide ($\cdot\text{NO}$) [218]. Moreover, ROS serve as stimulus for proliferation and hypertrophy for vascular smooth muscle cells [21]. This connection is not limited to systemic hypertension, but is as well valid for pulmonary hypertension [210]. Precisely, there are multiple hints, that ROS are involved in the pathogenesis of group 1 pulmonary arterial hypertension (PAH). Upregulation of NOXes and xanthine oxidase, a decrease of $\cdot\text{NO}$ with an increase of reactive

nitric species, as well as enhanced eNOS uncoupling were observed in PAH [43, 182]. This is of special interest, since the exact pathophysiological mechanisms leading to this incurable disease are still not completely understood. The uncovering of more mechanistic details might be a chance for the development of new therapeutic approaches.

2.5. Aim of the study

The fatal disease pulmonary hypertension (PH) is characterized by elevated mean pulmonary artery pressure, vasoconstriction and structural remodelling of the pulmonary vasculature and right ventricular hypertrophy, which can ultimately lead to right ventricular failure. Although the number of affected patients is increasing, the exact pathomechanisms leading to PH are not fully resolved and a curative therapy is not available until now.

Reactive oxygen species (ROS) have been shown to act as signalling molecules in various vascular diseases. They are mainly generated by the family of NADPH oxidases, which share the essential p22phox subunit. Recent evidence suggests that ROS and NADPH oxidases are involved in the development of PH, although their exact role is unclear. The aim of this study is to elucidate the role of the essential NADPH oxidase subunit p22phox in the development of chronic hypoxia induced PH. Therefore, we used the NMF333 mouse strain, which harbors a Y121H point mutation in the Cyba gene coding for the p22phox subunit.

We hypothesized that:

- a) P22phox is regulated by hypoxia in vitro and in vivo.
- b) The Y121H point mutation in NMF333 mice leads to a loss of p22phox protein.
- c) P22phox deficient NMF333 mice are protected against the development of hypoxia induced PH, vascular remodelling and right ventricular hypertrophy.

3. Material und Methods

3.1. Material

3.1.1. Equipment

Item	Supplier
Adjustable pipettes	Gilson
Analytic balance	Sartorius
Anesthetizing box	Harvard Apparatus
Axiocam 506 color	Zeiss
Axioscope 2 plus	Zeiss
Cell culture bank, Hera safe	Heraeus
Capsulefuge PMC-060	TOMY Digital Biology
Centrifuge Biofuge pico	Heraeus
Centrifuge Biofuge fresco	Heraeus
Centrifuge Biofuge stratos	Heraeus
Cooling Plate CO P30	Medite
Counting Chamber, Neubauer	LaborOptik
Cryolys	Bertin Instruments
Cryotome CM 1850	Leica Biosystemds
Dehydration machine STP-120	Microm
Electrophoresis chamber	Bio-Rad
EPR e-scan	Bruker
Fluorescence Microscope IX83	Olympus
Fluovac System	Harvard Apparatus
Gas flowmeter	Harvard Apparatus
Gel Doc 2000	Bio-Rad
GeneAmp PCR System 9700	Applied Biosystems Life Technologies
GeneDisc heat sealer HS-01	Corbett/ Qiagen
Humidity sensor	Grainger
Hypoxia chambers	Ing. Humbs
Incubator Hera Cell	Heraeus

Incubator Kelvitron	Heraeus
Isoflurane vaporizer	Harvard Apparatus
ISOTEC pressure transducer head	Hugo Sachs - Harvard Apparatus
Lightsource Spectra X	Lumencor
Magnetic stirrer MR 3000	Heidolph Instruments
Microtome HM355S	Thermo Fischer Scientific
Microwave	Severin
Mini Protean 3 System	Bio-Rad
Mini Trans-Blot Cell	Bio-Rad
Nano Drop 2000c	Thermo Fischer Scientific
OpttMOS sCMOS camera	QImaging
OR-lamp Hanaulux 2003	Heraeus
Oxygen sensor	Grainger
pH meter, pH540 GLP	WTW
Pipette "Multipette plus"	Eppendorf
Pipette "Pipetman"	Gilson
Pipette "Pipetus"	Hirschmann Laborgeräte
Plate reader "Safire"	Tecan
Plate shaker Polymax 1040	Heidolph Instruments
Power supply, Power Pac 200	Bio-Rad
Power supply, Power Pac 300	Bio-Rad
Precellys 24 Tissue Homogenizer	Bertin Instruments
Racks	Tecniplast
Rodent anaesthesia circuit mask	Harvard Apparatus
Rotor Disc loading block	Corbett/ Qiagen
Rotor Gene 6000	Qiagen
Ruskin work station	I&L-Biosystems
Scanner WF-2630	Epson
Shaker Polymax 1040	Heidolph Instruments
Sonopuls ultrasonic homogenizer	Bandelin
Thermomixer Comfort	Eppendorf
Tissue embedding system AP 280-2	Microm
Tissue Float Bath 1052	GFL GmbH

Transducer Amplifier Modul-A	Hugo Sachs - Harvard Apparatus
Tube roller, RM-5	Assistant
Vortex-Genie 2	Scientific Industries
Warming plate	Witte & Sutor GmbH
X-ray cassettes IEC 60406	Kisker Biotech

3.1.2. Chemicals

Chemical/ Reagent	Supplier
Acetic acid	Carl Roth
Acetone	Sigma Aldrich
Agarose Standard	Carl Roth
Amido-black solution	Sigma Aldrich
Ammonium persulfate	Carl Roth
Bond Breaker	Thermo Fischer Scientific
Bromphenol blue	Sigma Aldrich
Bovine serum albumin (BSA)	AppliChem
CaCl ₂	Merck
1-hydroxy-methoxycarbonyl-2,2,5,5-tetramethylpyrrolidine hydrochloride (CMH)	Noxygen
Cumaric Acid	Sigma Aldrich
D-Glucose	Sigma Aldrich
DAB chromogen substrate	Dako
DAPI	Enzo
Desferroxamine (DES)	Sigma Aldrich
DMSO	Sigma Aldrich
Diethyldithiocarbamate (DETC)	Sigma Aldrich
Direct Red 80	Sigma Aldrich
Dithiothreitol (DTT)	GE Healthcare
EDTA	Carl Roth
EGTA	Carl Roth
Eosin G	Carl Roth

Ethanol Rotipuran	Carl Roth
Ethidium bromide	Carl Roth
Ficoll-Paque	Sigma Aldrich
Formalin 37%	Carl Roth
Glycerol	Carl Roth
β -Glycerophosphate	Sigma Aldrich
Glycine	Carl Roth
HIER buffer pH 6.0	Dako Agilent
HIER T-EDTA Buffer pH 9.0	Zytomed Systems
Hydrogen chloride	CLN
Hydrogen peroxide	Merck
Isopropanol	CLN
KCl	Merck
KH_2PO_4	Merck
Luminol	Sigma Aldrich
Matrigel matrix	BD Bioscience
MgSO_4	AppliChem
Mayer's Hemalaun	Carl Roth
Methanol	CLN
MgCl_2	Metabion
Na-HEPES	Sigma Aldrich
NaCl 0,9%	B. Braun
NaCl	Carl Roth
NaHCO_3	Merck
NaH_2PO_4	Sigma Aldrich
Na_2HPO_4	Sigma Aldrich
Naphthol blue black	Sigma Aldrich
Na_3VO_4	Merck
NEB buffer 3	New England Biolabs
Orange G	Sigma Aldrich
PBS Tablets	Life Technologies
PDGF	Calbiochem/ Merck
PMSF	Sigma Aldrich

Ponceau S	Carl Roth
Proteinase inhibitor mix complete	Roche
Quick-Load 100bp DNA Ladder	New England Biolabs
Rhodamine Labelled Wheat Germ Agglutinin	Biozol
Rotiphorese Gel	Carl Roth
Roti-Quant	Carl Roth
SDS	Carl Roth
Sodium acetate trihydrate	Carl Roth
Sodium pyrophosphate	Sigma Aldrich
Skim Milk Powder	Merck Millipore
TEMED	Carl Roth
TRIS "ultra"	Carl Roth
Triton X	Sigma Aldrich
Tween 20	Sigma Aldrich
Weigert's Hematoxylin A	Carl Roth
Weigert's Hematoxylin B	Carl Roth
X-ray fixing fluid	Tetenal
X-ray rapid developer	Tetenal
Xylene	Carl Roth

3.1.3. Cell culture reagents

Media and additives	Supplier
β -Mercaptoethanol	Carl Roth
DMEM	PAA/ GE Healthcare
Dulbecco's PBS	PAA/ GE Healthcare
EGF	Merck Millipore
Fetal calf serum	PAN-Biotech
Gelatine	PAN-Biotech
Hydrocortisone	PAN-Biotech
L-glutamine	PAN-Biotech
Leukaemia inhibitory factor	Merck Millipore

Lipofectamine 3000	Life Technologies
MCDB131 medium	PAN-Biotech
NEAA	PAN-Biotech
Penicillin	PAA/ GE Healthcare
Streptomycin	PAA/ GE Healthcare
Sodium pyruvate	PAN-Biotech
Trypsin 0,05%	PAA/ GE Healthcare

3.1.4. Consumables

Item	Supplier
Aluminium foil	Carl Roth
Cell culture dishes	Sarstedt
Cell lifter	SPL Lifesciences
Cover slides 24x50mm	Carl Roth
Cryo boxes	Kisker
Dako Pen S2002	Dako
Depilation cream	Veet, Reckitt Benckiser
Entellan	Merck
Eppendorf tubes	Eppendorf
Falcons	BD Bioscience
Gene-Disc 100	Qiagen
Gene-Disc heat sealing film	Qiagen
Glass capillaries	Sigma Aldrich
Gloves (latex)	Sempermed
Gloves (nitril)	Kimberly-Clark
Jelco 25G disposable cannula	Smiths Medical
Microtome blades S35	Feather
Mounting Medium	Dako
Multi-Adapter	Sarstedt
Nitrocellulose membrane Protran	GE Healthcare
Object slides Superfrost Plus	Gerhard Menzel GmbH
Paraffin	Merck

Pipette filter tips	Biozym Scientific
Pipettes, graduated, sterile	BD Bioscience
Pipette tips	Gilson
Reaction tubes, 4-stripe	Biozym Scientific
Reaction tubes, 8-stripe	Thermo Fischer Scientific
Rotilabo cassettes K116.1	Carl Roth
S-Monovette	Sarstedt
Soda lime	Draeger
Syringe, sterile	B. Braun
T75-flasks	Sarstedt
Tissue Tec O.C.T. Compound	Sakura Finetek
Whatman filtration paper 3mm	GE Healthcare
X-ray films Super RX	Fujifilm

3.1.5. Enzymes

Item	Supplier
Bsl I – RE	New England Biolabs
DNase 1	VWR LifeScience
Taq DNA Polymerase	Qiagen

3.1.6. Kits and ready-to-use reagents

Kits	Supplier
mi-Total RNA Miniprep Kit	Metabion
peqGOLD Total RNA Kit	Peqlab/ VWR
Mouse on Mouse Elite Peroxidase Kit	Vectorlabs
High-Capacity cDNA Reverse Transcription Kit	Applied Biosystems/ Life Technologies
SYBR Green “Quanta Perfecta”	Quanta Bioscience

3.1.7. Antibodies

Primary Antibodies

Antigen	Source	Number	Supplier
α -SMA	mouse	M0581	Dako
β -Actin	goat	sc-1616	Santa Cruz
CD31	mouse	M0823	Dako
Hif1 α	rabbit	EP1215Y	Abcam
KI67	mouse	ab15580	Abcam
p22phox	rabbit	sc-20781	Santa Cruz
p22phox	rabbit	ab75941	Abcam

Secondary Antibodies for Western Blot

The secondary antibodies are selected to target the heritage of the primary antibody. They are connected to a horseradish peroxidase enzyme and are diluted in TBS-T containing 5% skim milk powder.

Target	Dilution	Supplier
rabbit	1:10.000	Calbiochem/ Merck
goat	1:10.000	Calbiochem/ Merck

Secondary Antibodies for Immunostaining

Target	Wavelength	Dilution	Supplier
goat	594 nm (red)	1:250	Invitrogen
mouse	488 nm (green)	1:250	Invitrogen
mouse	594 nm (red)	1:250	Invitrogen
rabbit	488 nm (green)	1:250	Invitrogen

3.1.8. Primers

3.1.8.1. Primers for genotyping

Target gene

Cyba	Cyba F	5'-CAG-ATG-CCC-ACT-GAC-TGC-TA
	Cyba R	5'-CGA-GCC-ACA-GTA-CAG-CTT-CA
NOX1	NOX1 F	5'-GTA-CTA-AAC-AGA-GAA-AGG-CTC-TCC-C
	NOX1 R	5'-TAC-TGG-GAC-AGC-TTC-CTG-CAT-CCC
	NOX1 R2	5'-TGT-GAA-CTG-ATG-GCG-AGC-TCA-GAC
	LAR3	5'-CAA-CGG-GTT-CTT-CTG-TTA-GTC-C

3.1.8.2. Primers for qPCR

Target gene

h β -Actin	fw	5'-CCA-ACC-GCG-AGA-AGA-TGA
	rev	5'-CCA-GAG-GCG-TAC-AGG-GAT-AG
h Hif1 α	fw	5'-GAA-GAC-ATC-GCG-GGG-AC
	rev	5'-TGG-CTG-CAT-CTC-GAG-ACT-TT
h p22phox	fw	5'-GCG-TCT-GGC-CTG-ATT-CTC
	rev	5'-CAC-ACC-TGC-AGC-GAT-AGA
h PGK 1	fw	5'-CTG-TGG-CTT-CTG-GCA-TAC-CT
	rev	5'-CGA-GTG-ACA-GCC-TCA-GCA-TA
h VEGF	fw	5'-AGG-AGG-AGG-GCA-GAA-TCA-TCA
	rev	5'-CTC-GAT-TGG-ATG-GCA-GTA-GCT
m β -Actin	fw	5'-CTA-AGG-CCA-ACC-GTG-AAA-AG
	rev	5'-ACA-GCC-TGG-ATG-GCT-ACG
m β -MHC	fw	5'-CTA-CAG-GCC-TGG-GCT-TAC-CT
	rev	5'-CTC-CTT-CTA-GAC-TTC-CGC
m Hif1 α	fw	5'-GCA-CTA-GAC-AAA-GTT-CAC-CCT-GAG-A
	rev	5'-CGC-TAT-CCA-CAT-CAA-AGC-AA

m NOX1	fw	5'-TGT-GTC-GAA-ATC-TGC-TGT-CC
	rev	5'-CCA-GCT-TAT-GGA-AGG-TGA-GG
m NOX2	fw	5'-GGG-CTA-TTC-AAT-GCT-TGT-GG
	rev	5'-CTT-GAG-AAT-GGA-GGC-AAA-GG
m NOX4	fw	5'-GAA-GAT-TTG-CCT-GGA-AGA-ACC
	rev	5'-AGG-TTT-GTT-GCT-CCT-GAT-GC
m p22phox	fw	5'-TGG-CCT-GAT-TCT-CAT-CAC-TG
	rev	5'-TCC-AGC-AGA-CAG-ATG-AGC-AC

3.1.9. Buffers and solutions

Krebs-Hepes Buffer

NaCl	99 mM
KCl	4.69 mM
NaHCO ₃	25 mM
KH ₂ PO ₄	1.03 mM
D-glucose	5.6 mM
Na-HEPES	20 mM
CaCl ₂	2.5 mM
MgSO ₄	1.2 mM

Lysis Buffer for animal tissue:

1M TRIS-HCl pH 8.0	5% (v/v)
EDTA 0.5M	20% (v/v)
5M NaCl	2% (v/v)
20% SDS	5% (w/v)
H ₂ O	68% (v/v)

10x Orange G Loading Dye:

Glycerol	30% (v/v)
Orange G	0.2%(w/v)

dissolve in distilled water

Phosphate Buffer 0.1M

NaH ₂ PO ₄	25 mM
Na ₂ HPO ₄	75 mM

dissolved in distilled water [pH 7.3]

10x TAE-Buffer:

TRIS	0.5 M
Sodium acetate	0.2 M
EDTA	0.02 M

adjust pH to 7.4 – store at RT

TBS-T

NaCl	8% (w/v)
KCl	0.2% (w/v)
TRIS 1M, pH 7.5	25% (v/v)
Tween 20	11% (v/v)

store at RT

TE-Buffer:

TRIS	10 mM
EDTA	1 mM

adjust pH to 7.5; store at RT

Tris-EDTA buffer:

Tris	10 mM
EDTA	1 mM
Tween 20	0.05% (v/v)

adjust pH to 9.0

1x Tissue Lysis buffer for protein extraction:

TRIS-HCl (pH 7.5)	20 mM
NaCl	150 mM
Na ₂ EDTA	1 mM
EGTA	1 mM
Sodium pyrophosphate	2.5 mM
β-Glycerophosphate	1 mM
Na ₃ VO ₄	1 mM
Triton X	1% (v/v)

store at -20°C, add freshly prepared PMSF in ethanol of 1mM concentration prior to usage

3.1.9.1. Western blot solutions

Amido Black staining solution:

Naphthol blue black	0.1%
Methanol	50%
Acetic acid	10%

ECL 1:

TRIS	100 mM
Luminol	2.5 mM
Cumaric Acid	0.4 mM

adjust pH to 8.8 – store at 4°C in the dark

ECL 2:

TRIS	100 mM
H ₂ O ₂	0.15% (v/v)

adjust pH to 8.8 – store at 4°C in the dark

3x Laemmli buffer:

TRIS	190 mM
SDS	6% (w/v)
Glycerol	30% (v/v)
Bromophenol blue	0.06% (w/v)
DTT	15 mM
EDTA	60 mM

adjust pH to 6.8; store at -2°C

10x Running buffer:

TRIS	25 mM
Glycine	200 mM
SDS	0.5% (w/v)

adjust pH to 6.8; store at -2°C

10x Transfer buffer:

TRIS	25 mM
Glycine	200 mM
Methanol	20% (v/v)

store at RT

1x Transfer buffer:

Transfer Buffer 10X	250 ml
Methanol	500 ml
H ₂ O	1750 ml

store at RT

3.1.9.2. Solutions for histology

Blocking buffer:

BSA	1% (w/v)
Triton-X-100	0.05% (v/v)

dissolved in PBS

PBS-Triton washing buffer:

Triton-X-100	0.05% (v/v)
--------------	-------------

dissolved in PBS

Permeabilization buffer:

Triton-X-100	0.2% (v/v)
--------------	------------

dissolved in PBS

Scott's Tap Water:

Sodium bicarbonate	2 g/l
Magnesium sulphate	20 g/l

WGA-working solution:

WGA-stock (5 mg/ml)	10 µg/ml
---------------------	----------

dissolved in PBS

3.1.10. Software

Software	Supplier
Adobe Photoshop CS5	Adobe Systems
Adobe InDesign CS5	Adobe Systems
Aida	Elysia Raytest
AxioVision	Carl Zeiss
CellSens	Olympus
EBS9M Schreiber	GHM Messtechnik GmbH
Excel	Microsoft
GraphPad PRISM	GraphPad Software
HAEMODYN Software	Harvard Apparatus
Quantity One	Bio-Rad
REST-MCS Version 2	Gene Quantification
Word	Microsoft

3.2. Methods

3.2.1. Molecular biological methods

3.2.1.1. DNA analysis and genotyping

3.2.1.1.1. DNA extraction from animal tissue

Mouse tissue samples from ear or tail were dissolved in 500 µl of lysis buffer including 15 µl of proteinase K (20 g/ml) and incubated in a Thermomixer at 56°C, shaking overnight. 250 µl of 5 M NaCl was added to each lysate and mixed by vortexing. The mixtures were spun down at 13.000 rpm for 15 min at RT. About 600 µl of the supernatants were immediately transferred into a new tube, immersed with 400 µl isopropanol and mixed by inversion. Precipitating DNA can be observed at this stage. Again, the samples were spun down at 13.000 rpm for 15 min at RT. Then the supernatants were carefully removed by decantation. The remaining DNA pellets were washed with 1 ml of 70% ethanol stored at RT, mixed by inversion and spun down again at 13.000 rpm for 10 min. Supernatants were removed as described above. The DNA pellets were air dried for at least one hour at RT and then dissolved in 50 µl of 0.1x TE buffer and incubated for 10 min at 37°C while gently mixing. The DNA samples were stored at -20°C.

3.2.1.1.2. PCR

To make a DNA sequence of interest accessible to further analysis and visualization, a polymerase chain reaction (PCR) needs to be performed. This method, first developed by Kary Banks Mullis and Michael Smith, has been the foundation for the genomic research of our days [61].

Hereby a thermo-stable polymerase enzyme is used. A thermal cycler applies the necessary temperatures for reaction to the mixtures. At around 60°C the primers are connecting to the single DNA strand. The optimum temperatures are depending upon the individual primer sequences and amounts of C-G regions. 72°C provides the optimal working temperature for the polymerase enzyme. At 94°C the newly created double strand DNA is separated into single strands. Hereby the DNA sequence is rapidly amplified exponentially.

A standard PCR was performed with the Thermocycler GenAmp PCR system 9700 as follows (reaction volume 25 µl):

	[μ l]
H ₂ O	18.5
10x buffer with MgCl ₂	2.5
dNTPs (10mM)	0.25
primer FW (10mM)	0.25
primer RV (10mM)	0.25
DMSO	1
Tag (5U/ μ l)	0.25
DNA	2

Reactions:

Denaturation	94°C	05:00 min
--------------	------	-----------

40 cycles:

Denaturation	94°C	00:30 min
Annealing	59°C	01:00 min
Extension	72°C	01:00 min

Finalization:

Extension	72°C	07:00 min
Incubation	4°C	till end

The obtained DNA was stored at 4°C.

Digestion of PCR product for detection of the Y121H mutation:

To further analyse the presence of the Y121H mutation in the Cyba gene, characterizing the NMF333 mouse strain, a digestion of the PCR product with a restriction enzyme, BslI, was required [144]. The digestion mixture with a total volume of 20 μ l per sample was prepared as follows:

	[μ l]
H ₂ O	2.5
NEB buffer 3	2
Bsl I	0.5
PCR product	15

The mixture was then incubated overnight at 55°C.

3.2.1.1.3. Electrophoresis

To visualize the amplification product the PCR products were separated by agarose gel electrophoresis. Ethidium bromide was used as dye. While intercalating with double-strand DNA a fluorescence signal is emitted when observed under ultraviolet light. The gel concentrations were selected upon the expected DNA product size and varied between 15-3%.

100 ml of 1x TAE buffer was mixed with agarose standard and heated in a microwave until no agarose particles were visible anymore. Water was added in the end to compensate evaporation during the cooking process. 5 µl of ethidium bromide was added and the fluid agarose was poured into the plastic form containing and a comb to form the loading wells. Bubbles needed to be removed to guarantee a proper run of the DNA. The agarose was left for 30 min for polymerization at RT. The solid gel was transferred into the electrophoresis chamber and immersed with 1x TAE buffer, covering the wells and gel completely. The PCR mixtures were blended with 2 µl of 10x orange loading dye. 12 µl up to 20 µl of sample were loaded depending on the well size. 5 µl of Quick-Load DNA Ladder were used as marker. The electrodes were connected, placing cathode at loading side and the anode at the opposite. 90 V were applied for about one hour, the individual running time was determined by observing the progress of the dye in the gel.

For visualization of the DNA bands, the gel was placed in the UV camera Gel doc 2000 operated by the Quantity One software. The band bearing parts of the gel appeared bright under ultraviolet light.

3.2.1.2. Tissue and cell lysis

Tissue lysis is a crucial step for further analysis of protein and gene expression. Several methods to disrupt cellular boundaries and transfer the cellular components into a buffer solution were described. For protein extraction, 1x tissue lysis buffer was used, immersed with 25x proteinase K inhibitor mix. For RNA extraction the lysis buffer of the RNA extraction kit was used as described in the manual. Different lysis methods have been assessed:

3.2.1.2.1. Sand grinding

For protein extraction a frozen tissue piece was transferred in a glass tube containing 500 μ l of protein lysis buffer. A tip of autoclaved sand was added. While constantly cooled with ice, the tissue was grinded and solubilized using a fitting glass pestle. The lysate was transferred into a new tube and spun down at 13.000 rpm for 5 min at 4°C. The supernatant was carefully transferred into a new tube.

3.2.1.2.2. Automatic homogenizer

The Precellys 24 system is an automatic homogenizer, performing tissue lysis by strong shaking. Special ceramic beads were used to break up the tissue integrity during the shaking process. Additionally, the temperature was regulated using the cryolysis unit. The cooling unit, containing liquid nitrogen, regulates the homogenizer's temperature to a constant working temperature of 4°C to prevent protein degradation during the lysis process.

For protein extraction the frozen tissue samples were transferred into the bead containing tubes filled with protein lysis buffer. The amount of lysis buffer was adapted to the tissue mass. 30 mg of tissue required about 600 μ l of lysis buffer. The working parameters including rotation speed, number of cycles, cycle duration and resting time between the cycles were set as follows:

6000 rpm – 2 cycles of 20 sec – resting time 30 sec

The program was repeated two to three times.

Temperatures below 4°C would result in buffer freezing, impairing the free movement of the beads and hereby the lysing process. After successful tissue lysis the tubes were centrifuged at 10.000 rpm for 10 min at 4°C and the supernatant was carefully transferred into a new tube.

3.2.1.2.3. Tip sonicator

For ultrasonic tissue lysis the "Sonopuls ultrasonic homogenizer" from Bandelin was used. Via a tip, ultrasonic pulses are transferred into mixtures to break up tissue boundaries and homogenise mixtures. Continuous or pulsed energy application is possible. In the latter mode, cycles of one second were divided into a working and resting phase.

For RNA extraction, approximately 10 mg of tissue were transferred into 500 µl lysis buffer blended with 5 µl Bond Breaker. The tissue was solubilized in the pulsed mode for three seconds with a working phase of 0.8 and a power of 50% and constantly cooled on ice. The cycle was repeated twice.

For protein extraction a larger amount of tissue was required. About 30-40 mg of tissue were transferred into 600 µl of protein lysis buffer. A milder program was used to prevent protein degradation. Three runs of three seconds with a working phase of 0.6 and 35% of power were performed.

The obtained lysate was spun down at 13.000 rpm for 5 min at 4°C. The supernatant was transferred into a new tube.

3.2.1.2.4. Cell lysis

To obtain RNA from cells, about 400 µl of RNA lysis buffer was directly applied to the cell culture dishes, that had been frozen in liquid nitrogen before. For protein extraction about 300 µl of protein lysis buffer were used. Placed on ice, the inside of the dishes was scratched with a cell lifter to bring the cells in solution and disrupt their boundaries. The lysis buffer containing the cell components was recollected and transferred into a new tube. Cell pellets were easily dissolved in the appropriate lysis buffer.

3.2.1.3. RNA-related methods

3.2.1.3.1. RNA isolation and quantification

To extract RNA from animal tissues and cells, column-based RNA extraction kits were used as follows:

Loading of RNA columns

The lysed specimens were blended with an equal amount of ethanol 70 % and mixed by vortexing. 700 µl of the mixture were applied on the RNA columns and spun down at 13.000 rpm for one minute at 4°C. The RNA is caught in the membrane of the column and further purified by two additional washing steps with 500 µl washing buffer.

On column DNase digestion:

The PeqLab kit allows further on column DNase digestion to remove remaining DNA to prevent falsification of later RNA analysis by qPCR. Hereby 1.5 µl of DNaseI dissolved in 73.5 µl DNase buffer was directly applied on the RNA columns after the first washing step and left for incubation at RT for 15 min. To remove the DNase mixture, 400 µl of washing buffer was applied on the column and, after 5 min of incubation time, spun down at 13.000 rpm for 15 sec at RT.

Elution:

Two more washing steps with 600 µl of a second washing buffer, filled up with 100% ethanol, were required. Finally, the columns were spun down at 13.000 rpm for 2 min without solution to remove remaining traces of ethanol and dry the membranes. At last the RNA was eluted with 40 µl of RNase-free water. After 2 min of incubation the columns were centrifuged at 10.000 rpm for 2 min. The elution step was repeated when greater amounts of RNA had been expected. The RNA lysate was stored at -20° C for short time and at -80°C for long time storage.

Quantification:

The quantity and quality of RNA were determined by "NanoDrop". Hereby the RNA concentration and quality (as a ratio of two absorption peaks at A260 and A280) were measured photometrically in 1 µl of the mixtures.

3.2.1.3.2. RT-PCR

To further analyse the extracted RNA by quantitative real-time PCR (qPCR), a transcription of the obtained mRNA into more stable complementary DNA (cDNA) is required. Therefore, the "High-Capacity cDNA Reverse Transcription Kit" from Applied Bioscience was used. The reaction mixtures were prepared with 1 µg or 0.5 µg of RNA dissolved in 10 µl of RNase free water as follows:

	[μ l]
RT-Buffer 10X	1
25X dNTP Mix	0.8
10X Primer Mix	2
MultiScribe Reverse Transcriptase	1
H ₂ O	5.2
RNA	10

For each sample a negative control was included, replacing the MultiScribe RT enzyme with water. It was treated like normal samples in the following steps. The provided random primer mix was used to transcribe the whole RNA material into cDNA. The PCR was performed using the thermal cycler "GeneAmp PCR System 9700" as follows:

Incubation for primer hybridization	25°C	10:00 min
Incubation for transcription	37°C	120:00 min
Incubation for enzyme deactivation	85°C	05:00 min
Incubation for storage	04°C	till end

The obtained cDNA was stored at -20°C and, depending on the RNA concentration, diluted from 1:10 up to 1:40 with water for the final quantitative PCR analysis.

3.2.1.3.3. qPCR

Quantitative PCR (qPCR) is a method to determine the mRNA levels of cells and tissue at the time point of the sample collection. Therefore, the mRNA was transcribed into the stable complementary DNA as described above, that is, compared to genomic DNA, free of introns and non-coding regions. Quantitative PCR was performed as SYBR Green method using the PerfeCTa SYBR Green mix and a Rotor Gene 6000 system. The dye SYBR Green is emitting a fluorescence signal while binding to double-strand DNA which increases proportionally to the amount of double-stranded DNA, replicated from the sequence of interest during the PCR. The intensity of the signal, measured after every amplification step, describes a characteristic curve of exponential growth. The relative cDNA (and mRNA) expression can be calculated from the curve in comparison to a reference gene and a

reference condition based upon the threshold cycle (Ct), representing the beginning of exponential growth of each curve [202]. For each reaction the following mixture was used:

	[μ l]
cDNA (diluted)	2
PerfeCTa	5
primer FW	0.1
primer RV	0.1
H ₂ O	2.8

Each cDNA sample was run three times to obtain technical triplicates of the target gene expression. Furthermore, the negative control from the RT-PCR and blank water were included. The reaction contained the following steps:

Denaturation	95°C	00:30 sec
--------------	------	-----------

40-50 cycles:

Denaturation	95°C	00:02 sec
Extension	60°C	00:20 sec

Finalization:

Holding	55°C	00:30 sec
Melting	55°C – 95°C	

During the melting process, the temperature was raised in 1°C steps every 5 sec. Melting curve analysis confirmed the amplification of a single DNA sequence during the PCR to rule out contamination with genomic DNA and falsification of the experiment.

Evaluation

For the evaluation of the qPCR results, the REST-MCS – relative expression software tool-multiple condition solver – was used. The software compares the selected genes of interest und specific experimental conditions with a reference gene at a reference condition, using pair wise fixed reallocation randomisation test, based upon the Ct values of the PCR curves. For each gene and each condition up to nine values were analysed, consisting of three technical replicates, obtained from two to three biological specimens. The software

calculated the absolute target gene regulation, expressed as fold time expression compared to the reference condition, as well as a mean standard error and a p-value.

3.2.1.4. Protein-related methods

3.2.1.4.1. Protein quantification

The quantification of the obtained protein yield is a crucial step to further analyse the extracted protein samples and provide comparability. Two different methods were used. While the protein quantification after Bradford is more accurate, the dot blot quantification method is faster and requires a smaller amount of the protein sample. Nevertheless, it usually provided to be a good and sufficient determination of protein concentration.

3.2.1.4.1.1. *Dot blot*

For dot blot protein quantification, a protein standard row was required, prepared from BSA in 0.5 mg/ml, 1 mg/ml, 1.5 mg/ml, 2 mg/ml, 2.5 mg/ml, 3 mg/ml, 4 mg/ml and 5 mg/ml concentration steps.

1 µl of each protein standard and 1 µl of the protein sample of interest were applied on a nitrocellulose membrane. Next the membrane was immersed with Amido-black solution for several minutes until the dye had stained the membrane completely. The membrane was washed for several times with 50% methanol to destain the membrane and to reduce the black background. The protein containing dots remained stained, with the colour intensity depending upon the protein concentration. The absolute protein concentration of the sample was estimated in comparison to the protein standard row.

3.2.1.4.1.2. *Bradford assay*

The Bradford assay for protein quantification was first described by M.M. Bradford in 1976 and has become one of the standard procedures to determine protein concentrations [114]. Hereby the dye Coomassie Brilliant Blue G-250 (Roti-Quant) interacts with proteins, changing its charge from cationic to anionic. The change in charge leads to a shift in colour and absorption maximum from 470 nm to 595 nm proportionally to the protein concentration.

To perform the Bradford assay, the protein samples were diluted from 1:300 up to 1:600. Furthermore, a protein standard row prepared from BSA at concentrations ranging from 10

$\mu\text{g/ml}$ to $80 \mu\text{g/ml}$ was required. For analysis $200 \mu\text{l}$ of Bradford reagent were mixed with $80 \mu\text{l}$ of protein sample in a 96 well plate. The absorption was assessed using a plate reader. The absolute protein concentration of the samples was calculated from the standard curve using linear regression analysis.

3.2.1.4.2. Western blot analysis

Western blot analysis is one key method to determine levels of specific proteins. Total protein extracts are separated by gel electrophoresis and blotted on a nitrocellulose membrane. Via a two-step antibody detection, protein bands of interest can be visualized and compared according to their intensity.

Gel preparation

The running and stacking gels were prepared as described below. The gel concentration was selected upon the molecular size of the protein of interest. The glass gel chambers were filled with liquid running gel and covered with isopropanol, creating an even and clean edge. The gels were left for polymerization for 20 min at RT. The isopropanol was removed and the stacking gel applied, inserting combs to form the loading wells. The gels were left another 30 min to solidify.

Running gel

	8%	10%	12%	Volume
Water	3.4	2.8	2.1	ml
Acrylamide 30%	2.7	3.3	4	ml
1M Tris HCL pH 8.8	3.7	3.7	3.7	ml
SDS 10%	100	100	100	μl

To initiate the polymerization process $80 \mu\text{l}$ of ammonium persulfate and $10 \mu\text{l}$ of TEMED were added.

Stacking gel

	5%	6%	Volume
Water	2.14	2.04	ml
Acrylamide 30%	0.488	0.584	ml
1M Tris HCL pH 6.8	0.375	0.375	ml
SDS 10%	30	30	μl
Bromphenol blue	30	30	μl

To initiate the polymerization process 15 μl of ammonium persulfate and 3 μl of TEMED were added.

Sample preparation

The protein samples were blended with 3x Laemmli buffer in 3:1 relation and heated up to 95°C, shaking, for 5 min to denature the protein structure.

Electrophoresis

SDS electrophoresis separates the proteins according to their molecular size. The individual electric charge of the proteins is annihilated through the degeneration process. SDS, covering the proteins, provides and equals electrical charge.

The gels were placed in the electrophoresis chamber and covered with 1x running buffer. 50 μg of protein sample and a protein marker were loaded. The electrophoresis chamber was connected to a power supply. Voltage was set to 100 V maximum for the passage of the stacking gel and was increased up to 200 V when the samples had reached the running gel. The electrophoresis was run until the bromophenol blue dye reached the bottom of the gel.

Transfer

The transfer process transports the separated protein lanes from the gel onto a nitrocellulose membrane to fix them and to make them accessible to further analyzation.

The stacking gel was carefully removed from the running gel and the following steps were performed in cold 1x running buffer. Within the transfer cassette a package was made up of: porous pad – Whatman cellulose filter paper 3 mm – gel – nitrocellulose membrane – filter paper – porous pad. Bubbles between the layers had to be carefully avoided to ensure direct contact of gel and membrane for complete protein transfer. The transfer cassettes and a

cooling unit of frozen transfer buffer were placed into the transfer chambers and filled up with transfer buffer. The transfer was performed at a constant voltage of 100 V for one hour. After successful transfer, the membranes were stained with diluted Ponceau S dye for about 5 min, washed subsequently with water to remove surplus dye from the empty membrane parts, to finally visualize the protein bands.

Hybridization

In the next step the primary antibody was applied to bind its target protein, being a crucial step in the detection process. In advance, blocking of the membranes was performed for two hours at RT with 5% skim milk dissolved in TBS-T, to reduce unspecific binding of the primary antibody to the membranes empty surface. For hybridization the membranes were incubated with the primary antibody diluted in 5% skim milk TBS-T overnight, shaking at 4°C. The first hybridization was finalized for 1 hour at RT.

The membranes were washed three times for 5 to 10 min with TBS-T to remove surplus antibody. The incubation with the secondary antibody, diluted in 5% skim milk TBS-T, was performed at RT for one to two hours. The washing process of surplus antibody was repeated as described above with TBS-T.

ECL detection:

To visualize the antibody marked protein bands, the horseradish peroxidase linked to the secondary antibody catalyses a luminescence reaction. Therefore, ECL solution one and two were combined in relation 1:1, applied on the membranes and left for incubation for one minute [142]. The blots, placed between two transparency papers, were exposed to light sensitive x-ray films for short-time (one minute) and long-time exposure overnight. For development, the films were immersed in rapid developer solution until the bands became visible, rinsed with water and transferred into the fixing solution. It is crucial to avoid light exposure of the films until they are finally transferred into the fixing solution. Multiple films were used to create different levels of exposure.

Quantification

The detected protein bands were quantified according to their intensity. The loading control PonceauS or β -Actin served as reference for normalisation. The films were digitalized with a flatbed scanner. Using the software ImageJ, the intensity of the protein bands and their corresponding loading controls were acquired. To calculate the relative protein expression

factor, the normalized intensity of the protein bands was compared to a reference condition. At least three replicates per condition were used for calculation.

3.2.1.5. Measurement of reactive oxygen species

For direct assessment of superoxide production, the electron paramagnetic resonance (EPR) measurement system E-scan by Bruker was used. EPR is a technique that allows the detection of species harbouring unpaired electrons by spectroscopy. Similar to nuclear magnetic resonance (NMR) – better known as magnetic resonance imaging (MRI), used in daily radiology routine – which detects the spin of protons, EPR detects the spinning of single electrons. For the detections of short living radicals a spin trap like CMH is necessary. CHM is oxidised by the radical, forming a new radical itself, that can be measured due its long half-life time. Thereby the accumulation of the oxidized spin trap correlates with the production rate of free radicals [72].

PBMCs (s. 3.2.2.8.2.) obtained from WT and NMF333 mice were washed with PBS, adjusted to a total number of $1 \cdot 10^6$ cells/ml and transferred in Krebs-Hepes buffer. 5 μ M diethyldithiocarbamate (DETC) and 25 μ M desferroxamine were added to the samples. Finally, 100 μ m of the spin trap CMH, which is necessary for capturing the short-living free radicals was added. The whole procedure was performed on ice to prevent an early activation of reaction. For measurement, the samples were transferred to special, gas permeable, glass capillaries, which were sealed one side. The cell suspension carrying capillaries were placed in the resonator, which is filled with a definite gas mixture containing 1% O₂, 5% CO₂ and 94% N₂ at a pressure of 22 mmHg. The special EPR settings for CMH contained: centre field at 3455 G, sweep width of 10 G, a frequency of 9.7690 GHz. Further settings including microwave power and modulation amplitude were set on auto-tune. The measurement spectra were recorded over a period of 10 min, with a frequency of 1/60 Hz. The superoxide production rate was calculated by linear regression of the measurement points.

3.2.2. Animal experiments

All animal experiments were approved by the responsible legislation at the “Regierung von Oberbayern”.

3.2.2.1. Mouse lines

3.2.2.1.1. NMF333 mice

The A.B6 Tyr⁺-Cyba^{nmf333}/J mouse strain, also referred to as NMF333, which has been described to harbour a point mutation in the Cyba gene with a consecutive loss of p22phox protein, was obtained from Jackson Laboratories, Bar Harbour, MN (JAX stock #005445) [95, 144]. The Y121H mutation was chemically induced by ethylnitrosourea (ENU) mutagenesis and is located in exon 5 of the Cyba gene on chromosome 8, coding for a transmembrane domain of the p22phox protein [95]. The T to C point mutation leads to a substitution of the amino acid tyrosine (Y) with histidine (H) at position 121 (Fig. 5). All mice were of C57BL/6J background, which was used as wildtype control mouse strain. As described by Nakano et al., the Y121H mutation introduced a new cutting side in the gene sequence, which proved to be relevant for genotyping when the PCR product of NMF333 mice is digested with the Bsl1 restriction enzyme [144]. For genotyping, a DNA PCR with consecutive Bsl1 digestion was performed as described above (3.2.1.1.2). As a result, wildtype mice are characterized by two bands of 89 bp and 202 bp size, since the restriction enzyme only cuts once. Homozygote NMF333 mice, on the other hand, presented with two bands of 89 bp and 162 bp size. The restriction enzyme cuts a second time in the long strand, the small fragment of 40 bp is usually not visual anymore. Heterozygote mice finally show all three bands of 202 bp, 162 bp and 89 bp size [144] (Fig. 6).

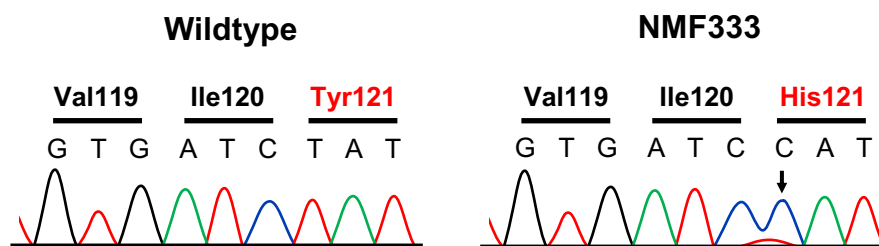


Figure 5 Y121H point mutation in NMF333 mice

The T to C point mutation led to a substitution of the amino acid Tyrosine (Tyr/Y) with Histidine (His/H) at position 121 of the Cyba gene, a transmembrane domain of the p22phox protein. Adapted after [144].

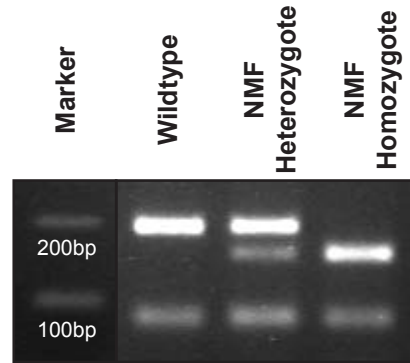


Figure 6 Genotyping results of NMF33

Electrophoresis shows DNA bands characteristic for WT mice, heterozygote and homozygote NMF333 mice, after digestion of the PCR product with BslI restriction enzyme.

3.2.2.1.2. NOX1-K.O. mice

NOX1-K.O. mice were generated using the “knockout-first” allele method (Fig. 7). Thereby, the gene of interest is flanked upstream with a LacZ/ Neomycin cassette including FRT cutting sites. Furthermore, the target gene is enclosed with loxP cutting sites (Tm1a). The further knock out process is dependent on recombinase enzymes, recognizing the different cutting sites and deleting the enclosing DNA sequence. In this case the “Cre recombinase” (Cre) recognizes the loxP sites and the “Saccharomyces Cerevisiae FLP1 recombinase“ (Flp) recognizes the FRT cutting sites. We used mice, expressing Cre recombinase (Cre⁺ deleter mice) and “Saccharomyces Cerevisiae FLP1 recombinase“ (Flp⁺ mice) globally only.

When heterozygote Tm1a mice were bred with Cre⁺ deleter mice, the knockout-first allele structure leads to deletion of the target gene, as well as of the Neomycin cassette, and replacement with the LacZ reporter gene (Tm1b). The transcription of the LacZ cassette leads to beta-galactosidase expression, that catalyses the conversion of the X-gal staining dye. In this state, the X-gal staining allows the detection of the normal expression site of the gene of interest.

For generation of the real knock out line, Tm1a mice are crossed with Flp⁺ mice, recognising the FRT sites and thus deleting the LacZ/Neomycin cassette. In this state, the newly created Tm1c mice, also referred to as floxed line (from “flanked by loxP”), differ from WT mice only by the presence of the loxP sites, flanking the gene of interest. These pseudo wildtype mice served as WT control in the experiments. Finally, the Tm1c mice were crossed with Cre recombinase expressing mice, recognizing the remaining loxP sites and thus deleting the gene of interest (Tm1d) [34].

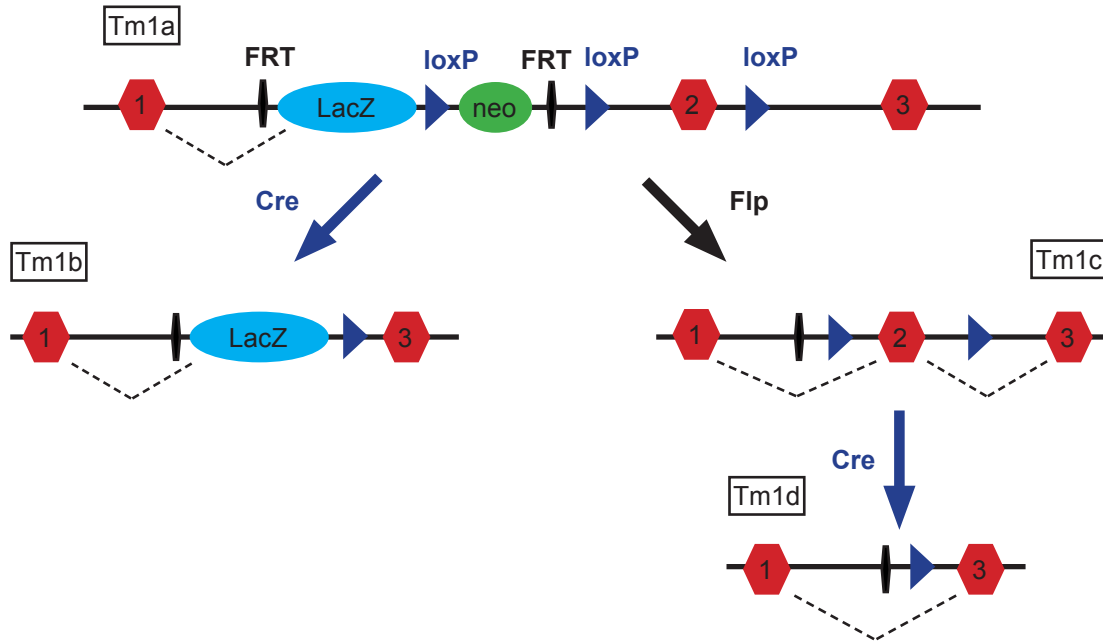


Figure 7 Schematic illustration of the "knockout-first" allele

In Tm1a mice, the gene of interest (GOI), here exon 2, is flanked by loxP cutting sites, whereas the LacZ/neomycin cassette is enclosed by FRT cutting sites. When crossed with Cre⁺ mice, the GOI is replaced by the LacZ cassette, creating Tm1b reporter mice. When crossed with Flp expressing mice, a pseudo WT state, also referred to as floxed line, is established (Tm1c). To create the real knockout (Tm1d), Tm1c mice were crossed with Cre⁺ mice, finally deleting the GOI. Adapted after [34].

For creation of the NOX1-K.O. line, mice of C57BL/6N background were used. The loxP sites enclose the exons four to nine of the NOX1 gene, that is located on the long arm of the X-chromosome [55]. To identify the different stages in the breeding process, multiple PCR reactions and primers were necessary. In WT mice, PCR with the NOX1 forward primer (NOX1 F), binding upstream of the FRT site, and reverse primer (NOX1 R), binding downstream of the LacZ/ neomycin cassette in the target gene region, resulted in a WT DNA band of 530 bp size.

In Tm1a mice, the additional LAR3 primer was required, binding a region in the LacZ cassette and resulting in a DNA band of 410 bp size (Fig. 8a). In the floxed line (Tm1c) the NOX1 forward and reverse primers produced a DNA band of 690 bp, since the additional loxP site is included (Fig. 8b). In the final knockout mice, an additional second NOX1 reverse primer (NOX1 R2) was required, binding to a region downstream of the Cre-deletion knockout allele and resulting in a NOX1-K.O. DNA band of 430 bp (Fig. 8c).

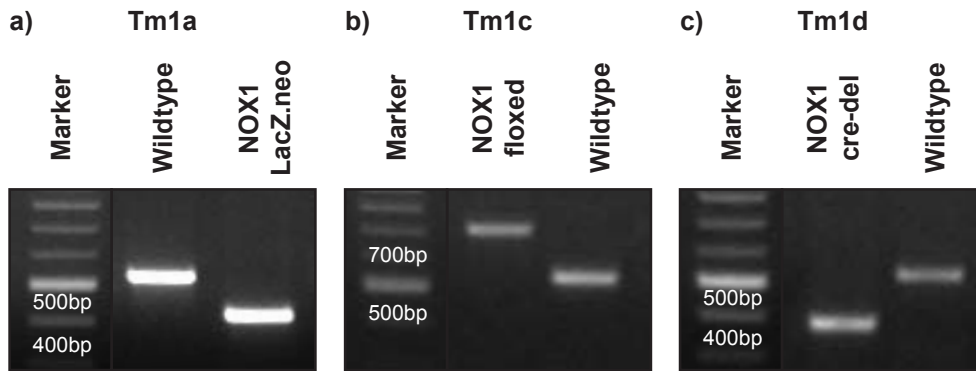


Figure 8 Genotyping results of NOX1-K.O. mice

The WT allele is characterised by a DNA band of 530 bp size, produced by NOX1 F and R primers. a) In Tm1a mice, the NOX1 F and LAR3 primers produce a characteristic DNA band of 410 bp size. b) In Tm1C mice, the additional loxP site enclosed by the NOX1 F and R primers resulted in a DNA band of 690 bp. c) NOX1-K.O. mice are characterised by a DNA band of 430 bp size, produced by an additional NOX1 R2 primer, binding in the Cre-deletion allele.

3.2.2.2. Mouse keeping

Mice were held in an animal facility under specific pathogen free conditions under the supervision of a licenced veterinarian for animal experiments. For breeding, a male and a female mouse were placed together in one cage. The female mice were checked regularly for vaginal plugs. This plug is made up from secretion of the male prostate gland and is, though no guarantee for pregnancy, a proof for the sexual activity of the mice. It usually remains for 8 to 24 hours after intercourse. Nevertheless, it is not possible to observe the plug every time [93]. The pregnancy of mice lasts about 21 days. The pups were left for three to four weeks with their mother before separation. Ear marking was performed to individualize the mice and obtain material for genotyping. At the age of eight weeks, hypoxia experiments were started. Both genders were used, since preliminary experiments did not show a difference in response to the experimental conditions between female and male mice.

3.2.2.3. Hypoxia

Mice were exposed to chronic hypoxia in normobaric hypoxia chambers in an atmosphere of 10% oxygen for 21 days. Durations of two and three weeks had been compared initially, but mice exposed for three weeks presented with a stronger reaction to the hypoxic conditions. The chambers were air tight boxes made of acryl glass that provided place for up to two mouse cages. When closed, they were connected to the room air only by a

computer-controlled valve. An oxygen sensor continuously measured the oxygen concentration within the chambers, while a ventilator provided continuous air circulation. Within the closed system, the chamber air circulated through a soda lime cylinder to erase surplus CO₂. A change in colour from white to purple indicated that the CO₂ binding capacity has reached its limits and the soda lime was exchanged. Furthermore, the air flew along a Peltier element, a metal plate that cools down when electricity is applied. The Peltier element cooled down the passing air and led to condensation of air-bound water into a cylinder. Through this process the humidity was held in a constant range between 65-75% without the necessity of opening the chambers.

To initially reduce the oxygen concentration of the chambers to 10%, they were slowly flooded with pure nitrogen until the chamber air reached the required concentration. The oxygen concentration was constantly held in a range between 10.0% and 10.3%. When the oxygen concentration fell below 10%, the valve opened to allow entering of room air until the oxygen concentration reached 10.3%. The valve remained closed until the oxygen was used up by the mice and the lower limit was reached again. A computer continuously recorded the oxygen and humidity levels to guarantee the proper function of all systems.

At least twice a day the hypoxia chambers and the mice were checked. Once a week the mice were taken out of the chambers to change cages and renew food and water. The mice were examined and weighed to check their health status. A strong drop in weight over 10% indicated a health problem and the experiment for the individual mouse was stopped immediately.

3.2.2.4. Haemodynamic measurements

To assess the effect of chronic hypoxia on the vascular system and the heart, direct intracardiac pressure measurements were performed. Therefore, we used a transthoracic approach. First, the left ventricle was punctured from outside. The right ventricle was assessed by carefully pushing the cannula forward through the septum. Haemodynamic measurements were performed as final experiments, as the integrity of the cardiopulmonary system is strongly affected by the measurement process. 10 to 12 mice were measured for each group.

3.2.2.4.1. Pressure transducer system

The measurement system consisted of a tip catheter pressure transducer head (ISOTEC), connected to the Transducer Amplifier Modul-A, that passed the signal to the measurement computer. The experiments were recorded with the HAEMODYN software at a frequency of 1000 Hz.

The transducer head is built up of the pressure dome, that is fitted with two valves. The first one is a three-way valve connected to the flexible hose carrying the disposable 25G cannula and a 20 ml syringe filled with distilled water for flushing. The second valve serves as protecting pressure relief valve during the filling process, remaining closed during the measurement process. The complete system was filled up with distilled water, serving as medium to transfer the pressure from the catheter tip to the pressure transducer element. The transducer head is mounted at the height of the mouse's heart.

3.2.2.4.2. Anaesthesia system

During the measurement, mice were held under isoflurane anaesthesia. A special, semi-closed anaesthesia system for rodents from Harvard Apparatus was used. The isoflurane vaporizer was supplied with oxygen from the centre line. Via a flowmeter the total air flow through the system is regulated, whereas the partial flow through the isoflurane chamber of the vaporizer – and hereby the isoflurane concentration of the air – is regulated directly at the vaporizer and varies between 0.5% and 5%. The output of the vaporizer was connected to a gas flow director, allowing to switch the gas flow between the anaesthetizing chamber for induction and the gas mask for the measurement procedure. Both, the chamber and anaesthetizing mask were connected to the Fluovac evacuation system to absorb anaesthetic vapours from the working area. This unit consists of a disposable absorbance canister and an aspirator. The mask combines gas output and simultaneous erasure of excess narcotic gas through a double hose construction [81]. The mice remained ventilated by the mask throughout the whole experiment. A warming plate was used to preserve the mice's body temperature from cooling during anaesthesia.

3.2.2.4.3. Haemodynamic measurement procedure

For induction of anaesthesia the mice were placed in the anaesthetizing chamber. High air flow (4 l/min) and isoflurane gas concentration (5%) were selected to ensure a quick sedation of the mice. Usually the excitation state could be well observed and is typical for an induction

with inhalation anaesthetics. The bodyweight of the sleeping mice was measured on a fine scale. The mice were now placed on their backside at the working place under the anaesthesia mask. The head was covered by the mask to ensure a continuous aspiration of anaesthetic gas. For maintenance the gas flow and isoflurane concentration were reduced (flow: 2.0-2.5 l/min; concentration 2.0-2.5%).

The mice were carefully fixed at their upper and one lower limb to stabilize the measurement position. One limb remained free for reflex checks to ensure proper depth of anaesthesia. Signs for an adequate anaesthesia narcosis are a lack of reaction on external stimuli, for example a pinch between the toes at normal respiratory effort [160]. Gasp breathing on the other hand is a pathological breathing pattern that requires an immediate intervention and reduction of anaesthetic gas concentration.

The left thorax of the mice was carefully depilated using a depilation cream allowing to keep the beat of the heart tip well visible. Prior to each measurement the tip catheter system was re-flushed to fill the new cannula (Jelco 25G) and to remove blood or potential obstructing material. Furthermore, the system was set to zero at the Transducer Amplifier Module. The optimal position for inserting the cannula had been shown to be located slightly cranial compared to the heart beating tip. The skin was punctured between two ribs in a horizontal line. It was important not to rush in, but to carefully pass the skin and muscle layer. The position of the cannula within the body was identified by characteristic pressure curves. On the way to the left ventricle, the lung was passed first where negative pressure values could be observed. The cannula was slowly and evenly pushed forwards. The abrupt appearance of an oscillating pressure curve indicated the correct position in the left ventricle. The cannula was stabilised in this position until a stabile pressure curve could be recorded for several seconds (Fig. 9a). The cannula was now carefully moved forward to penetrate the septum. A sudden drop of the oscillating curve characterizes the correct position in the right ventricle. The pressure values were again recorded in a stabile position for several seconds (Fig. 9b). An increase in the pressure curve could be observed as the cannula was withdrawn through left ventricle. Obtaining the pressure values with the first attempt was defined as crucial criteria for a successful measurement, since the results could be influenced and falsified by bleeding or pericardial tamponade. Furthermore, it would involve unnecessary suffering of the animals. The mice remained in anaesthesia and were euthanized immediately after the measurement by cervical dislocation.

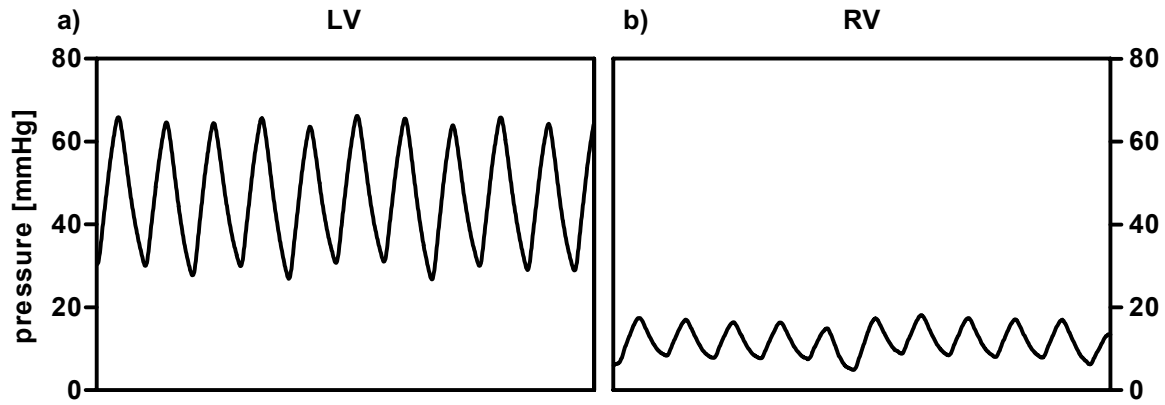


Figure 9 Pressure curves as displayed in Haemodyn Software

Representative pressure curves of a normoxic wildtype mouse showing ten heart actions in a row from a) the left ventricle, oscillating around 50 mmHg and b) the right ventricle, oscillating around 12 mmHg, characterizing the correct position of the tip catheter during the measurements.

3.2.2.5. Euthanasia and organ collection

The mice were euthanized by cervical dislocation according to FELASA rules and the body was opened by median skin cut along thorax and abdomen for collection of the inner organs. The thorax itself was opened by median sternotomy. First, the left and right ventricle were punctured for blood withdrawal. EDTA tubes were used to prime the blood samples for later analysis. The circulation was flushed with PBS to remove the remaining blood from the organs. Prior, one liver lobe was cut to release the PBS from the circulation during the flushing process and to protect the organs from high pressure damage.

Generally, organs determined for histological analyses were washed with PBS, placed in labelled histology cassettes and stored in 4% formalin. Organs determined for molecular analyses were washed with PBS and immediately placed in tubes for shock freezing in liquid nitrogen. They were stored at -80°C .

3.2.2.5.1. Special preparation of the heart

Fine organ preparation was performed using microsurgical instruments. For histological analyses the heart was removed by cutting along the atrioventricular border – the atria remained left in the body. The heart was cut into equal parts along the transversal plane (at 90° towards the heart's axis). Both parts were embedded with the cutting sides facing downwards.

To determine Fulton's index, the right ventricle was separated in situ from the heart. Its mass was acquired using a fine scale. In a second step, left ventricle and septum were isolated together and their mass was acquired. The atria remained inside the body. The isolated ventricles were placed in tubes for shock freezing with liquid nitrogen for further analysis.

3.2.2.5.2. Special preparation of the lung

For histological analyses the lung was flushed and inflated with 4% formalin through the trachea, cut along the main bronchi, washed in PBS and stored in histology cassettes in 4% formalin.

For molecular analyses the lungs were treated as described above without formalin flushing. Formalin led to strong degeneration of RNA, so that they could not be used for further analysis anymore.

Liver, kidney, spleen, pancreas, stomach, skeletal muscle and aorta were isolated for both, histological and molecular analysis as described above without a special treatment.

3.2.2.6. Evaluation of the animal experiments

3.2.2.6.1. Haemodynamic measurements

The haemodynamic pressure measurements were evaluated for each mouse as follows: ten heart actions in a row of a stable recording phase were exported from the HAEMODYN software and imported in Excel.

The following parameters were calculated from the pressure curves for each mouse:

- Mean systolic pressure
- Mean diastolic pressure
- Mean arterial pressure

The ten maxima (= systolic pressure value) and minima (= diastolic pressure value) of each of the ten heart cycles were assessed and used to calculate a mean systolic and diastolic pressure for the individual mouse.

Furthermore, the mean arterial pressure was calculated by the following formula:

$$P_{dias} + \frac{1}{3}(P_{sys} - P_{dias}).$$

The parameters assessed for each mouse were used to calculate mean values with standard deviation for the experimental groups.

3.2.2.6.2. Fulton index

Fulton index is used as parameter characterizing the hypertrophy of the right ventricle in pulmonary hypertension. Hereby, the mass of the isolated right ventricle is normalised to the mass of the remaining heart including left ventricle and interventricular septum. The mass of the atria was not taken into account [205]. The ratios of ten hearts had been assessed for each group.

3.2.2.7. In-vivo Matrigel angiogenesis assay

The in vivo Matrigel sprouting assay was performed to examine the capacity of new vessel formation in mice. The Matrigel matrix is a substance extracted from the Engelbreth-Holm-Swarm mouse sarcoma rich in extracellular proteins like laminin and collagen IV. The Matrigel matrix was found to be an ideal basis for the invasive growth of endothelial cells aiming to form new vessels [126]. Due to its special properties the matrix is soluble around 4°C and changes its state into a solid gel around 22°C to 35°C.

For the in-vivo angiogenesis assay, the Matrigel matrix was enriched with 100 nM of platelet derived growth factor (PDGF), whereas growth factor reduced Matrigel was used as control. The cold and soluble matrix was injected subcutaneously into the lower abdominal sides of eight-week-old WT and NMF333 mice. After two weeks, the Matrigel plugs were excised, formalin-fixed and paraffin embedded for further histological analysis. To trace endothelial cells, an immunofluorescence staining against CD31 was performed.

3.2.2.8. Blood

Blood obtained from the mice was either analysed individually for routine blood work or pooled per experimental group for PBMC isolation.

3.2.2.8.1. Routine blood work

The routine blood work of the individual mice was performed by the laboratory medicine of the German heart centre. A complete blood count was run to assess the mice's adaption to chronic hypoxia.

3.2.2.8.2. Purification of mononuclear cells

Peripheral blood mononuclear cells (PBMCs) were isolated from whole blood for further analyzation, including EPR, protein- and gene expression analysis. The density-based isolation method with Ficoll buffer was used. Ficoll is a polysaccharide developed for mononuclear cell isolation. With its density of 1.077 g/ml, laying above the lymphocyte/monocyte fraction and below the erythrocytes and neutrophils, it physically separates these cells in a suspension [145]. Whole blood from four to six mice of one experimental group was pooled, diluted 1:1 with PBS and transferred into a Falcon tube. The blood was carefully covered with Ficoll buffer in relation 2:1 (4 ml of blood required 2 ml of Ficoll buffer). The mixture was centrifuged at 900 g for 20 min at RT to separate the blood into layers.

The top phase consisted mainly of serum, followed by a thin layer containing the mononuclear cells. Beneath, the Ficoll layer and the erythrocyte pellet were located (Fig. 10). The monocyte layer was carefully extracted with a pipette and transferred into a new tube. The other layers should remain as less affected as possible to preserve the purity of the cellular fraction. In a washing step, the isolated monocyte cellular suspension was diluted with PBS in relation 1:3 and spun down at 500 g for 10 min at RT. The supernatant was discarded, and the cell pellet was frozen and stored at -80°C for further analysis.

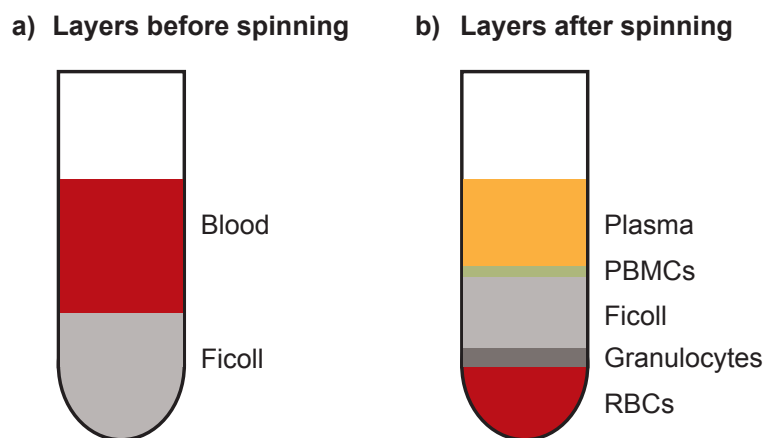


Figure 10 Density based PBMC purification

a) Whole blood was layered on Ficoll buffer in a tube. b) After centrifugation, the blood components were separated due to their density: red blood cells (RBCs), granulocytes, peripheral blood mononuclear cells (PBMCs) and plasma. The PBMCs were carefully extracted with a pipette.

3.2.2.9. Measurement of metabolic activity

In cooperation with the Department of Nuclear Medicine at the University Hospital Rechts der Isar of the Technical University of Munich, positron emission tomography (PET) with the glucose analogue tracer 2-deoxy-2-(^{18}F)fluoro-D-glucose (^{18}F -FDG), was performed according to the protocol provided by the department.

The tracer molecule ^{18}F -FDG is a derivate of glucose, where the hydroxyl group at position C2 is replaced by the radionuclide fluorine-18, which is important for two reasons. Like normal glucose, the tracer is taken up by cells. However, since the replaced hydroxyl group at position C2 is crucial for further glycolysis, ^{18}F -FDG cannot be metabolized and accumulates in cells. The positrons emitted by the radionuclide fluorine-18 can be detected by positron emission tomography (PET) or autoradiography. The distribution and intensity of tracer accumulation correlates with the glucose uptake and metabolic activity within the body, making PET-scans an important tool in daily radiology routine, for example in the cancer diagnosis.

Mice were injected with ^{18}F -FDG at a dose adapted to the mice's bodyweight, ranging between 15.5 and 17.5 MBq. After 45 min time for metabolism of the tracer, a PET-scan was performed, followed by euthanasia and organ collection of heart, lung and liver for autoradiography. The organs were cryo-fixed and cut in sections of 10-20 μm thickness as described below. At least six to nine sections per organ were cut and analysed. In the next step, the sections were exposed to x-ray films for 4-8 h and scanned for evaluation with the AIDA software. The radiation was measured as intensity per area in the right ventricle and the left ventricle, as well as in lung and liver (Fig. 11). For evaluation, the relative intensity was expressed as intensity/area of the RV normalized to the intensity/area of the LV, whereas lung was normalized to liver in the same way. The relative radiation intensity served as surrogate parameter for the metabolic activity.

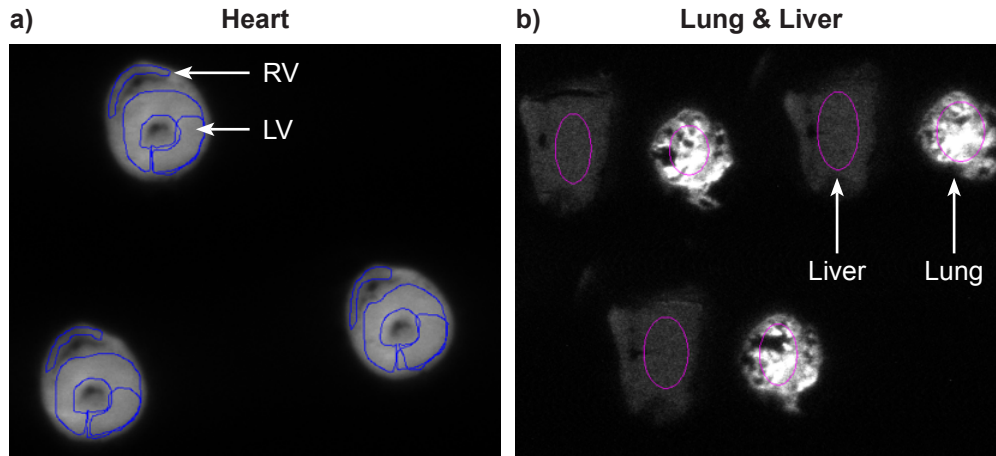


Figure 11 *Autoradiography of mouse organs*

Mice were injected with FDG-18 and autoradiography was used to assess the radiation intensity in a) right and left ventricles and b) lung and liver of WT and NMF333 mice, held under normoxic or chronic hypoxic conditions.

3.2.3. Cell culture

3.2.3.1. Cell lines

In this study, human microvascular endothelial cells (HMEC-1) were used as example for a human derived cell line, which has been well characterized in the context of HIF-expression and hypoxia [79]. Furthermore, mouse embryonic stem cells (mESC) served as exemplary mouse derived cell line. 3T3 cells, another well-established mouse line, turned out as an unsuitable example, since they lack an endogenous p22phox expression [16].

3.2.3.1.3. HMEC-1

The human microvascular endothelial cell line, HMEC-1 (ATCC CRL-3243) is a permanent cell line, derived from human dermal microvascular endothelial cells. The cell line was immortalised by transfection with a gene sequence of the simian virus A40, coding for the large T antigen [3].

The cells were cultivated in T75-flasks and grown under an atmosphere containing 5% CO₂ at 37°C in MCDB131 medium with 10% fetal calf serum, enriched for HMEC-1 growth with:

endothelial growth factor (EGF)	10 ng/ml
L-glutamine	2 nM
hydrocortisone	1 µg/ml
penicillin	100 U/ml
streptomycin	100 µg/ml

The medium was renewed every second day and the cells were passaged at 90% density, usually twice a week, by trypsinisation. After rinsing the cells with PBS, they were incubated with 3 ml 0.05% trypsin for about two minutes. The trypsinisation process was stopped by adding 5 ml medium. The released cells were collected, spun down for 5 min a 200 g, resuspended, subdivided in an adequate ratio and seeded into new T75-flasks for further growth or on dishes for further experiments.

3.2.3.1.4. Mouse embryonic stem cells

Mouse embryonic stem cells (mESC) are a primary cell line, taken in an early stage of mouse development. In our experiment, we used murine V6.5 embryonic stem cells [116]. These undifferentiated cells are not immortalized and should be held in culture not longer than for more than 30 passages, since chromosomal aberrations may occur more frequently. Undifferentiated cells need to be grown on feeder cells like mouse embryonic fibroblasts or on gelatine covered surfaces to inhibit spontaneous differentiation of the cells.

The embryonic stem cells were cultivated in T75-flasks at 37°C under an atmosphere of 5% CO₂ in Dulbecco's modified Eagle's medium (DMEM) supplemented as follows:

fetal calf serum	18%
Sodium pyruvate	1.2%
Non-essential amino acids (NEAA)	1.2%
penicillin	100 U/ml
streptomycin	100 µg/ml
β-Mercaptoethanol	0.016 µl/ml

Leukaemia inhibitory factor (LIF) was added freshly in a ratio of 1:1.000 prior to use. The medium was changed every second day and the cells were split twice a week by trypsinisation as described above. In contrast, stem cells needed a longer trypsin-incubation time of 5-10 min. The T75-flask and dish surfaces were immersed with 3-5 ml of 0.5%

gelatine solution. After 15 min of incubation, the supernatant was removed, and the gelatine cover left for another 5 min of air drying, before seeding the stem cells.

3.2.3.2. Hypoxia cell culture

To study the effect of hypoxia on the cellular level, HMEC-1 and mESC were exposed to hypoxic conditions of 1% oxygen in a hypoxia work station. Therefore, the cells were seeded in an appropriate number in 5 cm cell culture dishes and were placed in the prepared atmosphere in the hypoxia bench. The cells were incubated for different periods of time from 0.5 h up to 8 h, then the medium was removed, and the cell dishes were shock frozen with liquid nitrogen and stored at -80°C for further analysis.

3.2.3.3. Transfection of HMEC-1

To induce an artificial knockdown of p22phox, HMEC-1 were transfected with short interfering RNA (siRNA). These short RNA strands lead to the formation of the RNA-induced silencing complex (RISC), in which the siRNA binds a complementary mRNA strand, leading to its degradation. In consequence, mRNA levels are decreased and the protein translation is inhibited. For silencing of the p22phox gene, siRNA idSI03078523 by (Qiagen) was used. Furthermore, cells were transfected with AllStars negative control siRNA (Qiagen) and used as control cells.

The transfection was performed in 10 cm cell culture dishes at a density of about 70%. First, 20 µl of siRNA were mixed with 1000 µl of serum and antibiotic free MCDB and 20 µl of the transfection reagent Lipofectamin3000 were immersed with 1000 µl of serum and antibiotic free medium separately. The diluted RNA and Lipofectamine were combined, mixed by vortexing and left for incubation for about 30 min at RT. The transfection reagent forms small liposomes around the RNA that are able to fuse with cellular membranes of the living cells and hereby transport the captured RNA into the cells. Before transfection, the medium of the cells, normally supplemented as described above, was renewed with a volume of 8 ml. Finally, the transfection mix was added, and the cells were left for incubation for 48 hours before hypoxic stimulation. The final siRNA concentration was 20 µmol/ml.

3.2.4. Histology

Histological analysis is one of the basic and essential methods, in research as well as in daily clinical routine and diagnosis, analysing the morphology of tissues on the cellular level under the microscope. Therefore, tissue pieces are chemically treated to conserve their structure and allow the preparation of micrometre-thin slices. These slice are stained, since unstained tissue appears nearly invisible under the microscope. Different staining methods have been developed to enhance the contrast and mark specific structures of interest.

3.2.4.1. Standard procedures

The process of histological preparation of tissues is a complex procedure requiring several steps including fixation, processing, embedding, sectioning and staining. [5] Two main methods were used in this study – the formalin-paraffin fixation and the cryo-fixation.

3.2.4.1.1. Formalin fixation and paraffin embedding

The FFPE method is the standard procedure in daily histological routine. The tissue fixation was followed by a dehydration and an embedding process to finally replace the water within the tissue by paraffin. Afterwards the tissue was enclosed in paraffin blocks, allowing the final microtome sectioning. The sections were transferred on glass slides. Rehydration of the tissue sections was necessary, since most dyes are water soluble. The staining process was completed by sealing the tissue section with a coverslip.

Fixation:

Formalin or methanal is an organic chemical compound, belonging to the family of aldehydes. Working with formalin requires high caution as it is hazardous and toxic in many ways. Its biting vapours irritate conjunctiva and mucous membranes and can lead to bronchitis and pneumonia for example. Ingestion leads to strong inflammation or even sudden death [60].

A 4% formalin solution was used for fixation to preserve the tissue structure. Formalin cross-links proteins and preserves the cellular structure from autolysis. On the other hand, proteins lose their functional conformation. Furthermore, it leads to degeneration of DNA, RNA and miRNA [5]. Therefore, formalin fixed tissues are not useful for molecular analysis anymore.

For fixation, the collected animal organs were placed in histology cassettes and immersed in the 4% formalin solution for 48 h at RT.

Dehydration and embedding:

In the next step, the water in the tissue shall be removed and replaced by paraffin. Since alcohol has the ability to repress water, an ascending alcoholic row of isopropanol was used to replace the water in the tissue step by step.

Subsequently, the alcohol was replaced by the organic solvent xylene in turn. Finally the organic solvent was exchanged with paraffin [18]. The paraffin hardens the tissue which is an important precondition for the micro-sectioning.

The tissue processing was automatically performed by a dehydration machine. The carousel like machine consists of several canisters containing the alcohol row, the organic solvent and the molten paraffin. The cassettes were placed in a cage that was automatically transferred from canister to canister. The immersion time for each solution was set as follows:

Immersion time [h:min]	Solution
01:00	Formalin 4%
01:00	Formalin 4%
01:30	Isopropanol 70%
01:30	Isopropanol 80%
01:30	Isopropanol 96%
01:00	Isopropanol 100%
01:00	Isopropanol 100%
01:00	Isopropanol 100%
01:30	Xylene 100%
01:30	Xylene 100%
02:00	molten Paraffin
02:00	molten Paraffin

Isopropanol was diluted with distilled water.

Next, the dehydrated tissue was embedded in a paraffin block. Therefore, a tissue embedding system has been used, consisting of a paraffin dispenser and a cooling plate. Furthermore, metal forms of different sizes were required.

A small amount of molten paraffin was filled in the form, with the specimens positioned in the favoured way on the ground of the forms. The remaining form was filled with paraffin with the labelled cassette placed on top. The forms remained on the cooling plate until the blocks could be easily removed from their forms.

Sectioning:

The paraffin embedded specimens were sectioned with a rotary microtome. The moveable working table of the microtome, mounted with the paraffin block, allowed up- and downward and back- and forward movements. One full turn of the crank moved the table up and down once along the microtome blade. After one cycle the table was moved forward by a certain distance towards the blade, determining the thickness of the sections, that can be set by 0.5µm steps. Repetitive cycles created a ribbon of connected sections. The thickness of the slices depended upon the embedded tissue and usually lied around three to five micrometres.

The ribbons were split and transferred into a warm water bath of around 37°C where they flattened and stretched out. Floating on the surface they were scooped and mounted on a glass slide. Charged glass slides were used, enhancing the adhesion between slide and sections, providing more stability for further staining procedures. The slides were dried for several hours.

Rehydration:

For further processing the sections needed to be cleared from the paraffin, since the common staining procedures require a hydrophilic milieu. For rehydration the embedding procedure was reversed. After incubating the slides for 30 min at 60°C to melt the paraffin, the sections were immersed in a descending alcoholic row as follows:

Immersion time [min:sec]	Solution
05:00	Xylene 100%
05:00	Xylene 100%
03:00	Ethanol 100%
03:00	Ethanol 100%
03:00	Ethanol 90%
03:00	Ethanol 90%
03:00	Ethanol 70%
03:00	distilled water
03:00	distilled water

After immersion, the transfer cassette was left for some seconds to allow dripping of the solutions to reduce pollution of the row. Nevertheless, the solutions of the alcoholic row needed to be renewed frequently.

At the end of the staining procedure, the sections were sealed with a cover slide, using Entellan as mounting medium. It is a non-aqueous but organic solvent soluble mounting medium. Therefore, the stained sections were dehydrated again, using the alcoholic row in opposite direction. Taken directly from the last jar of xylene, a drop of mounting medium was applied on the sections and a fitting cover slide was placed on top. Attention must be paid to avoid enclosure of bubbles. The sealed sections were left overnight to allow hardening of the mounting medium.

3.2.4.1.2. Cryo fixation

Cryo fixation is another method for tissue fixation by rapid freezing down of the specimens. In this state, tissue is hard enough for cutting sections. The advantage lies in the quick processing, since no time-consuming paraffin embedding is necessary. In daily clinical routine, the frozen section analysis is mostly used for intraoperative diagnosis. Furthermore, the protein structure is not altered, which can be important for immuno-histological analysis. On the other hand, special equipment is necessary, as the whole cutting procedures needs to be performed at temperatures around -15°C . Besides, the section quality usually appears to be inferior compared to FFPE sections and the obtained slices are thicker. In this study, cryo fixation was used to prepare the organs for autoradiography.

Fixation and embedding:

Tissue specimens, shock frozen in liquid nitrogen or stored at -80°C were used for cryo cutting. The tissue pieces were placed in small disposable embedding cassettes in the required position. The specimens were embedded in special embedding medium. Tissue Tek OCT is a viscous liquid that hardens at temperatures below 0°C . Similarly to a paraffin block, it enclosed the tissue and provides a stable matrix for cutting. The frozen tissue block was mounted on a stamp, serving as specimen holder.

Sectioning:

For cutting of frozen tissue, a special cryostat rotary microtome was required, providing a stable working temperature of -15°C . The cutting process itself was similar to FFPE sectioning. In contrast the sections were directly mounted to the glass slides: the slides stored at RT were simply hold against the cut sections on the microtome table. They were drawn to the slide and fixed there, since the Tissue Tek melts immediately on the surface of the slide. The slides were stored at -20°C .

3.2.4.2. Staining

The staining process itself is the last essential step to process the tissue specimens for microscopic analysis. Besides the natural colour pigments melanin and haemoglobin, unstained tissue does not provide any contrast enhancing elements and appears nearly invisible in bright-field microscopy. Therefore, some kind of staining is necessary.

Staining methods can be distinguished by their basic mechanisms into two main groups: chemical staining and immunostaining.

3.2.4.2.1. Chemical staining

In chemical staining, the staining dyes react with different cell components and target different structures. These structures are highlighted in the final histological picture.

H&E staining

The hematoxylin and eosin staining is the routine standard staining in histology. It provides a good visualization of the tissue structure and a variety of pathologies can be identified already. The staining combines the two name-giving dyes hematoxylin and eosin (H&E). Hematoxylin reacts with the nucleic acids of the DNA and gives a blue-purple colour to the

cell nuclei. The pink eosin stains proteins non-specifically. Finally the typical image of H&E stained tissue presents with dark blue nuclei, whereas the cytoplasm and extracellular matrix appear in different shades of pink, dependent upon their composition [59].

The H&E staining was performed as follows:

Working step	Immersion time
immerse sections in Mayer's Hemalaun	15:00 min
transfer into Scott's Tap Water for blueing	02:00 min
rinse with distilled water	
immerse sections ins aqueous eosin solution 0.5%	03:00 min
rinse in with distilled water	
dehydrate as described above	

Scott's Tap Water was used as blueing solution. The alkaline pH ensures a reliable and crisp blue staining of the nuclei. 100 ml of the aqueous eosin solution 0.5% was laced with a drop of glacial acetic acid to counteract the alkaline pH from the blueing process.

3.2.4.2.2. Immunostaining

The working principle of immunostaining resembles western blot analysis of proteins. Antibodies are used to specifically target and visualize cellular structures. In clinical routine, immunostaining is an essential tool in cancer diagnostic, since the expression of surface antigens and alterations of cancer cells can be analysed.

Heat induced epitope retrieval (HIER):

FFPE sections needed a special heat induced epitope retrieval treatment, since formalin affects the protein structure. Therefore, the sections were immersed in a slide holder box with citrate antigen retrieval buffer (pH 6.0) or EDTA antigen retrieval buffer (pH 9.0) and cooked in the microwave for 20 min. HIER was performed pH 6.0 for the KI67/ α -smooth muscle actin double staining, and at pH 9.0 for CD31 staining.

Two different methods to visualize the binding antibodies have been used, that will be described in detail, the peroxidase and the fluorescence method.

Visualization by peroxidase staining

The rationale behind this method is a reaction of the chromogenic substrate DAB, mediated by an antibody linked peroxidase. In this study the avidin-biotin-complex (ABC) staining method was used. Hereby, the secondary antibody and the converting enzyme horseradish peroxidase (HRP) are biotinylated. The protein avidin can bind up to four biotinylation sites. The biotinylated HRP and the avidin are combined prior to the staining. In the kit used, two drops of reagent A and reagent B were mixed with 2.5 ml of PBS and incubated for 30 min to allow the formation of HRP-avidin complexes. The preformed complexes finally bind the biotinylation site of the secondary antibody and catalyse the reaction of the chromogenic substrate. The avidin-biotin-complex formation leads to a greater enzyme concentration at the antigen site with an increase in signal intensity [186] (Fig. 12).

This method was used in combination with the Dako α -smooth muscle actin antibody derived from mouse (M0581) to assess the muscularization of lung vessels. To rule out cross reactivity of the secondary antibody with endogenous antibodies, the Mouse on Mouse detection kit from Vector Labs was used.

Procedure:

The sections were prepared for the staining as described above. First, the endogenous peroxidase activity was blocked by incubating the slides with 0.3% H_2O_2 for 10 min, followed by washing steps with PBS for 5 min each. The surface of the slides was dried

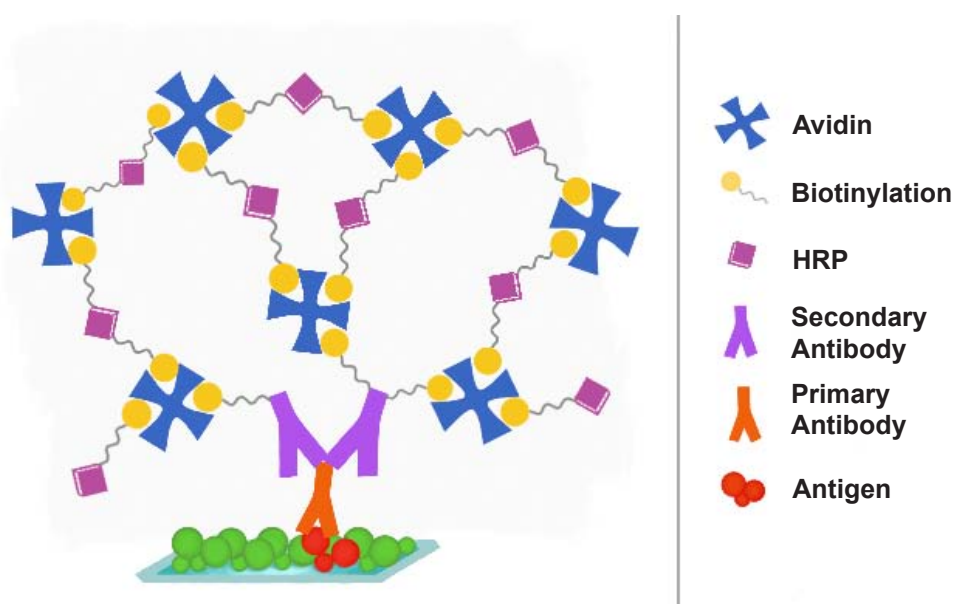


Figure 12 Schematic illustration of the ABC-staining method

The secondary antibody and the reporter enzyme horseradish peroxidase (HRP) are biotinylated. The protein avidin can bind up to four biotinylation sites, forming biotin-avidin complexes that lead to a greater enzyme concentration at the antigen site, enhancing the signal intensity. Adapted after [186].

carefully and a circle with the water repellent Dako pap pen was drawn around the sections on the slides. The hydrophobic border keeps the reagents within the circle, concentrates the reaction on the enclosed section, prevents mixture of solutions and reduces the amount of volumes necessary. The slides were blocked for one to two hours with 3% BSA in PBS in a humid chamber. Next, the sections were incubated with the working solution of the M.o.M. Ig blocking reagent to block endogenous antibodies for one hour. The slides were then incubated with the primary antibody. The α -smooth muscle actin antibody was diluted 1:100 with antibody diluent and applied on the specimens. After 30 min of incubation time in a humid chamber, slides were washed twice for 2 min with PBS, followed by incubation with the working solution of the biotinylated anti-mouse IgG reagent, targeting the primary antibody, for 10 min. The slides were washed twice for 2 min with PBS and the ABC reagent was applied for 5 min. The slides were washed again twice for 5 min before the peroxidase substrate was added and left for 5 min of incubation. The reaction of the chromogenic substrate could be observed as it turns dark brown. The supernatant substrate solution was removed completely with distilled water followed by two additional washing steps of 5 min as performed before. Finally, the sections were counterstained with Mayer's Hemalaun for 30 sec and incubated for 2 min in Scott's Tap Water for blueing. The slides were dehydrated and cover slipped as described above.

Visualization by fluorescence staining

The fluorescence method is another way for primary antibody detection in immunostaining. Hereby the secondary antibody is fluorescence labelled and can be visualized using a fluorescence microscope. The fluorophore has the ability to absorb light of one special wavelength and emit a light signal that is visualized in the end. Antibodies carrying different fluorophores can be combined in one specimen, since they can be distinguished by their individual excitation wavelengths. For visualizing the nuclei, the staining according to Hoechst has been used. This fluorophore binds to DNA and stains the nuclei independently from antibodies. It emits bright blue light at an excitation wavelength of 361 nm. The single images were combined in post procession.

Procedure:

The slides were prepared for the staining as described above. After drawing the hydrophobic reaction border, the slides were washed three times for 5 min with PBS, followed by blocking with 3% BSA dissolved in PBS for one to two hours in a humid chamber. After washing off

the blocking solution in PBS, the sections were incubated with one or two primary antibodies at 4°C overnight in a humid chamber, followed by two washing steps. The KI67 antibody was diluted at 1:1.000, the α -smooth muscle actin antibody at 1:125 and the CD31 antibody at 1:40. The corresponding secondary antibodies were diluted at 1:250 and applied for one to two hours incubation time at RT. All antibodies were diluted in Dako antibody diluent. The supernatant antibody solution was removed by three washing steps for 2 min each in PBS. The sections were incubated with Hoechst staining solution, diluted 1:10.000 for 1 min, followed by three washing steps for 2 min each with PBS.

The fluorescence stained slides were not dehydrated to protect the fluorescence labelled antibodies. Instead, Dako aqueous mounting medium was used to cover the slides.

3.2.4.2.3. Wheat germ agglutinin staining

The wheat germ agglutinin is a lectin that binds to cellular membranes. The staining was used to visualize the cell boundaries in mouse hearts to assess cardiomyocyte size. Therefore, fluorescence-labelled wheat germ agglutinin was used. Rhodamine, the coupled fluorophore, emits a red-light signal at 570 nm excitation wavelength.

Procedure:

FFPE slides were rehydrated and prepared as described above. The slides were immersed in the permeabilization buffer for 1 h to dissolve the cellular membranes and allow proper intercalation of the wheat germ agglutinin. The sections were washed three times for 2 min in PBS-Triton-Buffer subsequently. Non-specific fluorophore binding sites were blocked with the blocking buffer for 1 h. Next, the sections were stained in the WGA-working solution for 1 h at 37°C in dark. To remove supernatant staining solution, the slides were washed in PBS-Triton buffer three times for 2 min each. The counterstaining of the nuclei was performed with Hoechst staining solution, diluted 1:10.000 in PBS. Finally, the slides were washed three times for 2 min each in PBS and cover slipped with Dako aqueous mounting medium.

3.2.4.3. Evaluation

Bright field microscopic examination was performed using a "Zeiss Axioskop 2 plus" microscope. The digital processing and measurement of the obtained images was performed

with the "AxioVision" software, calibrated with stage micrometre. The evaluation of fluorescence staining was performed on an "Olympus IX50" microscope.

3.2.4.3.1. Heart – H&E staining

The aim of the measurement was to determine the ratio of the right ventricular and left ventricular wall thickness in order to check for right ventricular hypertrophy. The septum was selected as measurement side for the LV, since it provides an equal thickness, whereas the free wall of the LV is more uneven due to its muscular structure.

FFPE hearts were cut in transversal plane with a slice thickness of 3 μm and H&E stained for morphological evaluation as described above. Total heart images were taken with an objective of 1.25x magnification. Three measurements on the RV wall and the interventricular septum were carried out per heart. One mean value for the RV and LV thickness and consecutively a ratio for each heart was calculated.

To ensure the integrity of the septum as representative parameter for the left ventricle and to rule out the possibility of independent alterations of the septum, the obtained septum diameter was normalized to the total area of the left ventricle.

3.2.4.3.2. Heart – WGA staining

To examine the individual myocyte size in the right ventricle, FFPE hearts were cut in transversal plane with a slice thickness of 3 μm and stained with rhodamine labelled wheat germ agglutinin. Four HPF's of 40-fold objective magnification of the right ventricle were analysed in each heart. Thereby one HPF was covering an area of approximately 0.0375 mm^2 . The cell diameter of ten myocytes, cut in longitudinal axis, was measured in each HPF, thus 40 individual values were obtained from each heart. In total, the cells of three hearts have been analysed. From the individual myocyte values a mean value with standard deviation and standard error was calculated for each experimental group.

3.2.4.3.3. Lung – α -smooth muscle actin staining

Sections of 3 μm thickness of FFPE lungs were prepared and stained against α -smooth muscle actin as described above. For evaluation and quantification of the immune-reactive vessels, four HPFs of 10-fold objective magnification, covering each an area of approximately 0.6 mm^2 , were analysed in each lung. All α -smooth muscle actin positive vessels have been measured and, based on their diameter, assigned to one of three groups:

0-30 μm , 30-60 μm and $>60\mu\text{m}$. The results were expressed as number of immune-reactive vessels in four high power fields per analysed lung. Five lungs were analysed in each experimental group.

Due to the smaller experimental group in the NOX1-K.O. mice experiment, the quantification of the vessels was calculated as “number of positive vessels per HPF”, compared to “number of positive vessels per 4 HPFs” in NMF333 mice.

3.2.4.3.4. Lung – KI67/ α -smooth muscle actin double staining

The KI67 immunostaining was performed to analyse the proliferative activity in the context of vascular remodelling in hypoxic mice. Hence, it was used in combination with the α -smooth muscle actin staining. To assess the proliferation index of the remodelled vessels, the number of vessels, which were double positive for KI67 and α -smooth muscle actin were set in relation to the number of single positive vessels (only α -smooth muscle actin positive), counted in three high power fields per lung. Only hypoxic lungs were analysed, since vascular remodelling is not present under normoxic conditions.

3.3. Statistics

The values were presented as means with standard error. Unpaired and two-sided student's t-test of the mean was performed to check for statistical significance. A p-value < 0.05 was accepted as significant.

4. Results

4.1. Link between hypoxia and p22phox

The state of hypoxia was described to increase the levels and activity of the ROS producing NADPH oxidases [47, 157, 214]. Among the five NOX isoforms NOX1 to NOX4 share the essential subunit p22phox [151]. We therefore aimed to study the effect of hypoxia on the expression of p22phox.

4.1.1. Regulation of p22phox gene expression by hypoxia

To assess whether hypoxia influences p22phox mRNA levels human microvascular endothelial cells (HMEC-1) and mouse embryonic stem cells (mESC) were exposed to hypoxia (1% oxygen) for varying time periods. P22phox mRNA levels were not significantly altered by hypoxia in HMEC-1 cells. The small dip after one hour was tested as statistically not significant (Fig. 13a) [215]. In contrast, in mESC, p22phox mRNA levels were lower under hypoxia than under normoxia (Fig. 13b). P22phox gene expression was decreased by 60% already at 0.5 h of exposure to hypoxia and remained downregulated until

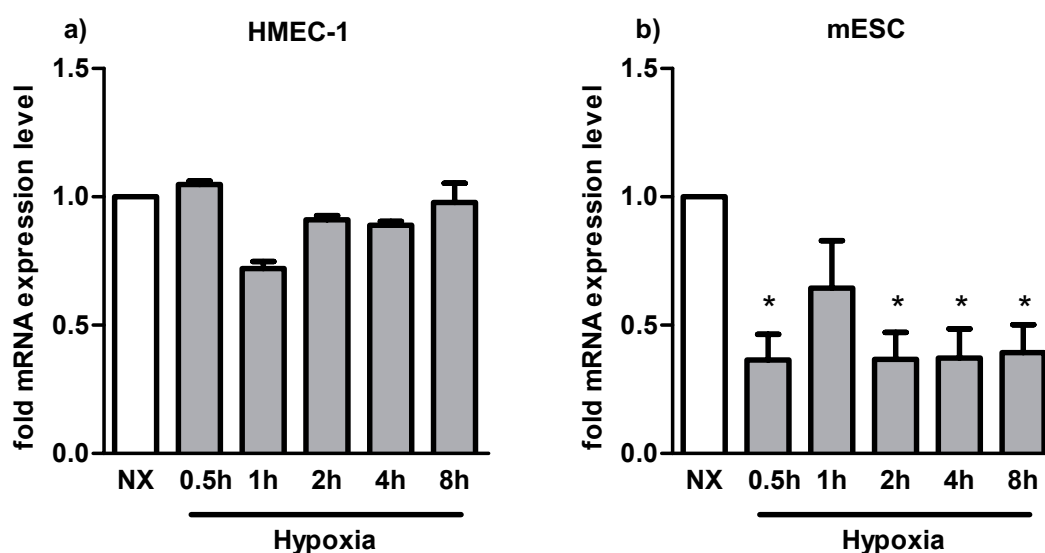


Figure 13 Hypoxia decreases p22phox mRNA levels in mESC

Quantitative PCR was performed for p22phox from cDNA derived from a) human microvascular endothelial cells (HMEC-1) and b) mouse embryonic stem cells (mESC). Cells were exposed to hypoxia (1% oxygen) for the given periods of time. Relative mRNA levels were calculated using β -actin as reference gene and normoxia (NX) as reference condition. Values are presented as mean \pm SEM; n=3; * $p < 0.05$ compared to NX [215].

8 h of hypoxia, although at 2 h p22phox mRNA levels were not significantly different under hypoxia and normoxia.

4.1.2. Regulation of p22phox protein levels by hypoxia

To assess, whether p22phox protein levels are affected by hypoxic stimulation, human microvascular endothelial cells (HMEC-1) (Fig. 14a & c) and mouse embryonic stem cells (mESC) (Fig. 14b & d) were exposed for different periods of time to hypoxic conditions (1% oxygen). Western blot analyses revealed, that p22phox protein levels were transiently increased in both cell lines, starting already after 0.5 h of stimulation while they returned to baseline levels at four hours in HMEC-1 cells and at eight hours in mESC [215]. These results suggest, that p22phox is differentially regulated on protein and mRNA levels by hypoxia.

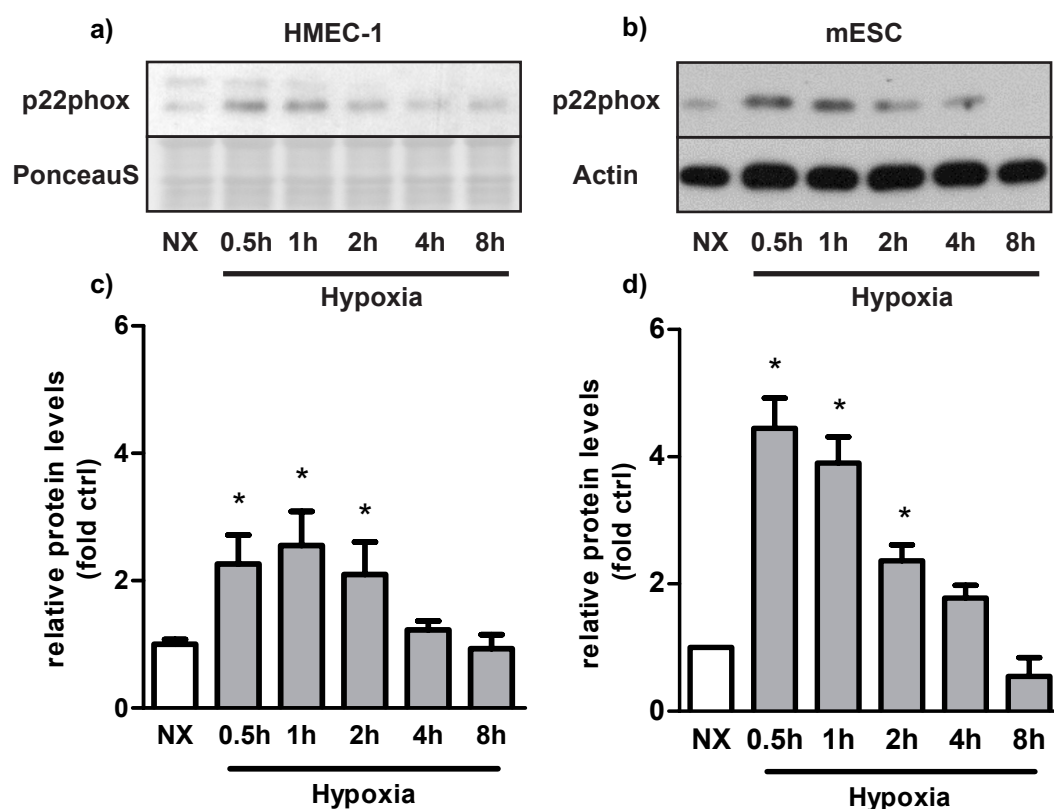


Figure 14 Hypoxia increases p22phox protein levels

Western blot analysis was performed for p22phox in a) human microvascular endothelial cells (HMEC1) and b) mouse embryonic stem cells (mESC) exposed to hypoxia (1% oxygen) for the given periods of time. PonceauS and β -actin served as loading control. Quantification of Western blot analysis is shown in graphs c) for HMEC-1 and d) for mESC. Values are presented as mean \pm SEM; $n=3$; * $p<0.05$ compared to normoxia (NX) [215].

4.2. Characterization of the NMF333 mouse line

The NMF333 mouse strain was described in 2008 by Nakano et al. to carry a Y121H point mutation in the *Cyba* gene, which codes for p22phox [144]. These mice presented with a characteristic phenotype – a tilted head position, due to an impaired sense of balance. Furthermore, they were described to lack the so called respiratory burst due to a loss of p22phox protein and superoxide production in neutrophils, thus resulting in a deficiency in the innate immune system similar to chronic granulomatous disease (CGD) described in humans. Since p22phox is an ubiquitously expressed protein [105], we aimed to analyse whether the Y121H mutation would also affect other cells and organs apart from neutrophils.

4.2.1. P22phox gene expression in NMF333 mice

To test the effect of the Y121H mutation on the p22phox mRNA expression in different mouse organs, quantitative PCR was performed in spleen, liver, lung, heart, kidney and skeletal muscle obtained from wildtype and NMF333 mice (Fig. 15).

P22phox mRNA levels were not influenced by the Y121H mutation since no significant differences were found between wildtype and NMF333 mice. A tendency to increased mRNA levels in liver and reduced mRNA levels in heart of NMF333 mice did not reach statistical significance.

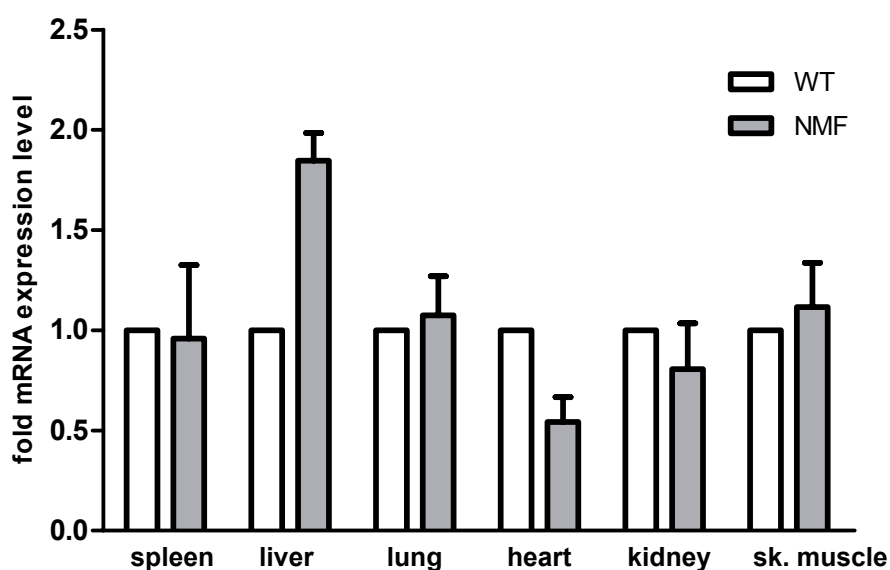


Figure 15 The Y121H mutation does not affect p22phox mRNA levels

Quantitative PCR was performed from cDNA of different mouse organs obtained from wildtype (WT) and NMF333 mice (NMF) for p22phox and related to β -actin as reference gene. P22phox mRNA levels in WT mice served as reference condition. Values are presented as mean \pm SEM; n=3 (sk. muscle – skeletal muscle).

4.2.2. P22phox protein levels in NMF333 mice

In a next step p22phox protein levels were tested in spleen, liver, kidney, heart and lung obtained from wildtype and NMF333 mice. Western blot analyses were performed in tissue lysates as well as in PBMCs which served as control. (Fig. 16).

Compared to wildtype mice, p22phox protein levels were almost not detectable in PBMCs [215] and spleen from NMF333 mice, while p22phox protein was present at equal levels in kidneys from both, WT and mutant mice. P22phox protein could not be detected in liver, lung and right ventricular tissue (RV) from WT and NMF333 mice.

These results suggest that the Y121H point mutation compromises only the p22phox protein levels, whereas the p22phox gene expression remained unaffected.

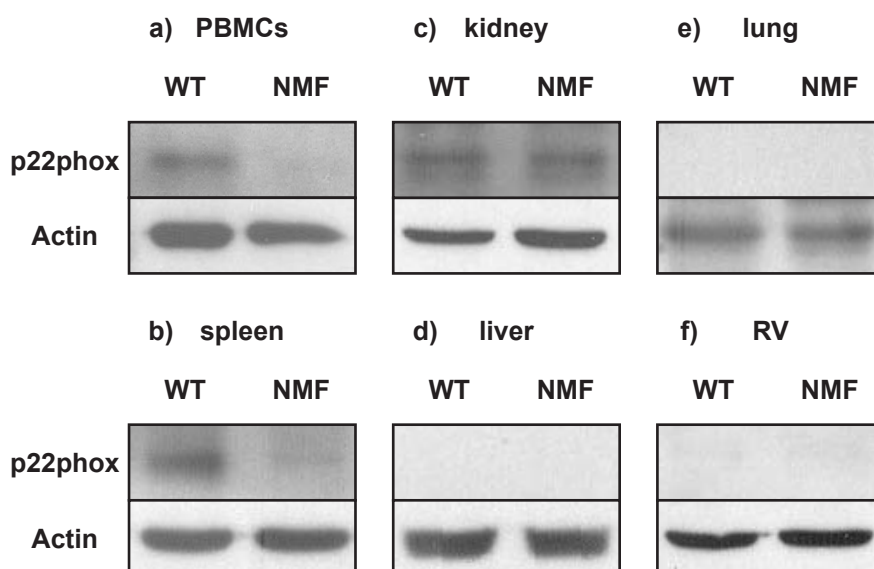


Figure 16 P22phox protein levels are reduced in different organs from NMF333 mice
 Western blot analysis for p22phox was performed in a) peripheral blood mononuclear cells (PBMCs) [215]; b) spleen; c) kidney; d) liver; e) lung and f) right ventricle (RV) obtained from wildtype (WT) and NMF333 (NMF) mice. β -Actin served as loading control; n=2-3.

4.2.3. ROS production in mononuclear cells

Next, the consequences of the loss of p22phox protein on the ROS production rate was tested in PBMCs derived from wildtype and NMF333 mice in comparison using electron paramagnetic resonance (EPR) with CMH as spin trap.

PBMCs derived from NMF333 mice were found to have a significantly reduced ROS production rate of 0.28 nM/10min/10⁻³cells compared to 0.43 nM/10min/10⁻³cells measured in PBMCs derived from WT mice (Fig. 17) [215]. These results indicate that the Y121H point mutation is connected with both, reduced p22phox protein levels and a decreased ROS production in PBMCs.

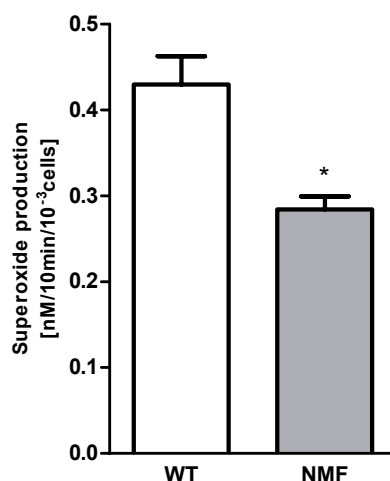


Figure 17 Basal superoxide generation is decreased in NMF333 peripheral blood mononuclear cells
 The superoxide production rate was assessed for 10 min by EPR using CMH as spin trap in PBMCs obtained from wildtype (WT) and NMF333 (NMF) mice. Values are presented as mean \pm SEM; n=3-10; * $p < 0.05$ NMF vs. WT [215].

4.2.4. Vessel-forming capacity in wildtype and NMF333 mice

Besides their role in immune defence, ROS have been described to play an important role as mediators and modulators in different signalling pathways, such as angiogenesis [22, 70, 192]. To evaluate, if NMF333 mice show differences in their vessel forming capacity compared to WT mice, an in vivo Matrigel sprouting assay was performed. Liquid Matrigel matrix, enriched with or without the angiogenesis promoting hormone “platelet derived growth factor” (PDGF) [42] was injected s.c. into WT and NMF333 mice. After 14 days, the Matrigel-plugs were isolated and stained with DAPI to label cell nuclei and with an antibody against CD31, a marker for endothelial cells (Fig. 18). The Matrigel-plugs without growth factor did not show a clear sprouting of endothelial cells, neither in WT nor in

NMF333 mice. In contrast, PDGF enriched plugs obtained from WT mice showed a distinct formation of CD31 positive cells, forming network-like structures. On the contrary, PDGF enriched Matrigel-plugs, isolated from NMF333 mice, did not show comparable CD31 positive cells or cellular structures, suggesting a reduced vessel-forming capacity in NMF333 mice [215].

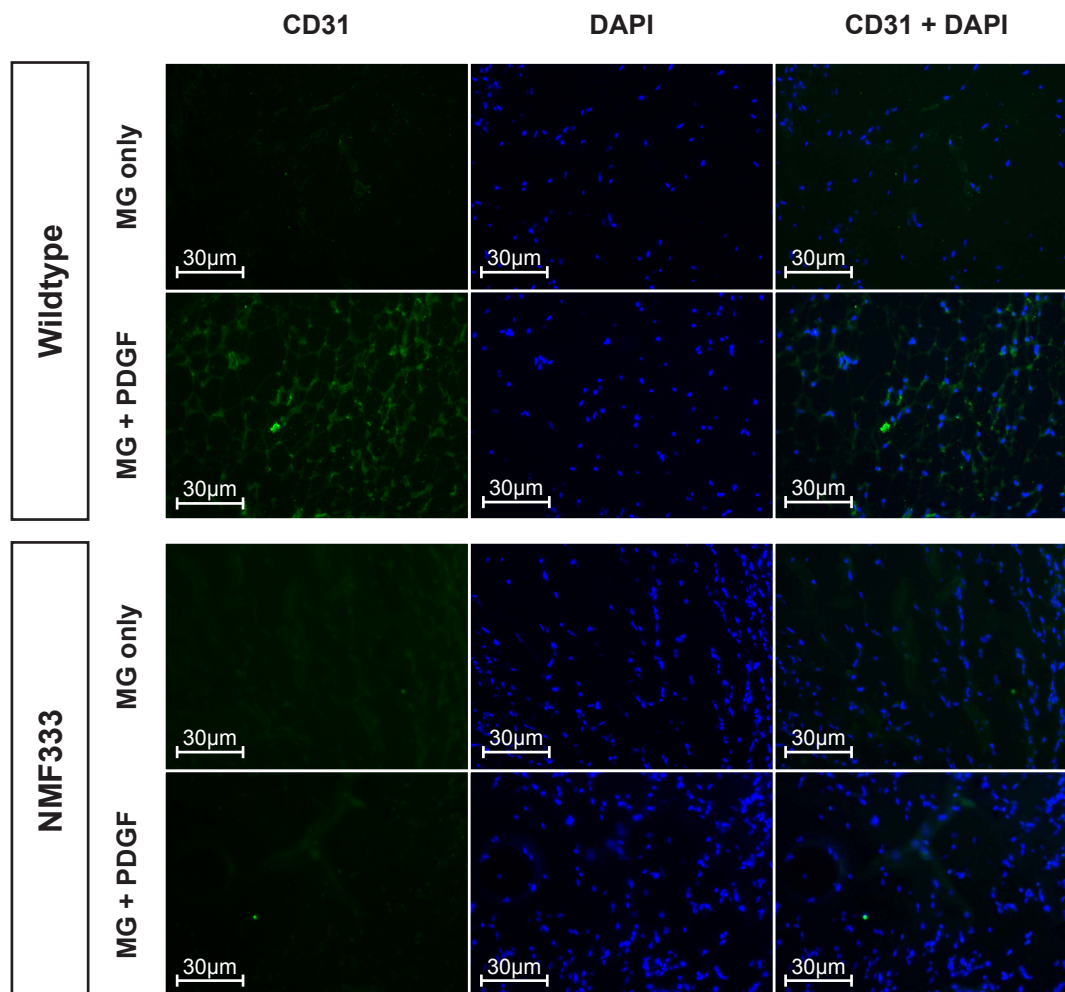


Figure 18 Vessel forming capacity is reduced in NMF333 mice

Matrigel plugs (MG), with or without 100 nM platelet derived growth factor (PDGF), were implanted in the subcutis of wildtype and NMF333 mice. After 14 days the Matrigel plugs were excised and stained with an antibody against CD31 (green) and with DAPI (blue). Representative microscopic images were taken at 20-fold magnification. Scale bar = 30 μ m [215].

4.3. Effect of chronic hypoxia on NMF333 and WT mice

Since hypoxia was able to upregulate p22phox in cell culture and the Y121H mutation in NMF333 mice was associated with decreased p22phox protein levels, it was next tested whether the p22phox mutation would also have effects on the in vivo response of mice towards exposure to chronic hypoxia. To this end wildtype and NMF333 mice were exposed to 10% oxygen for three weeks.

4.3.1. Blood parameters

To analyse, whether the Y121H mutation of the NMF333 mice affected the general haematological response to chronic hypoxia, a routine blood work was obtained. The platelet count under normoxic conditions was significantly higher in NMF333 than in WT mice.

Hypoxia increased the red blood count, haemoglobin levels, haematocrit as well as mean corpuscular volume (MCV) and mean corpuscular haemoglobin (MCH) levels in both mouse lines to a similar extent. The platelet counts significantly dropped by around 40% in WT and by 50% in NMF333 mice, going along with the hypoxia-induced thrombocytopenia described in mice [17]. The white blood cell count remained unaffected by genotype and oxygen concentration.

Table 1 Routine blood work obtained from wildtype and NMF333 mice

	WT/NX	NMF/NX	WT/HX	NMF/HX
WBC (*10 ³ /μl)	2.8 ± 0.9	2.0 ± 0.5	2.8 ± 0.9	2.2 ± 0.8
RBC (*10 ⁶ /μl)	8.13 ± 1.04	7.80 ± 0.42	11.54 ± 0.83 ^a	11.42 ± 0.61 ^a
HGB (g/dl)	12.3 ± 1.5	11.8 ± 0.5	18.0 ± 1.3 ^a	18.0 ± 1.1 ^a
HCT (%)	41.0 ± 5.5	39.9 ± 2.0	62.7 ± 4.4 ^a	63.0 ± 5.2 ^a
MCV (fl)	50.5 ± 2.4	51.2 ± 2.1	54.4 ± 3.2 ^a	55.2 ± 2.4 ^a
MCH (pg)	15.1 ± 0.7	15.2 ± 0.7	15.9 ± 1.0	15.7 ± 0.3 ^a
MCHC (g/dl)	29.9 ± 0.7	29.6 ± 0.8	28.8 ± 2.0	28.6 ± 1.7
PLT (*10 ³ /μl)	615 ± 216	914 ± 232 ^b	368 ± 149 ^a	455 ± 271 ^a

Values are presented as mean ± SD; n=9-11; a p < 0.05 HX vs. NX; b p < 0.05 NMF333 vs. WT. (WBC – white blood cell count; RBC – red blood cell count; HGB – haemoglobin; HCT – haematocrit; MCV – mean corpuscular volume; MCH – mean corpuscular haemoglobin; MCHC – mean corpuscular haemoglobin concentration; PLT – platelet count; NX – normoxia; HX – hypoxia; WT – wildtype mice; NMF – NMF333 mice).

4.3.2. P22phox gene expression in hypoxic mice

P22phox mRNA expression levels in lung (Fig. 19a) and RV tissue (Fig. 19b) from hypoxic and normoxic wildtype and NMF333 mice were analysed using quantitative PCR. Hereby, no significant p22phox gene regulation was found, neither by genotype nor by hypoxia.

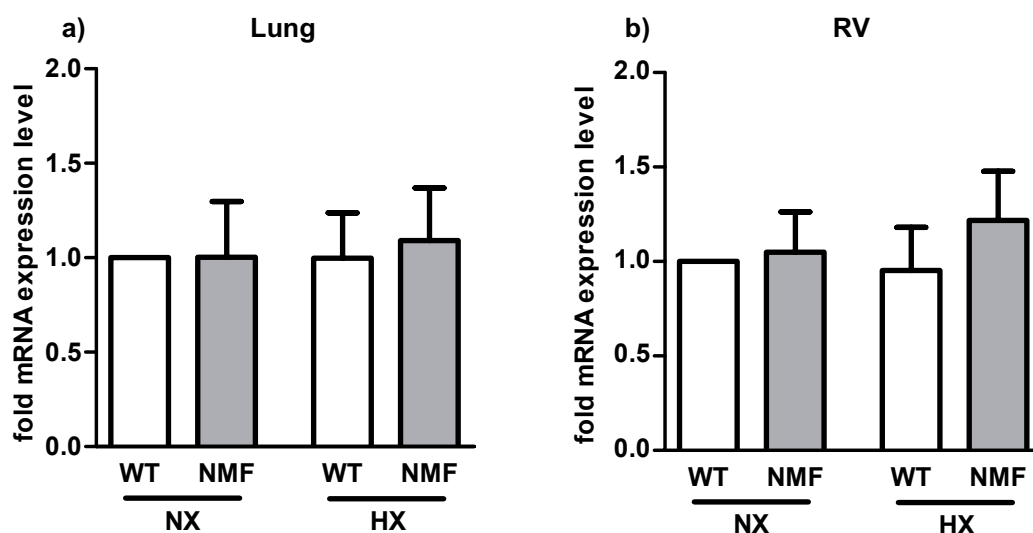


Figure 19 P22phox mRNA levels are not affected by hypoxia or the Y121H mutation

Quantitative PCR was performed for p22phox from cDNA derived from a) lung and b) right ventricular (RV) tissue of wildtype (WT) and NMF333 (NMF) mice exposed to chronic hypoxia (HX, 10% oxygen) for three weeks or to normoxic conditions (NX). Relative mRNA levels were calculated using β -actin as reference gene and NX/ WT mice as reference condition. Values are presented as mean \pm SEM; n=3; * $p < 0.05$ compared to reference condition.

4.3.3. P22phox protein levels in hypoxic mice

Furthermore, Western blot analysis of p22phox was performed in lung (Fig. 20a & c) and right ventricular tissue from wildtype and NMF333 mice (Fig. 20b & d) [215].

Under normoxic conditions, p22phox protein was barely detectable in these tissues in both, WT and NMF333 mice. Exposure to chronic hypoxia led to a strong induction of p22phox protein levels in WT tissues. Western blot quantification revealed a significant increase between WT normoxic and hypoxic levels by 2.0-fold in lung tissue and by even 5.3-fold in right ventricular tissue. However, in NMF333 mice, p22phox protein induction was substantially lower in RV tissue and completely absent in lung tissue. Western blot quantification showed that hypoxia increased p22phox levels in NMF333 mice only by around 1.5-fold in RV tissue, but decreased p22phox protein levels by factor 0.5 in lung tissue.

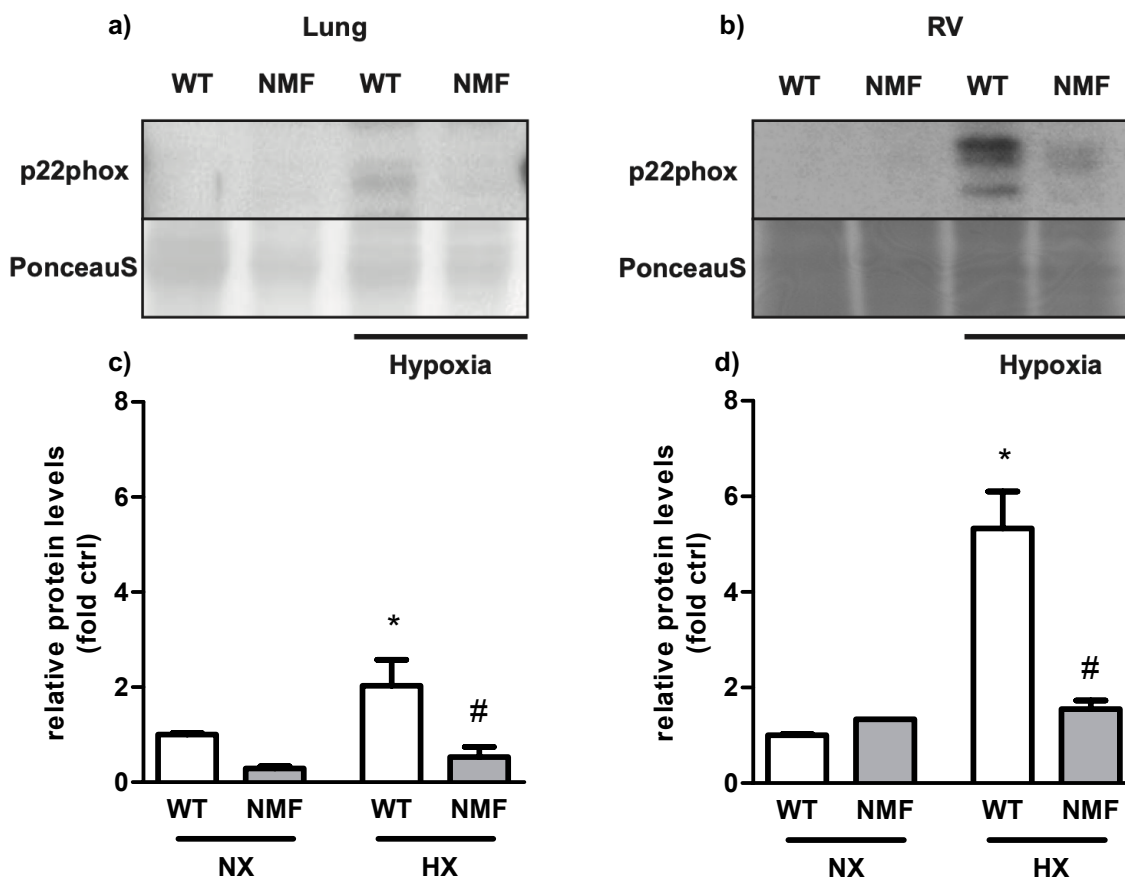


Figure 20 Hypoxic induction of p22phox protein is reduced in NMF333 mice

Western blot analysis was performed for p22phox in a) lung and b) right ventricular (RV) tissue obtained from wildtype (WT) and NMF333 (NMF) mice exposed to chronic hypoxia (HX, 10 % oxygen) for three weeks or normoxic conditions (NX). PonceauS served as loading control. Quantification of Western blot analysis is shown in graphs c) for lung and d) for RV. Values are presented as mean \pm SEM; $n=3$; * $p<0.05$ HX vs. NX; # $p<0.05$ NMF vs. WT [215].

4.3.4. Haemodynamic measurements in normoxic and hypoxia-stimulated mice

To evaluate the effect of the Y121H mutation on left and right ventricular pressure, haemodynamic measurements were performed in NMF333 and wildtype mice kept for three weeks at 10% oxygen (hypoxia) or under normoxic conditions (Fig. 21) [215]. Under normoxic conditions, right ventricular (RV) and left ventricular (LV) pressure values did not differ between WT and NMF333 mice: the right ventricular pressure was measured at around 16 mmHg over 8 mmHg resulting in a mean arterial pressure (MAP) of 11 mmHg in both mouse lines, whereas the left ventricular pressure was measured at 60 mmHg over 36 mmHg with a MAP of 44 mmHg.

After exposure to hypoxic conditions, the right ventricular systolic pressure in WT mice rose significantly to 26 mmHg, whereas in NMF333 mice the right ventricular systolic pressure increased to only 22 mmHg. Thus, the increase of the systolic pressure in response to hypoxia was about 40 % lower in NMF333 mice compared to their wildtype littermates.

The diastolic RV pressure increased around 6 mmHg from 8 to 14 mmHg in WT mice in response to hypoxia, whereas in NMF333 mice the diastolic RV pressure only increased from 8 to 9 mmHg. Hence, the MAP in the RV in WT mice rose around 7 mmHg from 11 to 18 mmHg, while the MAP in the RV in NMF333 mice increased only by 3 mmHg from 11 to 14 mmHg. Thus, the increase of the MAP in the RV was about 57% lower in p22phox-deficient NMF333 mice compared to WT mice.

The LV systolic pressure rose around 4 mmHg in both, WT and NMF333 mice. This change did not prove to be statistically significant. The LV diastolic pressure in WT mice increased by 5 mmHg from 36 to 41 mmHg, whereas in NMF333 mice it increased only by 3 mmHg from 36 mmHg to 39 mmHg. The increase in LV diastolic pressure in WT mice in response to hypoxia was tested as statistically significant, the change in NMF333 mice proved to be not significant. The left ventricular MAP rose around 5 mmHg from 44 to 49 mmHg in WT mice and around 3 mmHg from 44 to 47 mmHg in NMF333 mice. Again, the change in WT, but not in NMF333 mice was tested as statistically significant.

The data presented show that NMF333 mice developed significantly lower pressure values in the right ventricle under chronic hypoxia compared to their WT littermates.

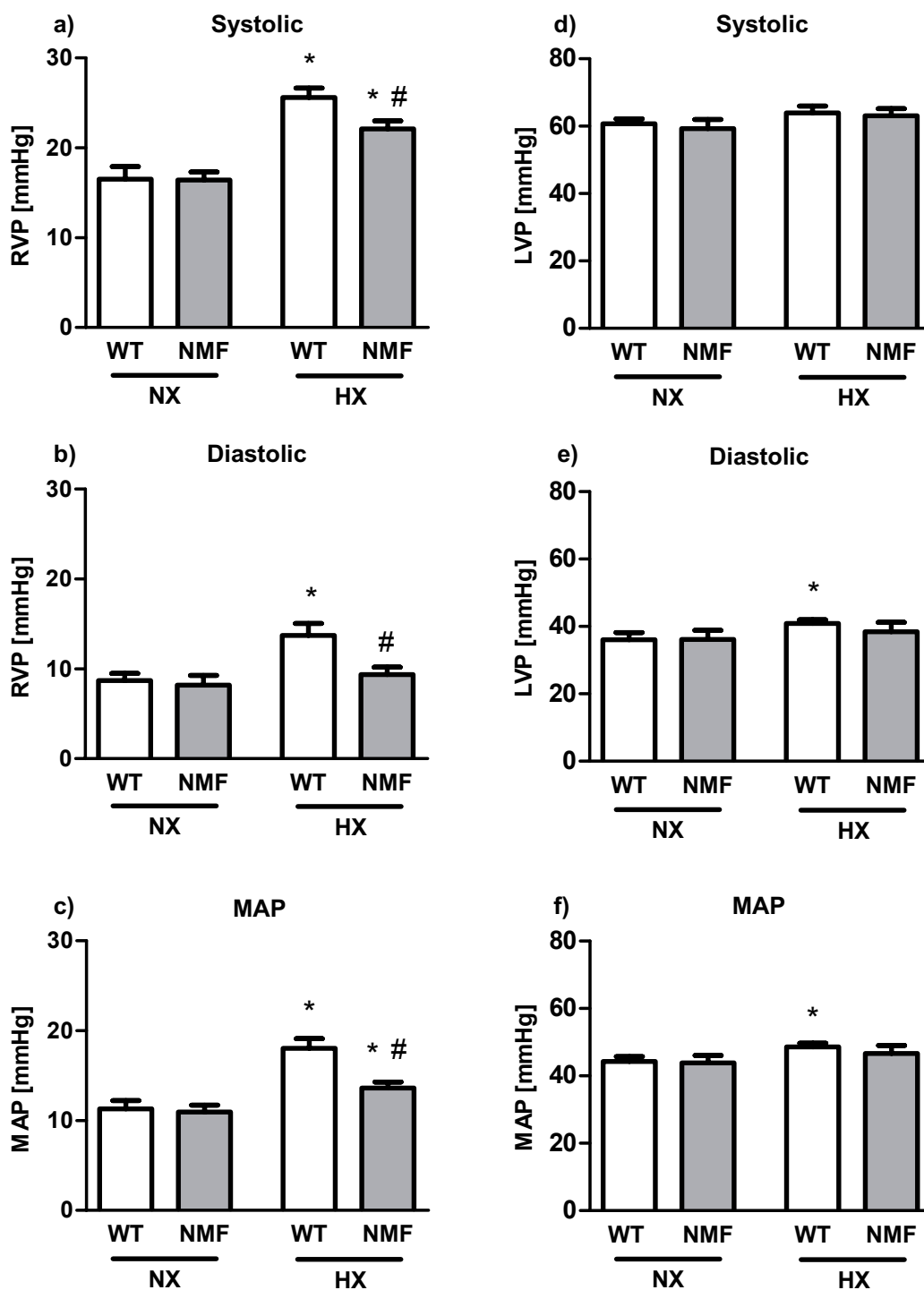


Figure 21 NMF333 mice do not develop hypoxia-induced pulmonary hypertension

Haemodynamic pressure values were obtained from wildtype (WT) and NMF333 (NMF) mice exposed either to chronic hypoxia (HX, 10% oxygen) for three weeks or to normoxic conditions (NX) using a trans-thoracically introduced tip catheter system. a) systolic right ventricular pressure (RVP), b) diastolic RVP, c) mean arterial pressure (MAP) from RV, d) systolic left ventricular pressure (LVP), e) diastolic LVP, f) MAP from LV. Values are presented as mean \pm SEM; n=10-12; * $p < 0.05$ HX vs. NX; # $p < 0.05$ NMF vs. WT [215].

4.3.5. Cardiac responses to chronic hypoxia

It is known, that an increase in right ventricular pressure can lead to a hypertrophic reaction of the right ventricular myocardium. Therefore, we aimed to assess whether wildtype and NMF333 mice exposed to hypoxia would develop right ventricular hypertrophy by determining the ventricular mass, the diameter of the right ventricular wall and the diameter of individual myocytes of the right ventricle, as well as by measuring β -MHC expression.

4.3.5.1. Determination of ventricular mass

To test whether chronic hypoxia leads to ventricular hypertrophy, right ventricular and left ventricular mass were determined and related to the body mass.

While left ventricular mass remained unchanged by either genotype or hypoxia treatment (Fig. 22b), the relative right ventricular mass was significantly increased in WT mice exposed to hypoxia from 0.86 to 1.3. In comparison, the relative right ventricular mass of NMF333 mice increased about 35% less to only 1.15 (Fig. 22a). No differences were observed under normoxic conditions.

In line, the Fulton's index, described as ratio between the mass of the right ventricle and the left ventricle including the septum, was significantly higher in hypoxic wildtype mice compared to hypoxic NMF333 mice (Fig. 22c). In WT mice exposed to chronic hypoxia it increased from 0.24 to 0.36 and in NMF333 mice from 0.25 to 0.31. Thus, the increase of the Fulton index in response to hypoxia was approximately 50% less in NMF333 mice than in WT mice [215]. The Fulton's indices of WT and NMF333 mice did not differ under normoxic conditions.

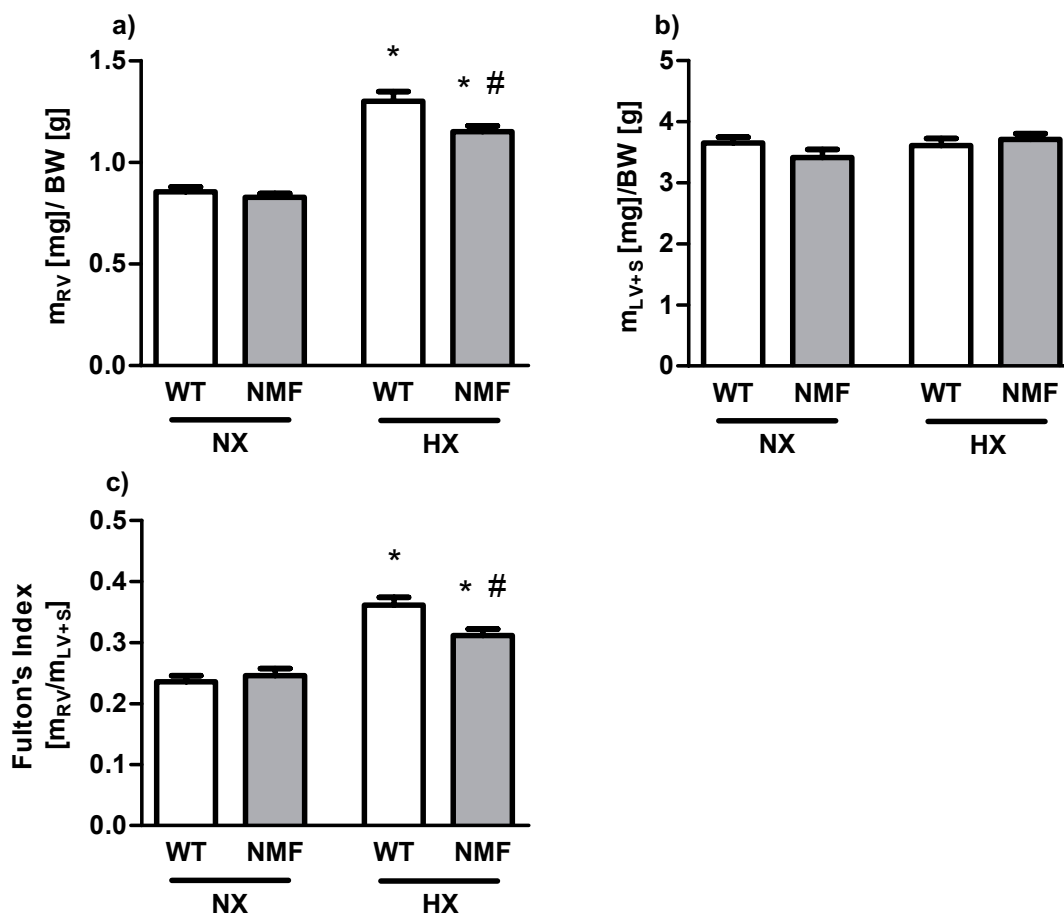


Figure 22 Hypoxic induction of right ventricular mass is reduced in NMF333 mice

The ventricular mass was determined in wildtype (WT) and NMF333 (NMF) mice exposed to normoxia (NX) or chronic hypoxia (HX, 10% oxygen) for three weeks. a) Ratio between right ventricular mass (m_{RV}) and the bodyweight (BW) of the mice and b) ratio between left ventricular mass including the septum (m_{LV+s}) and BW of the mice. c) Fulton's index was expressed as ratio between RV mass and LV mass including septum. Values are presented as mean \pm SEM; $n=10$; * $p < 0.05$ HX vs. NX; # $p < 0.05$ NMF vs. WT [215].

4.3.5.2. Ventricular wall diameter

To further determine the effect of chronic hypoxia on cardiac size, right and left ventricular wall diameter were assessed in microscopic images of total heart cross sections stained with H&E.

Representative heart cross sections of WT and NMF333 mice under normoxic and hypoxic conditions are shown in (Fig 23a) [215]. The ratio between the RV and the LV wall diameter of wildtype and NMF333 mice were alike under normoxic conditions. After exposure to chronic hypoxia, the RV/LV diameter ratio was significantly increased in WT mice from 0.36 to 0.60 and in NMF333 mice from 0.37 to 0.47. Similar to the Fulton's index, the increase of the RV/LV wall diameter ratio measured in hypoxic NMF333 mice was about 58% less compared to hypoxic WT mice (Fig. 23b) [215].

To rule out independent structural alterations of the septum due to chronic hypoxia, the acquired septum diameter was normalized to the total area of the left ventricle (Fig. 23c). The septum/LV area ratio was not altered by chronic hypoxia, neither in WT nor in NMF333 mice, proofing the integrity of the septum as part of the left ventricle [215].

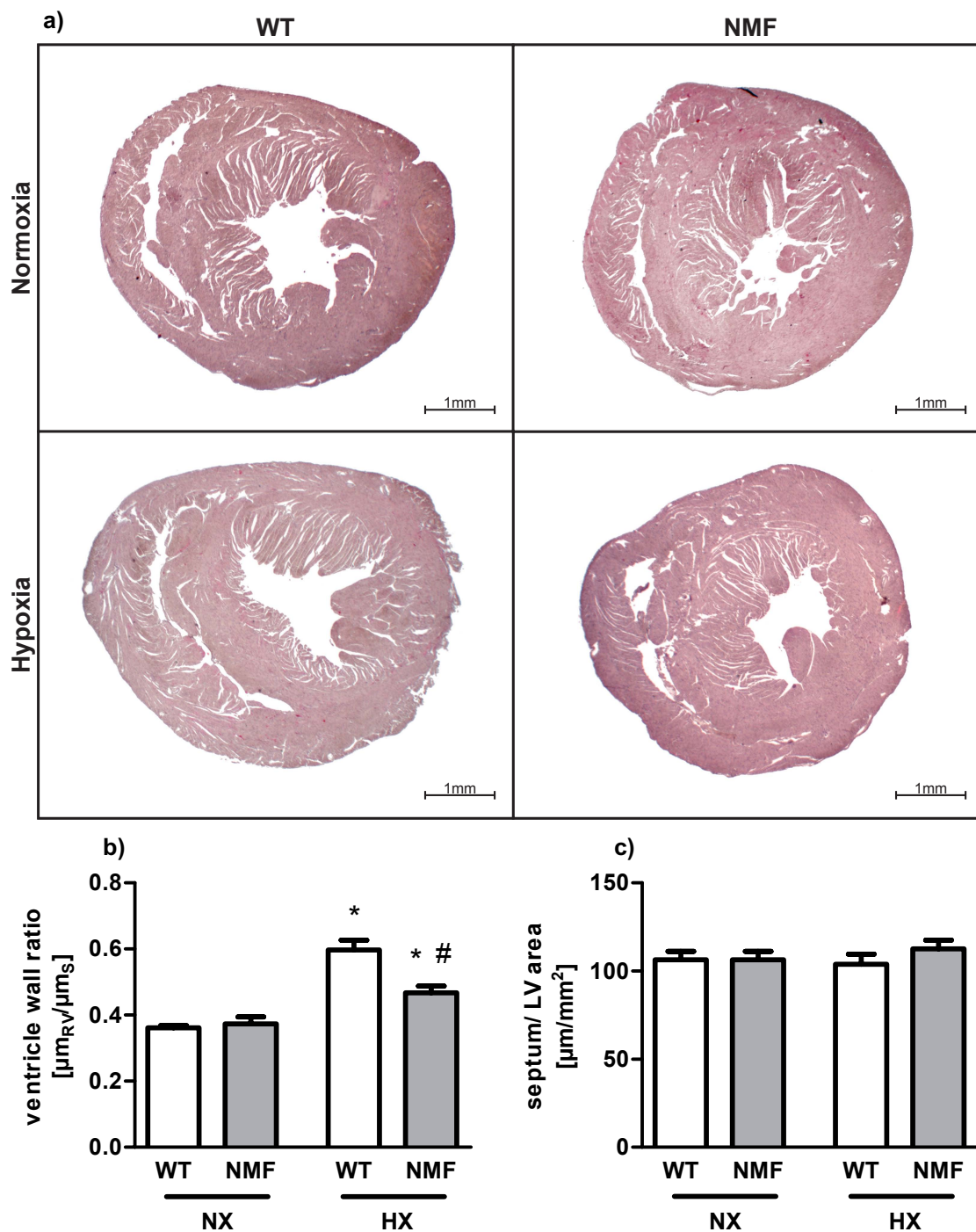


Figure 23 Right ventricular wall thickness is reduced in hypoxic NMF333 mice

a) Representative microscopic images of heart transversal plain sections from wildtype (WT) and NMF333 (NMF) mice, exposed to chronic hypoxia (HX, 10% oxygen) for three weeks or normoxic conditions (NX), stained with H&E at 1,25-fold magnification. b) Quantification of ventricular wall thickness: right ventricular (RV) wall diameter was normalized to the left ventricular (LV) wall diameter measured at the septum. c) LV wall diameter measured at the septum was normalized to the total area of the LV. Values are presented as mean \pm SEM; n=5; * p<0.05 HX vs. NX; # p< 0.05 NMF vs. WT; scale bar = 1 mm [215].

4.3.5.3. Size determination of cardiomyocytes

To further assess hypertrophy of the right ventricle in response to chronic hypoxia, the diameter of individual cardiomyocytes of the right ventricle was assessed in longitudinal sections by staining the cellular borders with WGA (Fig. 24a) [215].

Under normoxic conditions wildtype and NMF333 mice presented with similar values: the mean diameter of WT cardiomyocytes was $9.7 \mu\text{m}$ and of NMF333 cardiomyocytes $9.4 \mu\text{m}$. In response to three weeks of chronic hypoxia, the mean diameter of WT cardiomyocytes increased up to $13.6 \mu\text{m}$, whereas the diameter of NMF333 cardiomyocytes increased only up to $12.1 \mu\text{m}$, thus being a relative reduction by 31% of the diameter of hypoxic NMF333 cardiomyocytes compared to hypoxic WT cardiomyocytes (Fig. 24b) [215].

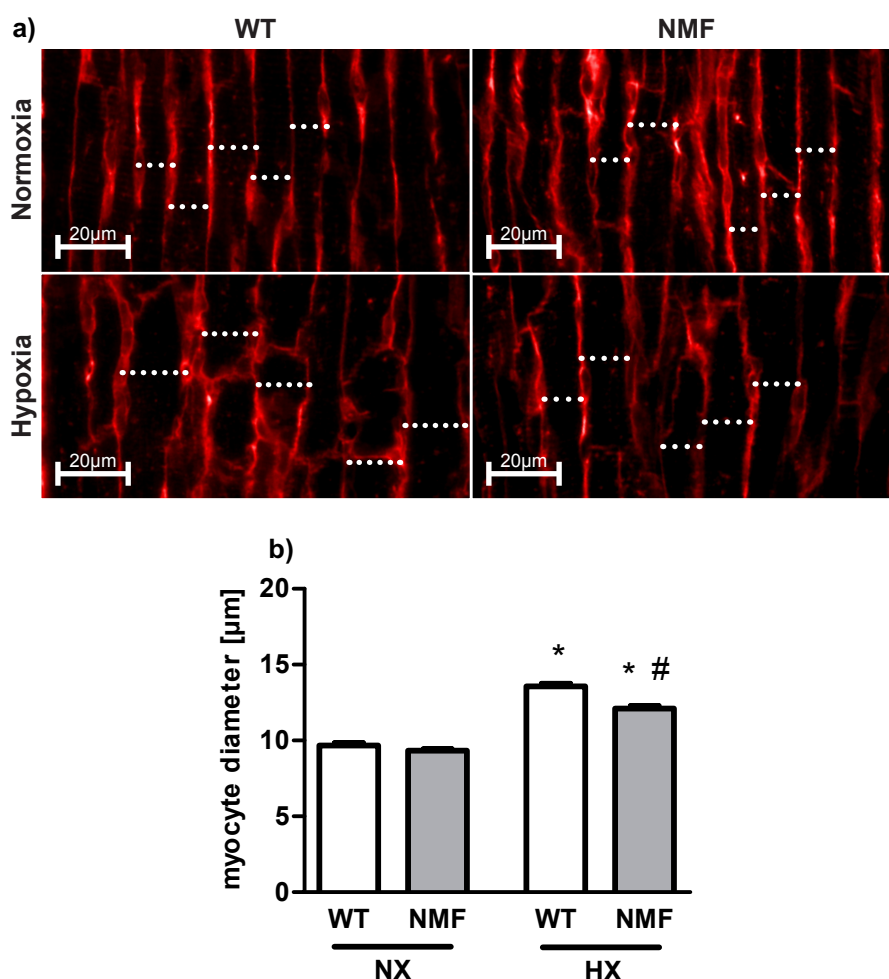


Figure 24 Hypoxic increase in cardiomyocyte diameter is reduced in NMF333 mice

a) Representative microscopic high power fields (HPFs) at 40-fold magnification of longitudinal sections from the right ventricle of wildtype (WT) and NMF333 (NMF) mice exposed to chronic hypoxia (HX, 10% oxygen) for three weeks or normoxic conditions (NX). Sections were stained with rhodamine labelled wheat-germ agglutinin to mark cellular boundaries. b) Quantification of individual cardiomyocyte diameter. Values are presented as mean \pm SEM; $n=120$; * $p<0.05$ HX vs. NX; # $p<0.05$ NMF vs. WT; scale bar = $20 \mu\text{m}$ [215].

4.3.5.4. Hypertrophy-linked gene expression of the right ventricle

To further assess right ventricular hypertrophy in response to chronic hypoxia, the expression of the hypertrophy markers was determined by quantitative PCR in RV tissue obtained from WT and NMF333 mice after exposure to three weeks of chronic hypoxia or normoxia. Besides the ACTA1 gene, coding for α -skeletal muscle actin (α SKA), β -myosin heavy chain (β -MHC) was selected as marker gene, since their expression was described to correlate with cardiac hypertrophy [27, 112].

Under normoxic conditions no difference of statistical significance was found in the β -MHC levels between WT and NMF333 mice. The exposure to chronic hypoxia led to an upregulation of the β -MHC mRNA levels by 4.3-fold in WT mice compared to normoxic WT mice, and by 2.4-fold in nmf333 mice compared to normoxic WT mice, although the latter was not statistically significant (Fig. 25a) [215]. Similarly, the ACTA1 mRNA levels were found to be upregulated by 3.9-fold in hypoxic WT mice. However, a significantly higher ACTA1 gene expression by 7.9-fold was already found in normoxic NMF333 mice, which persisted under hypoxia (Fig. 25b).

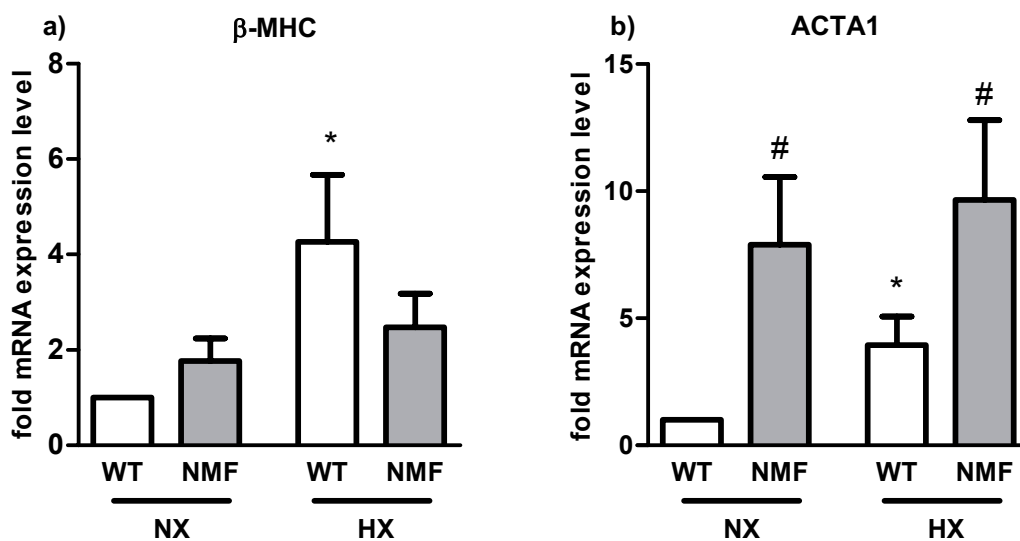


Figure 25 Hypertrophy associated gene expression in right ventricles of wildtype and NMF333 mice
 Quantitative PCR was performed for a) β -myosin heavy chain (β -MHC) gene and b) ACTA1, encoding α -skeletal muscle actin from cDNA derived from RV tissue of wildtype (WT) and NMF333 (NMF) mice exposed to chronic hypoxia (HX, 10% oxygen) for three weeks or to normoxic conditions (NX). Relative mRNA levels were calculated using β -actin as reference gene and NX/WT mice as reference condition. Values are presented as mean \pm SEM; $n=3$; * $p<0.05$ HX vs. NX; # $p<0.05$ NMF vs. WT [215].

4.3.6. Pulmonary vascular responses to chronic hypoxia

4.3.6.1. Pulmonary vascular remodeling

To determine the extent of pulmonary vascular remodelling, a hallmark of pulmonary hypertension, lung tissues of wildtype and NMF333 mice exposed to chronic hypoxia of 10% oxygen for three weeks or normoxia were stained with an antibody against α -smooth muscle actin to evaluate neo-muscularization of small pulmonary arteries (Fig. 26a) [215]. The vessels were quantified and grouped according to their diameter.

Under normoxic conditions, the number of α -smooth muscle actin positive vessels with a diameter up to 30 μm did not differ between the mouse lines: the average count in wildtype mice was 12 vessels in four HPF's and 14 in NMF333 mice. After exposure to chronic hypoxia, the average number of positive vessels increased significantly up to 39 in wildtype, but only up to 29 in NMF333 mice, being a relative reduction of neomuscularisation by 44% in hypoxic NMF333 mice (Fig. 27b) [215].

The number of vessels with a diameter ranging between 30 μm to 60 μm and greater than 60 μm were not influenced by chronic hypoxia. The mean number of vessels ranging between 30 μm up to 60 μm was about 7 under normoxia in both mouse lines, which remained after exposure to chronic hypoxia (Fig. 27c), whereas the average count for vessels greater than 60 μm remained between 1 and 2 for both mouse lines under normoxic and hypoxic conditions (Fig. 27d).

These results suggest, that hypoxia induced vascular remodelling mainly took place in smaller vessels up to 30 μm . Furthermore, p22phox-deficient NMF333 mice were less affected by hypoxia-induced pulmonary vascular remodelling compared to WT mice

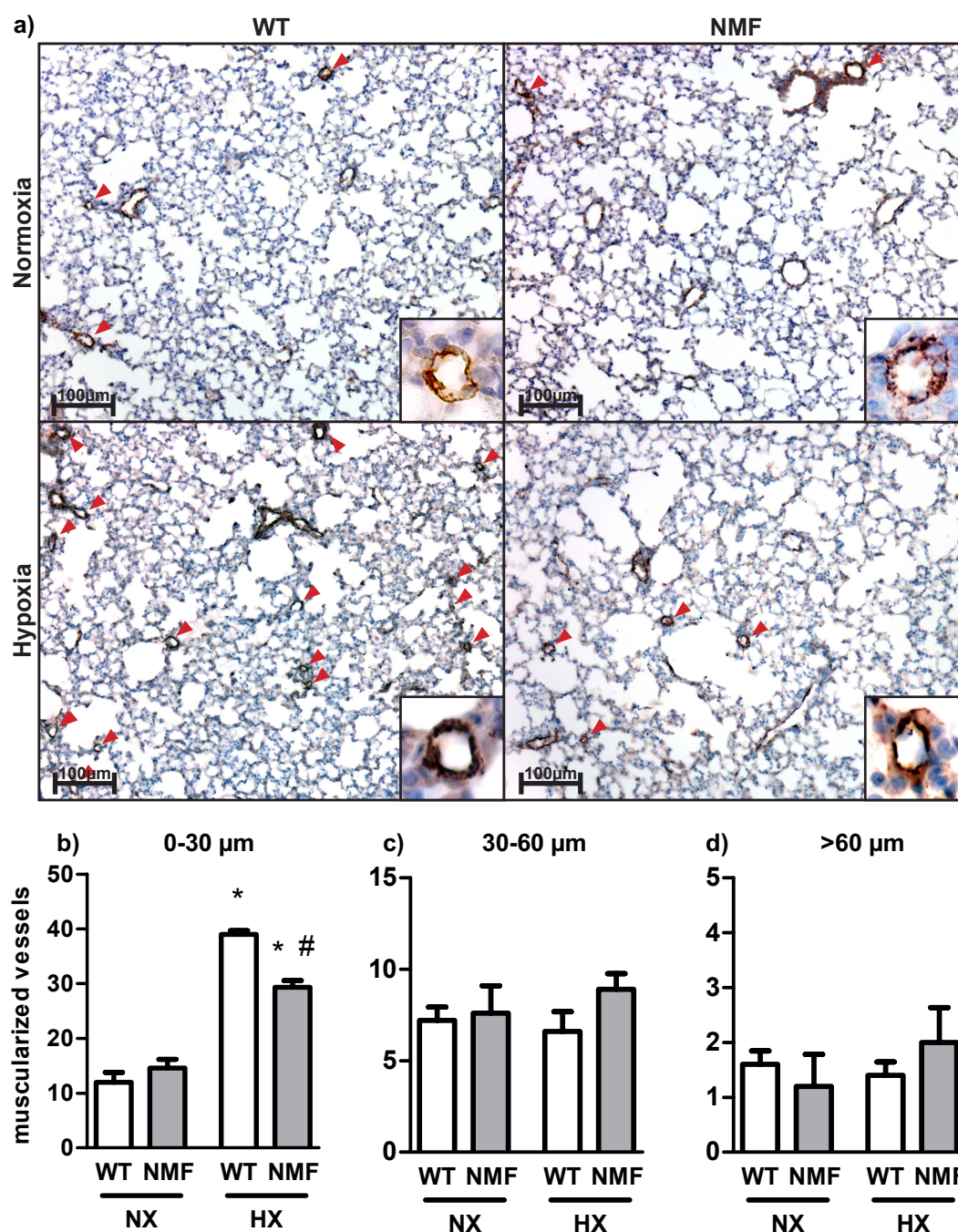


Figure 26 Hypoxia- induced pulmonary vascular remodelling is diminished in NMF333 mice.

a) Representative microscopic high power fields (HPFs) at 10-fold magnification of lung tissue obtained from wildtype (WT) and NMF333 (NMF) mice exposed to chronic hypoxia (HX, 10% oxygen) for three weeks or normoxic conditions (NX) were stained with an antibody against α -smooth-muscle actin. Red arrows indicate positive vessels. Boxes show representative small muscularised vessels at 40-fold magnification.

For quantification of vessel neomuscularisation, the number of α -smooth muscle actin positive vessels was counted in four HPFs per lung and grouped according to their diameter: b) 0-30 μm , c) 30-60 μm and d) $\geq 60 \mu\text{m}$. Values are presented as mean \pm SEM; n=5; * $p < 0.05$ HX vs. NX; # $p < 0.05$ NMF vs. WT; scalebar = 100 μm [215].

4.3.6.2. Pulmonary vascular proliferation

Next the hypothesis was investigated that the reduction in pulmonary vascular remodelling observed in hypoxic NMF333 mice might be linked to a reduced proliferative activity of vascular smooth muscle cells.

Therefore, lung tissue sections were stained with an antibody against the proliferative marker Ki67 in combination with an antibody against α -smooth muscle actin to mark smooth muscle cells (Fig 28a) [215]. For quantification, the number of all vessels, independent of size, that appeared double positive for α -smooth muscle actin (remodelled) and Ki67 (active proliferation) were related to the total number of fully α -smooth muscle actin positive vessels (Fig. 28b) [215]. In hypoxic WT mice, 51% of the pulmonary vessels were positive for Ki67, while in hypoxic NMF333 mice, only 22% of the pulmonary vessels were positive for Ki67, thus representing a significant reduction in Ki67-positive vessels by around 57%.

These findings suggest that the reduction in pulmonary vascular remodelling in hypoxic NMF333 mice was at least in part related to a reduction in proliferative activity of pulmonary vascular smooth muscle cells.

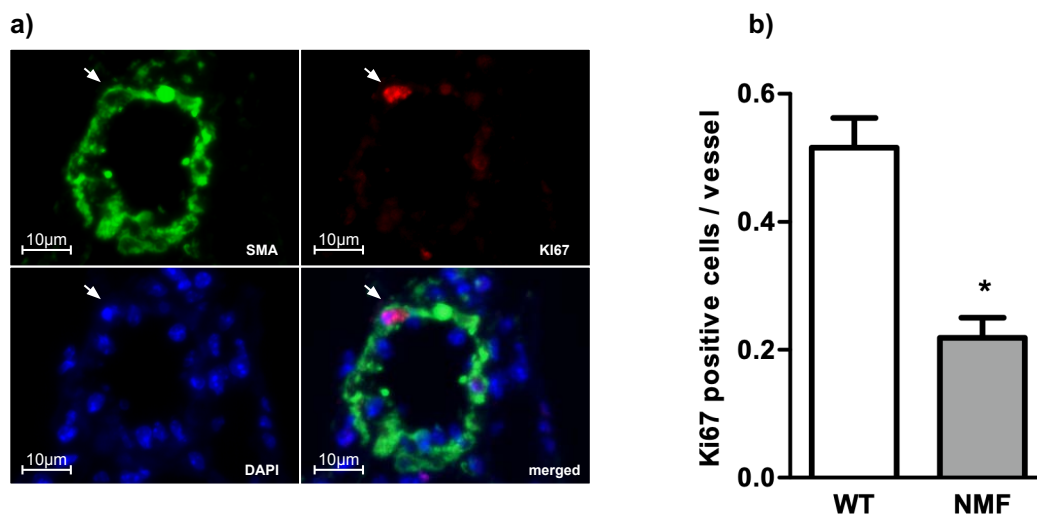


Figure 27 Ki67 staining is reduced in small muscularized vessels in hypoxic NMF333 mice
Lung tissue sections from wildtype (WT) and NMF333(NMF) mice exposed to chronic hypoxia (HX, 10% oxygen) for three weeks were co-stained with antibodies against α -smooth muscle actin (SMA)[green] and the proliferation marker Ki67 (Ki67) [red], the nuclei were stained with DAPI [blue]. a) Representative high power field of 20-fold magnification of an α -SMA and Ki67 positive vessel from a WT mouse. Ki67 positive cells appear violet in the superposition image. b) Proliferation index was calculated as ratio between number of SMA and Ki67 positive vessels compared to total number of SMA positive vessels. Values are presented as mean \pm SEM; n=3; * $p < 0.05$ NMF vs. WT; scale bar = 10 μ m [215].

4.3.7. Pulmonary and cardiac ^{18}F -FDG uptake

Since hypoxia has been shown to promote a metabolic switch from oxidative phosphorylation to glycolysis [165, 217], *in vivo* glucose uptake was determined by ^{18}F -FDG-positron emission tomography (PET). ^{18}F -FDG uptake was assessed by autoradiography in cryo-sections from the right and left ventricle and the lung and related to glucose uptake in the liver (Fig. 28) Under normoxic conditions, the relative ^{18}F -FDG uptake in all three organs did not differ between wildtype and NMF333 mice (lung 2.3 vs 3.0; RV 29 vs 36; LV 52 vs. 62), In hypoxic wildtype mice, a strong and significant increase in relative ^{18}F -FDG uptake was observed in lung up to 4.1, in RV up to 68 as well as in LV up to 115, although the latter one was not tested as statistically significant. Interestingly, the relative ^{18}F -FDG uptake, measured in the lungs of hypoxic NMF333 mice, did not increase in a significant way and remained with 2.2 significantly below the value of hypoxic wildtype

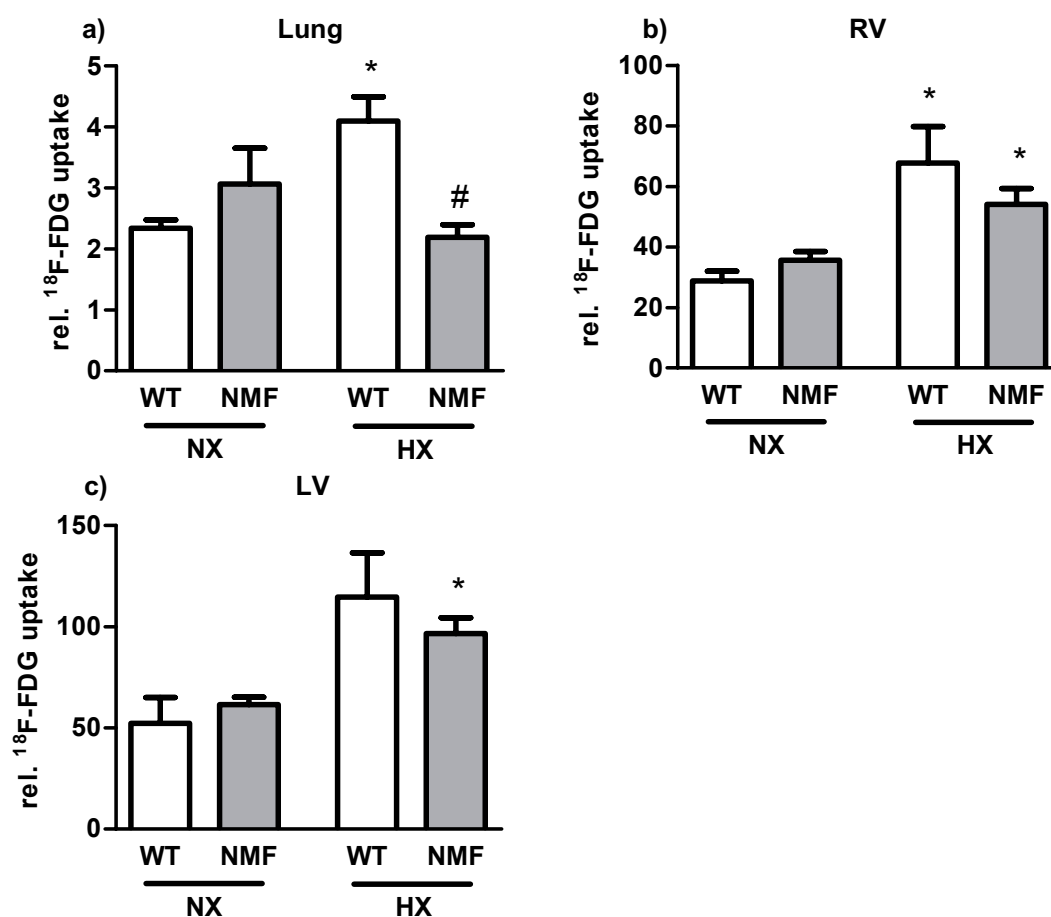


Figure 28 ^{18}F -FDG uptake is reduced in lungs of hypoxic NMF333 mice
 Wildtype (WT) and NMF333 (NMF) mice, exposed to chronic hypoxia (HX, 10% oxygen) for three weeks or to normoxic conditions (NX), were injected with ^{18}F -FDG. Glucose uptake was assessed using autoradiography. The glucose uptake in a) lung b) right ventricle (RV) and c) left ventricle (LV) was calculated and normalized to liver glucose uptake. Values are presented as mean \pm SEM; n=3; * $p < 0.05$ Hx vs. NX; # $p < 0.05$ NMF vs. WT.

mice. ^{18}F -FDG uptake of the remaining organs was found to be increased up to 54 in the right ventricle and up to 97 in left ventricle in hypoxic NMF333 mice. These values lie beneath the relative metabolic activity of hypoxic wildtype mice's RV and LV, however, the difference was not tested as statistically significant.

4.4. Regulation of HIF1 α

The hypoxia-inducible factors are key regulators of the response to hypoxia [165]. HIFs have also been shown to play an important role in the development of hypoxia induced pulmonary hypertension [213]. We therefore aimed to analyse whether p22phox would contribute to the regulation of HIF1 α under normoxia and hypoxia.

4.4.1. Regulation of HIF1 α gene expression by hypoxia

To assess the HIF1 α mRNA levels in human microvascular endothelial cells (HMEC-1) and mouse embryonic stem cells (mESC) in response to hypoxia quantitative PCR was performed.

In both cell lines HIF1 α mRNA levels tended to be lower under hypoxia than under normoxia, although this decrease did not reach statistical significance with the exception of the HIF1 α mRNA levels at 6h hypoxia in mESC (Fig. 31).

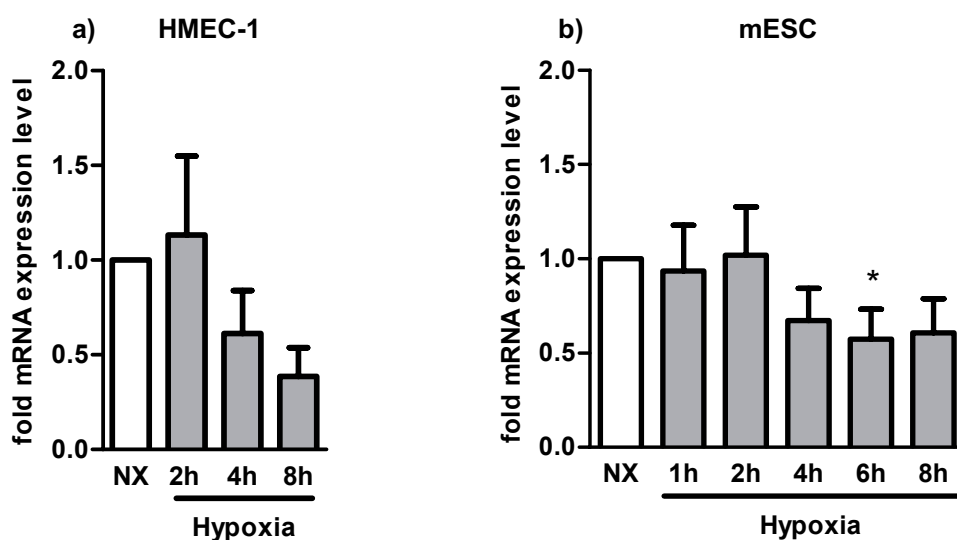


Figure 29 Hypoxia does not affect HIF1 α mRNA levels

Quantitative PCR was performed for HIF1 α from cDNA derived from a) human microvascular endothelial cells (HMEC-1) and b) mouse embryonic stem cells (mESC) exposed to normoxia (NX) or hypoxia (1% oxygen) for the given periods of time. Relative mRNA levels were calculated using β -actin as reference gene and NX as reference condition. Values are presented as mean \pm SEM; n=3; * p<0.05 compared to NX.

4.4.2. Regulation of HIF1 α protein levels by hypoxia

The HIF1 α protein levels were assessed in human microvascular endothelial cells (HMEC-1) (Fig. 30a & c) [215] and mouse embryonic stem cells (mESC) in response to increasing times of hypoxia using Western blot analysis. In both cell lines, HIF1 α protein levels increased already upon 0.5 to 1 h of hypoxia and remained elevated over the 8 h observation period (Fig. 30b & d).

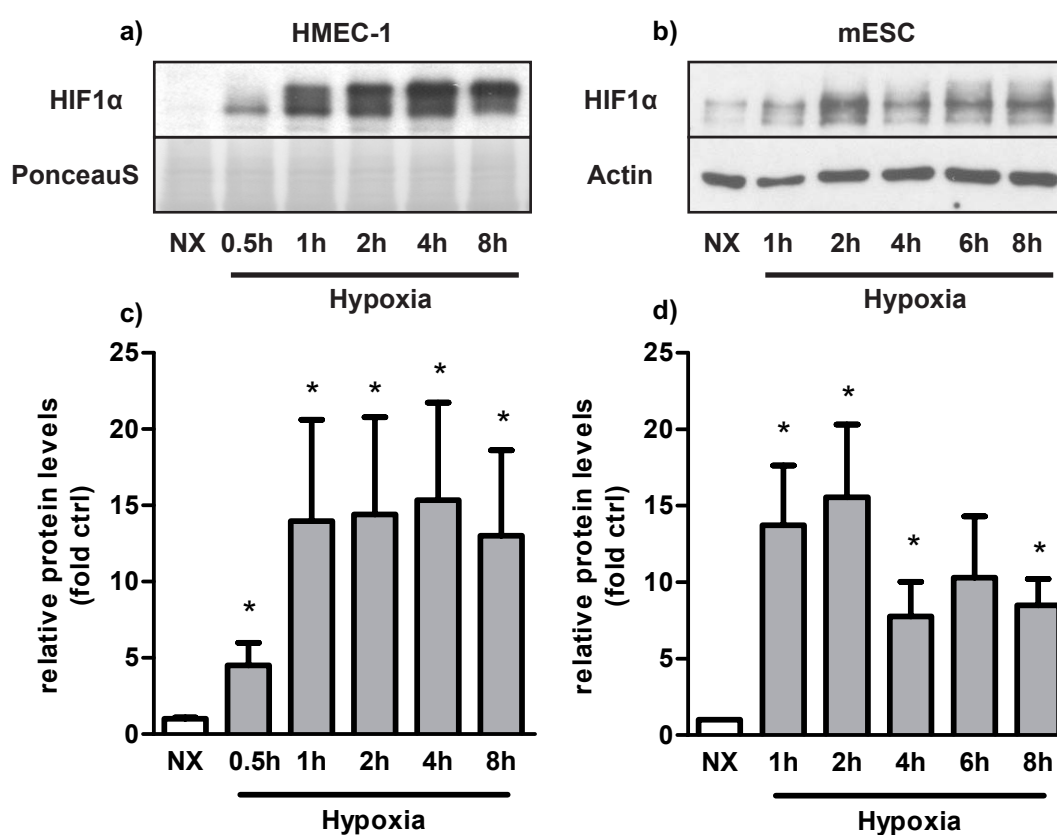


Figure 30 HIF1 α protein levels are induced by hypoxia

Western blot analysis was performed for HIF1 α in a) human microvascular endothelial cells (HMEC-1) and b) mouse embryonic stem cells (mESC) exposed to normoxia (NX) or hypoxia (1% oxygen) for the indicated periods of time. PonceauS or β -actin served as loading control. Quantification of Western blot analysis is shown in graphs c) for HMEC-1 and d) for mESC. Values are presented as mean \pm SEM; $n=3$; * $p<0.05$ compared to NX [215].

4.4.3. HIF1 α gene expression in hypoxic mice

HIF1 α gene expression was also determined in lung (Fig. 31a) and right ventricular tissue (Fig. 31b) of wildtype and NMF333 mice by quantitative PCR. Thereby, HIF1 α mRNA levels showed no significant alterations, neither by genotype nor by oxygen concentration, matching the observations from cell culture (4.4.2.).

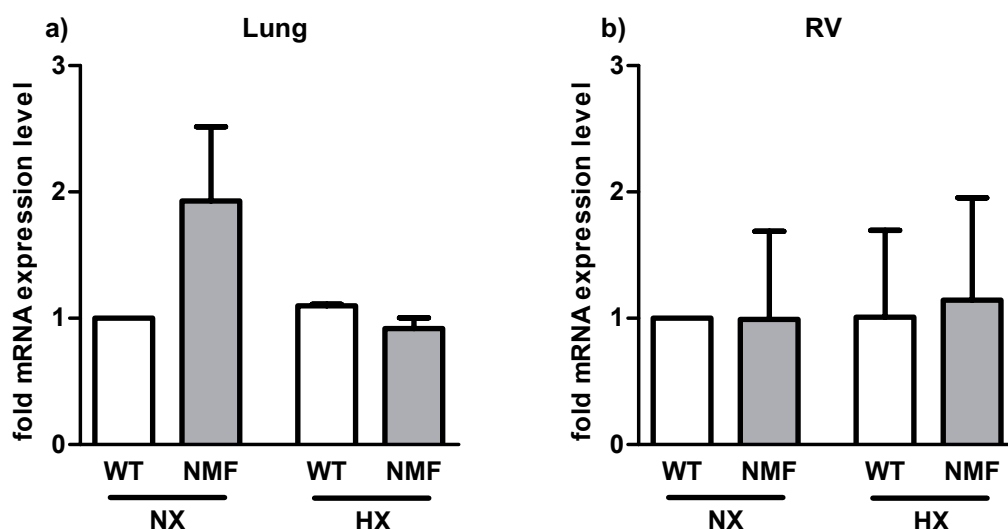


Figure 31 HIF1 α mRNA expression is not influenced by chronic hypoxia or the Y121H mutation in the lung and right ventricle

Quantitative PCR was performed for HIF1 α from cDNA derived from a) lung and b) right ventricular tissue (RV) obtained from wildtype (WT) and NMF333 (NMF) mice, exposed to chronic hypoxia (10% oxygen) for three weeks or to normoxic conditions. Relative mRNA expression was calculated using β -actin as reference gene and NX/ WT as reference condition. Values are presented as mean \pm SEM; n=3; * $p < 0.05$ compared to reference condition.

4.4.4. HIF1 α protein levels in hypoxic mice

Next, Western blot analysis was performed for HIF1 α in lung (Fig 32a) and right ventricular tissue (Fig 32b) from wildtype and NMF333 mice held under normoxic and hypoxic conditions for three weeks [215].

Quantification revealed equal HIF1 α protein levels under normoxic conditions in lung (Fig. 32c) and RV tissue (Fig. 32d) of wildtype and NMF333 mice. Exposure to chronic hypoxia led to a significant induction of HIF1 α protein levels by 4.8-fold in lung and by around 8.0-fold in RV tissue of wildtype mice. However, in NMF333 mice, HIF1 α protein levels increased only by 2.0-fold in lung and by 2.4-fold in RV tissue in response to chronic hypoxia which was significantly lower than the values measured in hypoxic wildtype mice, suggesting an impaired hypoxic induction of HIF1 α protein in NMF333 mice [215].

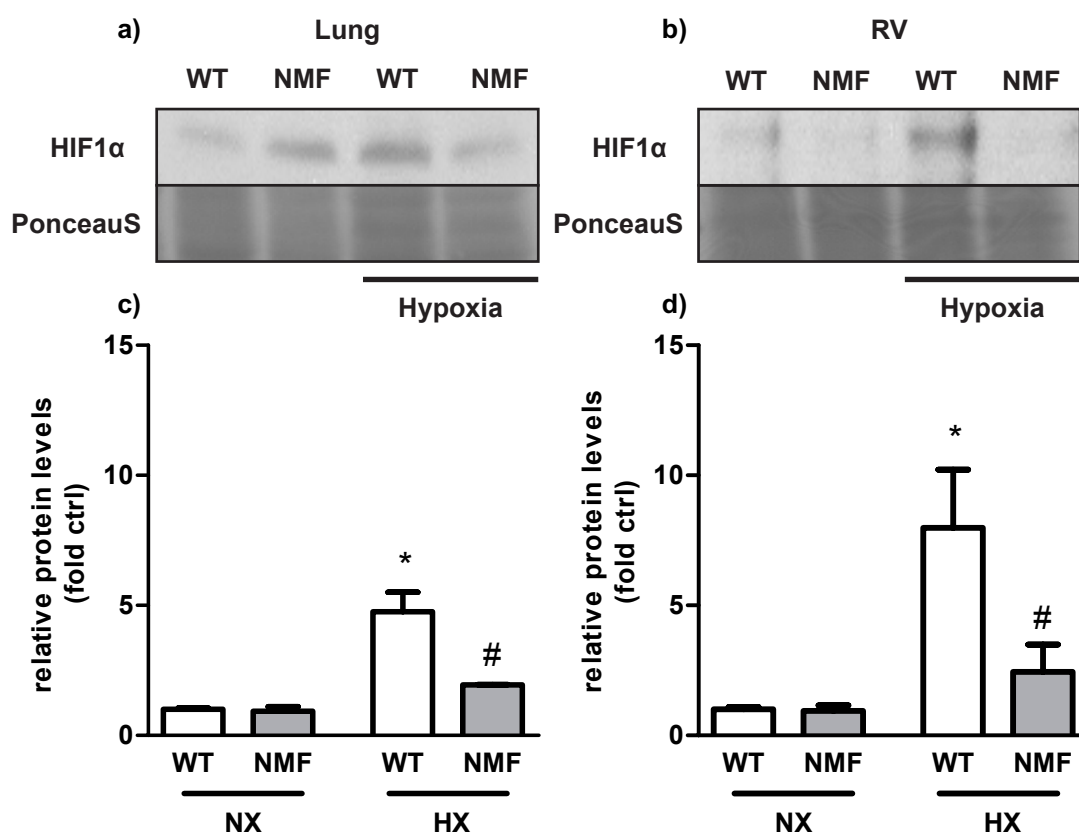


Figure 32 Hypoxic upregulation of HIF1 α is diminished in NMF333 mice
 Western blot analysis for HIF1 α was performed in a) lung and b) right ventricular (RV) tissue obtained from wildtype (WT) and NMF333 (NMF) mice exposed to chronic hypoxia (HX, 10% oxygen) for three weeks or to normoxic conditions (NX). β -actin served as loading control. Quantification of Western blot analysis is shown in graphs c) for lung and d) for RV. Values are presented as mean \pm SEM; $n=3$; * $p<0.05$ HX vs. NX; # $p<0.05$ NMF vs. WT [215].

4.4.5. Effect of p22phox silencing on HIF1 target gene expression

To further analyse the role of p22phox in regulating HIF1 signalling pathways, human microvascular endothelial cells were either transfected with p22phox siRNA (si p22), to block p22phox expression, or with non-interfering control siRNA (si ctrl). The transfected cells were exposed to 1% oxygen for eight hours. Quantitative PCR was used to check for alterations in gene expression with focus on HIF1 target genes.

P22phox mRNA levels were completely downregulated by p22phox siRNA transfection under normoxic and hypoxic condition (Fig. 33a)

However, HIF1 α mRNA levels were not affected by p22phox knockdown (Fig. 33b). Levels of the HIF1 target gene PGK1 mRNA were not affected in HMEC-1 transfected with p22phox siRNA under normoxia, while VEGF mRNA levels were increased in these cells (Fig. 33c, d). Exposure to hypoxia increased mRNA levels of PGK1 and VEGF (Fig 33c, d)

in cells transfected with control siRNA: PGK1 by 2.9-fold and VEGF1 by 9.7-fold compared to normoxic control cells. In p22phox-deficient cells, VEGF mRNA levels increased by only 6.5-fold under hypoxia, thus being a relative reduction by one third compared to normoxic control cells, whereas PGK1 mRNA levels did not show any regulation under hypoxia (Fig. 33c, d) [215].

These results suggest an impaired HIF1 target gene induction in response to chronic hypoxia due to p22phox deficiency.

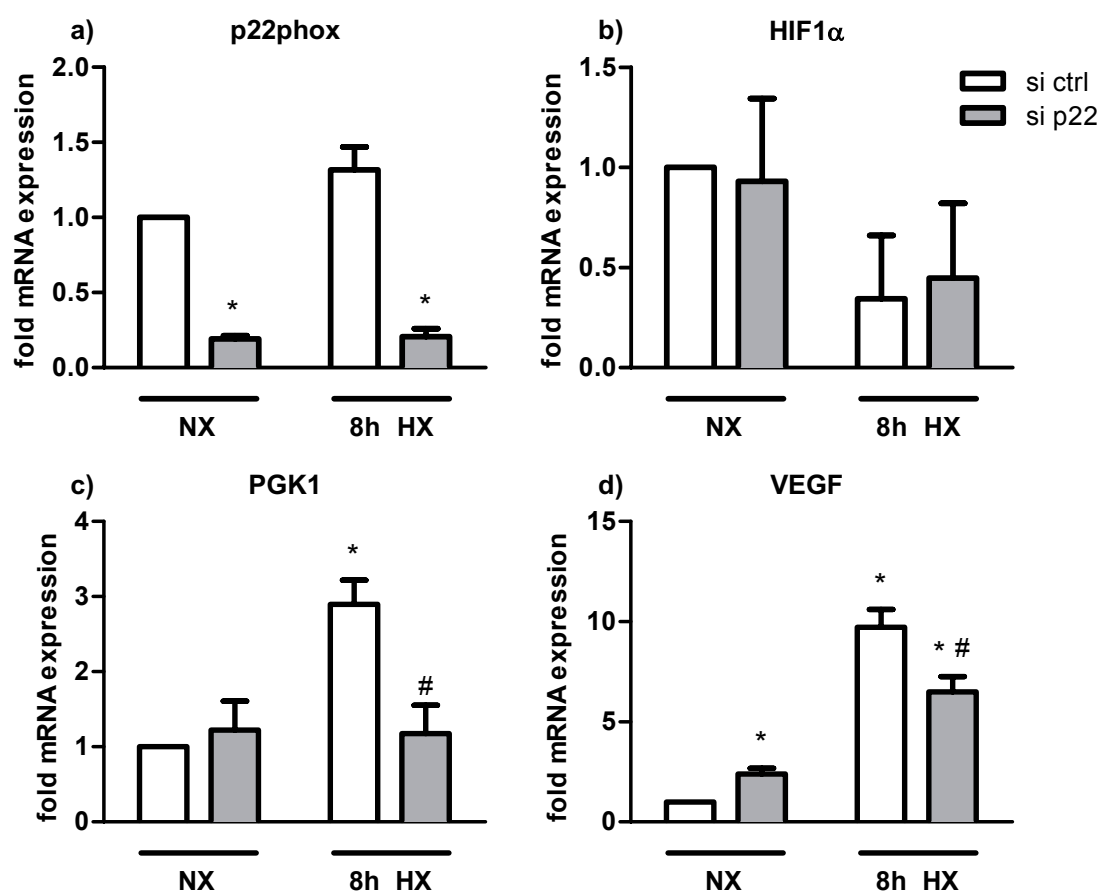


Figure 33 Depletion of p22phox decreases hypoxic induction of HIF1 target genes in hypoxic HMEC-1
 Quantitative PCR was performed for a) p22phox, b) HIF1α and HIF1 target genes c) PGK1 and d) VEGF from cDNA derived from HMEC-1, transfected with p22phox siRNA (si p22) or non-interfering control siRNA (si ctrl) and exposed to 8h of hypoxia (HX, 1% oxygen) or normoxia (NX). Relative mRNA levels were calculated using β-actin as reference gene and NX/ si ctrl as reference condition. Values are presented as mean ± SEM; n=3; * p<0.05 compared to reference condition; # p<0.05 si p22 vs. si ctrl [215].

4.5. NOX1-K.O. mice and chronic hypoxia

Previous data in the laboratory had shown that NOX1 protein levels are also increased in lung tissues in mice with hypoxia-induced pulmonary hypertension [215]. It was thus tested, whether NOX1 would also play a pathogenetic role in hypoxia-induced pulmonary hypertension.

4.5.1. Haemodynamic measurements

NOX1-K.O. mice were exposed to chronic hypoxia (10% oxygen) for three weeks as above, and haemodynamic measurements of the right heart were performed. Under normoxic conditions, the pressure values did not differ between WT and NOX1-K.O. mice (Fig. 34).

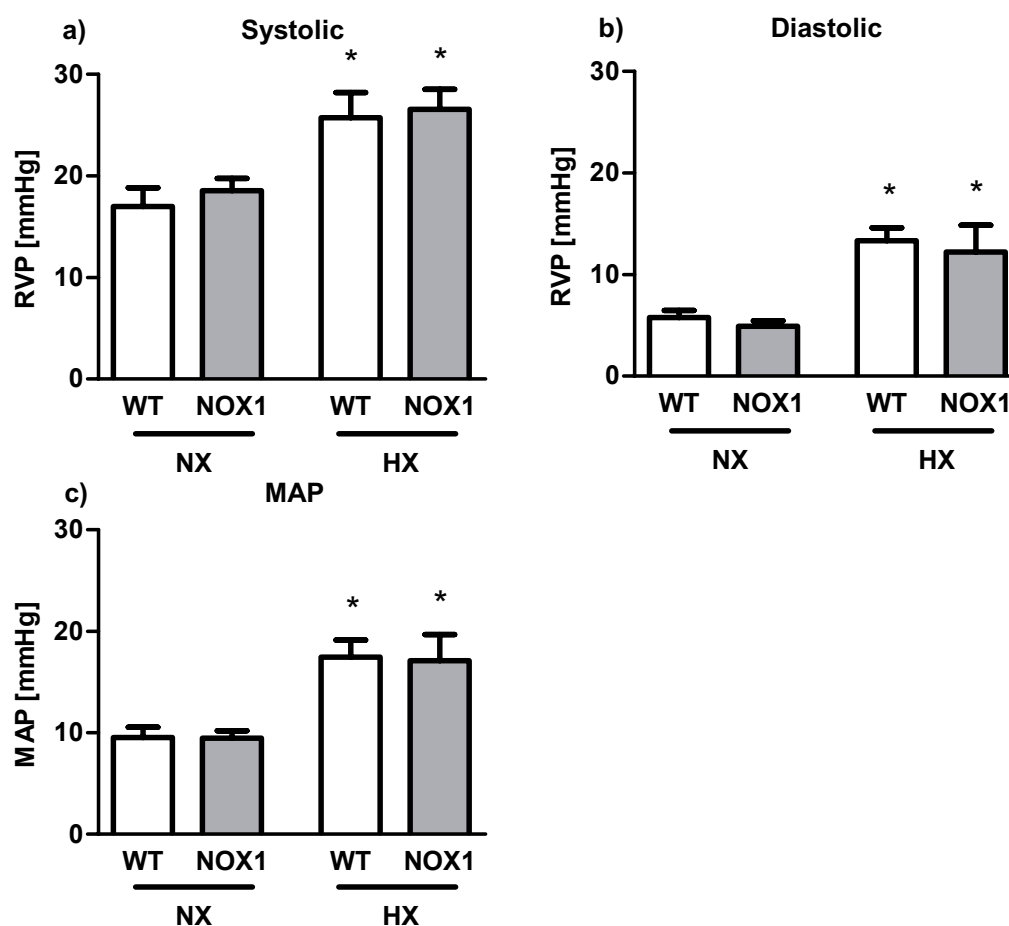


Figure 34 NOX1-K.O. mice are not protected against hypoxia-induced pulmonary hypertension
 Haemodynamic pressure values were obtained from wildtype (WT) and NOX1-K.O. (NOX1) mice exposed either to chronic hypoxia (HX, 10% oxygen) for three weeks or to normoxic conditions (NX) using a trans-thoracically introduced tip catheter system. a) systolic right ventricular pressure (RVP), b) diastolic RVP, c) mean arterial pressure (MAP) from RV. Values are presented as mean \pm SEM; $n=3$; * $p<0.05$ HX vs. NX; # $p<0.05$ NOX1 vs. WT.

In contrast to NMF333 mice, however, the increase in systolic, diastolic and mean pulmonary arterial pressure after exposure to chronic hypoxia, was similar in wildtype and NOX1-K.O mice with systolic pressure rising to up to 26 mmHg, diastolic pressure rising up to 13 mmHg, and mean pulmonary arterial pressure increasing up to 17 mmHg.

4.5.2. Cardiac response to chronic hypoxia

Next, the Fulton's index was determined to assess right ventricular hypertrophy as described above (Fig. 36). However, no difference could be observed between hypoxic wildtype and NOX1-K.O. mice.

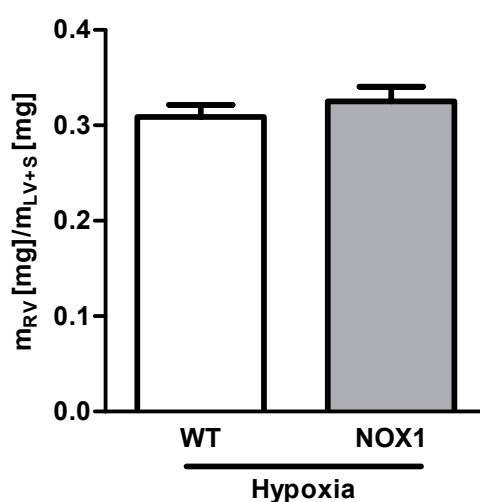


Figure 35 NOX1 K.O. mice develop hypoxia-induced right ventricular hypertrophy

Fulton's index was expressed as ratio between right ventricular mass (m_{RV}) and left ventricular mass including the septum (m_{LV+S}). Fulton's index was determined in wildtype (WT) and NOX1-K.O. (NOX1) mice exposed to chronic hypoxia (10% oxygen) for three weeks. Values are presented as mean \pm SEM; $n=3$.

4.5.3. Pulmonary vascular remodelling

Finally, lung tissue obtained from wildtype and NOX1-K.O. mice exposed to chronic hypoxia was analysed for signs of pulmonary vascular remodelling. As described above, lung tissue was stained with an antibody against α -smooth muscle actin and the number of immune reactive vessels was assessed. In wildtype mice, the number of small muscularised vessels with a diameter up to 30 μm increased as expected in response to chronic hypoxia (Fig. 36a), while neither the number of vessels with a diameter ranging between 30 μm and 60 μm (Fig. 36b), nor with a diameter greater than 60 μm (Fig. 36c) were affected by

hypoxia. The number of small muscularised vessels in NOX1-K.O. mice, however, also increased in a similar amount (Fig. 36a). There was no difference to wildtype mice, neither under hypoxia, nor under normoxia.

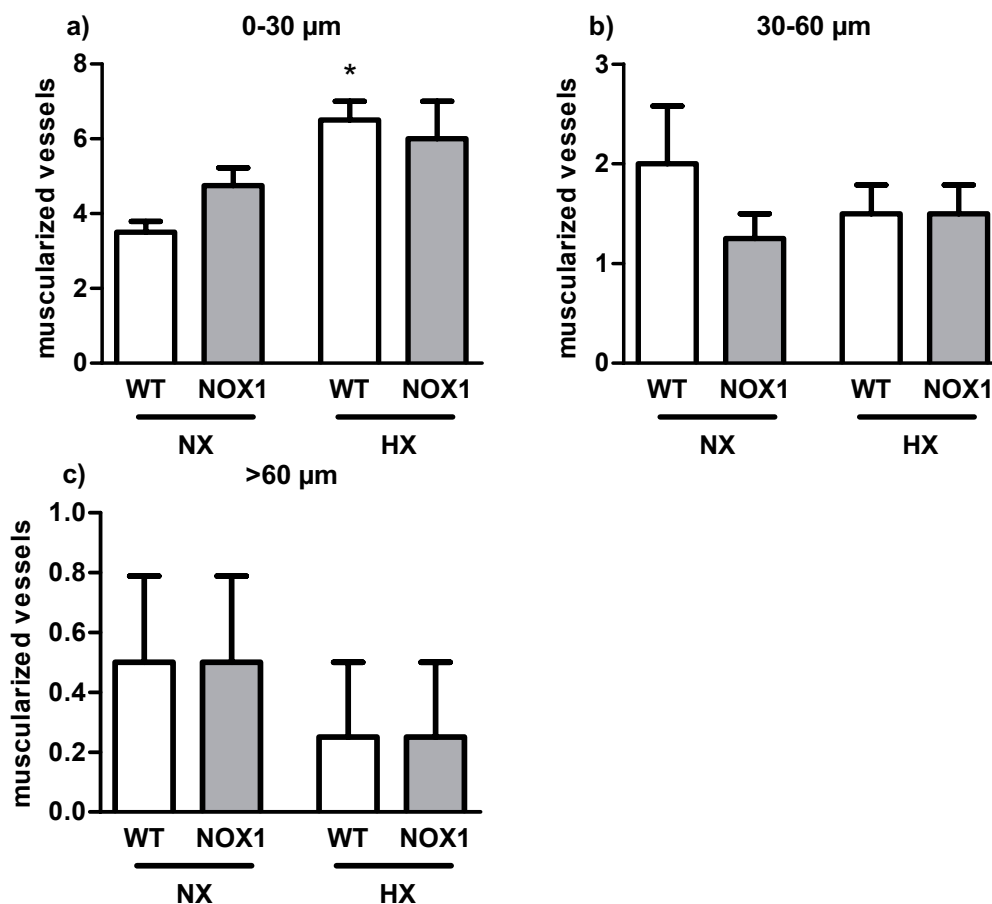


Figure 36 Hypoxia-induced pulmonary vascular remodelling is not affected in NOX1-K.O. mice
 For quantification of pulmonary vessel neomuscularisation lungs obtained from wildtype (WT) and NOX1-K.O. (NOX1) mice, exposed to chronic hypoxia (HX, 10% oxygen) for three weeks or to normoxic conditions (NX), were stained with an antibody against α -smooth-muscle actin. The number of α -smooth muscle actin positive vessels was counted in four high power fields (HPF) per lung, expressed as number of positive vessels per HPF. They were grouped according to their diameter: a) 0-30 μm , b) 30-60 μm and c) $\geq 60 \mu\text{m}$. Values are presented as mean \pm SEM; n=2; * $p < 0.05$ HX vs. NX; # $p < 0.05$ NOX1 vs. WT.

These results suggest, that NOX1-K.O. mice were equally affected by chronic hypoxia as WT mice, developing pulmonary vascular remodelling with elevated right ventricular pressure values and right ventricular hypertrophy. Thus, no protective effect regarding the development of hypoxia induced PH could be observed.

5. Discussion

The aim of this study was to analyse the role of p22phox in the development of hypoxia-induced pulmonary arterial hypertension. To this end, NMF333 mice harbouring the Y121H point mutation in the coding region of the Cyba gene, leading to a loss of p22phox protein, were exposed to chronic hypoxia.

In our study we could show that:

- a) P22phox protein levels were upregulated under hypoxic conditions.
- b) The Y121H mutation in the Cyba gene resulted in loss of p22phox protein in various tissues.
- c) Loss of p22phox reduced hypoxia-induced HIF1 α levels.
- d) NMF333 mice showed reduced leukocyte ROS production and a loss of vessel forming capacity.
- e) NMF333 mice were partially protected against hypoxia-induced PAH, RV hypertrophy and pulmonary vascular remodelling.
- f) NMF333 showed reduced metabolic and proliferative activity in hypoxic lungs.
- g) NOX1-K.O. mice were not protected against the development of hypoxic PAH.

5.1. Regulation of p22phox

5.1.1. Hypoxic regulation of p22phox

In the present study it was shown that hypoxia upregulated p22phox protein levels in human microvascular endothelial cells (HMEC-1), mouse embryonic stem cells (mESC), as well as in lung and heart tissue of WT mice exposed to chronic hypoxia.

A hypoxia-induced upregulation of the cytochrome b558 complex, formed by the NOX2 and p22phox proteins, has already been described in early studies in HepG cells [71]. Increased NOX2 protein levels have also been observed in hypoxic cardiomyocytes [214]. Furthermore, an upregulation of NOX isoforms, especially NOX1, NOX4 and NOX5 as well as DUOX1 and 2 and their regulatory units was observed in several tumour types, playing an important role in tumour's adaption to hypoxia, growth and survival [100, 138, 170, 184].

Thereby, the activation of HIF plays an important role, since it was shown, that NOX2 and NOX4 are targets of HIF1 [47, 48].

Interestingly the mRNA expression of p22phox was not affected by hypoxia neither in HMEC-1 nor in murine lungs and hearts, whereas mouse embryonic stem cells showed a downregulation of p22phox gene expression. A trend to downregulation of p22phox mRNA has been described before, however not in cells but in murine lung tissue, which showed at first unchanged p22phox mRNA levels after three days of hypoxia but reduced levels after three weeks of hypoxia [140] – an observation that we could not confirm in our study.

In contrast, an increase in p22phox mRNA levels has been reported by stimuli like intermittent hypoxia, urotensin-II or ROS [49, 128, 151]. Thus, these findings suggest that under hypoxic conditions, p22phox is not regulated at the transcriptional level. The difference observed between the cell lines might be explained by a more sensitive reaction of the undifferentiated stem cells compared to differentiated cells. In line, recent data from our group point to a posttranslational mechanism of p22phox regulation under hypoxia, whereby decreased ubiquitinylation and proteasomal degradation of p22phox dependent on prolyl hydroxylases (PHDs) and the E3 ubiquitin ligase protein von Hippel Lindau (pVHL), resulted in p22phox stabilization and accumulation under hypoxia [215]. Interestingly, this mechanism resembles the hypoxic regulation of the transcription factor HIF1 α , the master regulator of the cellular response to hypoxia [102], suggesting that p22phox is an important element of hypoxia signalling cascades.

5.1.2. Y121H mutation and p22phox expression

To study the effects of p22phox *in vivo*, we used the NMF333 mouse strain, harbouring a Y121H point mutation in the coding region of the *Cyba* gene. The mutation is located in the second predicted transmembrane domain of the p22phox protein and has been described to lead to a loss of p22phox protein in phagocytes [144]. The present study confirmed not only the loss of p22phox protein in peripheral blood mononuclear cells (PBMCs) but also the failure to produce ROS in an adequate way. Furthermore, a loss of p22phox protein could also be observed in the spleen while in liver, lung and heart p22phox protein was neither detectable in WT nor in mutant mice. Interestingly, p22phox was present in kidney of both mouse lines.

As integral part of the NADPH oxidase complex, p22phox is expressed together with a NOX1-4 homolog, forming functional heterodimers [22]. P22phox is expressed

ubiquitously, though the expression rate varies between different tissues [63]. Immune cells like PBMCs naturally express high levels of p22phox and NOX2, their predominant isoform, since it is essential for their function in immune defence. Therefore, it can already be detected in an unstimulated state, just like in splenic tissue.

In lung, liver and cardiac tissue, p22phox expression has been reported to be rather low [90, 190], and it was undetectable in our study under normoxic conditions. In renal tissue, however, p22phox was detected. This might be connected to the strong expression of NOX4 in the kidney, where it was first discovered leading to the name “Renox” in the beginning [8].

The absence of p22phox, caused by the Y121H mutation in PBMCs and splenic tissue of NMF333 mice, has been described to lead to a CGD like phenotype, since p22phox is required for the function of NOX2 [162]. Moreover, NOX3 has been described to be affected by the p22phoxY121H mutation thus causing vestibular problems in NMF333 mice [144]. Furthermore, a reduced superoxide production was observed in CHO-K1 cells expressing NOX1 and Y121H-mutated p22phox [200]. In contrast, NOX4 was found to be expressed normally and remained to interact with p22phoxY121H [200]. These findings match our observation that, in NMF333 mice, p22phox protein is primarily found in kidneys. It suggests that NOX4 might still be capable of interacting with p22phox regardless of its point mutation, thus allowing stabilization of p22phox protein. These findings suggest that the Y121H point mutation in NMF333 mice does not create a complete loss of p22phox protein in all tissues. Taking into consideration that p22phox is only expressed with a correct interacting NOX homolog and vice versa, it rather depends on whether this interaction is influenced by the point mutation [6]. The interaction between NOX1-3 seems to be inflicted in such way, that p22phox is finally not expressed anymore or at least diminished. Recently published results from our group underline these findings, showing a reduced protein half-life time of overexpressed p22phoxY121H in HMEC-1 [215].

5.2. P22phox and HIF

The hypoxia-inducible transcription factors are key players in the adaption to hypoxia, since they promote angiogenesis, proliferation, migration and many other adaptive processes [164, 165]. The alpha-subunits of the heterodimers have been shown to be closely regulated by hypoxia [13].

In this study it was shown that hypoxia upregulates HIF1 α protein in HMEC-1 and mESC while HIF1 α mRNA levels were not affected or even decreased. Furthermore, we could show, that the hypoxia-induced protein accumulation of HIF1 α in murine lung and heart tissue was reduced in the absence of p22phox in NMF333 mice. Moreover p22phox-depleted HMEC-1 failed to upregulate the HIF1 α target genes VEGF and PGK-1 under hypoxic conditions [215]. These findings suggest a clear involvement of NADPH oxidases in the regulatory pathway of HIF1 α . Activation of HIF1 has been shown to lead to an induction of NOX2 and NOX4 under normoxic or hypoxic conditions [47, 48], respectively indicating that HIF1 can regulate ROS production. However, the data presented in this study suggest, that p22phox-dependent NADPH oxidases play also a role in the induction of HIF1 α under hypoxia. In line, previous studies have shown that p22phox-dependent NADPH oxidases increase HIF1 α levels under normoxic conditions. These data suggest that a feedback loop exists between HIF1, NADPH oxidases and generation of ROS.

In this context, different and partially controversial models of the role of ROS on HIF1 α levels under normoxia or hypoxia have been described. On the one hand, an induction and stabilization of HIF1 α by ROS was observed [29]. On the other hand, HIF1 α levels were found to be reduced by reactive oxygen species in endothelial cells in context of chronic hypoxia [101]. In an attempt to integrate these controversial findings, one study designed a complex model including different tissue and cell types, duration of hypoxia and different hypoxic conditions like cancer or ischemia [155]. However, ROS have been described to inhibit prolyl hydroxylases (PHD) or to increase posttranslational modifications and the activation of the ERK and PI3K/AKT pathway via microRNA (miRNA) or other signalling molecules [141]. Recently published data from our group support these pathways [215]. Mechanistically, ROS have been suggested to interfere with the availability of intracellular Fe(II) and ascorbate [46, 113] which are essential cofactors for prolyl hydroxylase activity [107]. Therefore, reduced activity of PHDs would limit the binding of the von Hippel-Lindau protein (pVHL) and the ubiquitin-ligase complex, thus promoting stabilization of HIF1 α . In this context overexpression of p22phox reduced the levels of ascorbate and Fe(II) whereas Fe(III) levels increased in a proportional way, indicating that p22phox-dependent ROS production limits Fe(II) and ascorbate availability [215] (Fig. 37).

Nevertheless, it seems surprising, that the loss of p22phox with a consecutively reduced ROS production has such a strong impact on HIF1 α induction, which is known to be the key regulator in adaption to hypoxia. It is conceivable, that the interactions between HIF1 α and NOXes are much more complex and not fully understood so far.

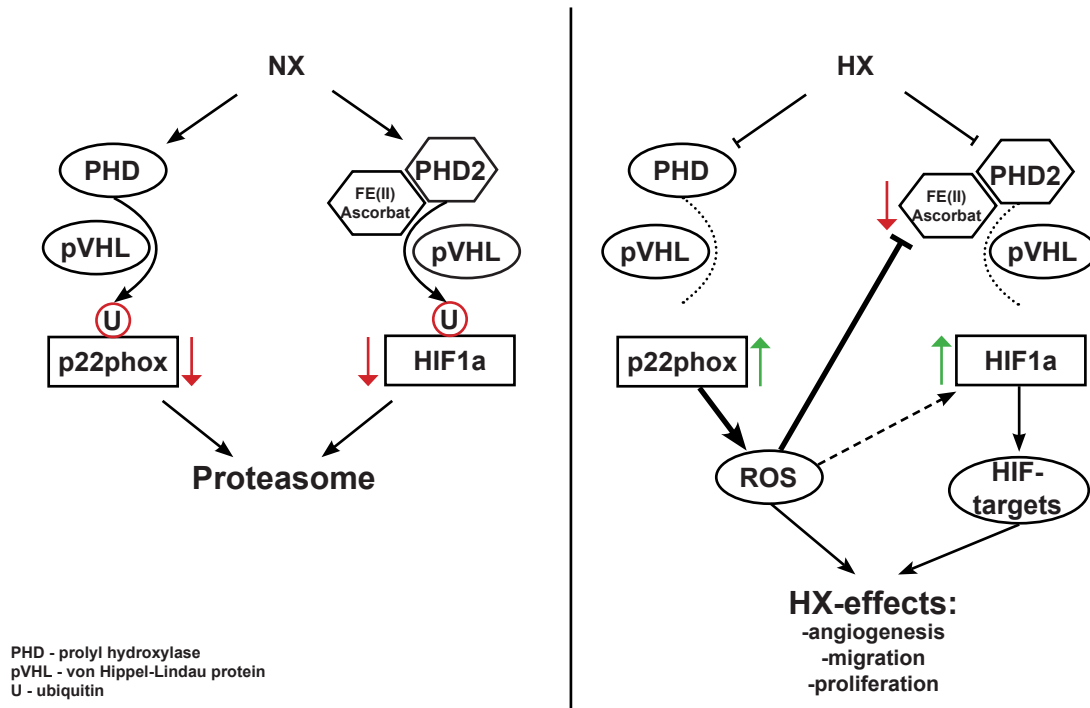


Figure 37 Illustration of the suggested pathway

The scheme illustrates the ROS dependent modulation of the HIF1 α regulatory pathway. Under normoxic conditions (NX) oxygen dependent prolyl hydroxylases (PHD) and the von Hippel-Lindau protein (pVHL), subunit of the ubiquitin ligase complex lead to proteasomal degradation of p22phox and HIF1 α . Hypoxia (HX) impairs the PHD activity leading to p22phox and HIF1 α accumulation. ROS further limit the availability of the PHD co-factors FE(II) and ascorbate. [215]

However, we could show in this study that, despite the downregulation of HIF1 α in hypoxic tissues, the total red blood cell count which is regulated by the HIF target EPO was not affected in NMF333 mice. Both mouse lines responded equally with an adequate haematological response to the chronic hypoxic conditions, including an increase in red blood count (RBC), total haemoglobin and haematocrit, as well as a drop in platelets, referred to as hypoxia-induced thrombocytopenia [36], [17].

Erythropoiesis has long been known to be triggered by erythropoietin (EPO), produced mainly in kidney as well as in liver with EPO being a direct target of HIF [77]. In this context the question arises, why NMF333 mice did not show any difference in the haematological response to hypoxia, when the loss of p22phox reduces the hypoxic induction of HIF1 α and its target gene expression. One reason could be, that for EPO it was demonstrated, that it rather stands under the control of HIF2 than HIF1 [77]. Interestingly, HIF2 α stabilization and accumulation was found to be enhanced by NOX4 derived ROS in renal cell carcinoma as well as in the vasculature [46, 129]. Assuming that the p22phox-NOX4 interaction and expression is less impaired by the Y121H mutation in NMF33 mice, an adequate ROS production, HIF2 α response and EPO production in kidney can be expected. However, there

is little evidence in the literature, that the EPO response is directly regulated by NADPH oxidase-derived ROS, but a rather modulating role with NOX4 as additional renal oxygen sensor is assumed [62, 76]. In this context, studies claim that NOX4 produces ROS proportional to the oxygen level – hence reduced superoxide levels at hypoxic conditions – since they found HIF1 α to be destabilized by elevated ROS levels under normoxic conditions. Furthermore, an inhibitory effect of oxidative stress on EPO production was described [62, 179]. In this sense, an impaired NOX4 function would lead to an increased HIF response. Thus, more detailed research on the importance of NADPH oxidase-derived ROS in the context of HIF1 α induction and activation and the hypoxic EPO response is necessary to clarify the situation.

5.3. Effects of p22phox

In our study we were able to demonstrate p22phox as an important player in proliferative pathways, including angiogenesis, PH, vascular remodelling, proliferation and metabolic activity.

5.3.1. P22phox promotes angiogenesis

We could show that NMF333 mice have an impaired vessel forming capacity in a PDGF-driven Matrigel angiogenesis assay under normoxic conditions.

The proangiogenic effect of PDGF is mediated via PDGF receptors (PDGFR) [156] and PDGF has been previously shown to induce and activate NADPH oxidases in endothelial cells [31, 181]. Moreover, ROS derived from NADPH oxidases have been found to promote angiogenesis and neovascularization [192, 203].

ROS are reported to carry out their angiogenic effects in multiple ways. On the one hand, they lead to a direct activation of the VEGF-receptor by autophosphorylation [191]. On the other hand, they promote the activation of transcription factors like HIF1 α and NF- κ B, which then lead to an upregulation of proangiogenic factors like VEGF and PAI-1 [192]. VEGF is known as one of the key regulators in angiogenesis, leading to detachment and migration of endothelial cells from their vessel of origination [113]. In line, PDGF has been previously shown to upregulate HIF1 α in a ROS-dependent manner [211]. Moreover, capillary formation was reduced in p22phox-depleted HMEC-1 under normoxic and hypoxic

conditions, and pulmonary arteries collected from NMF333 mice showed reduced endothelial sprouting compared to WT mice [215]. Furthermore, as shown in the study, hypoxic induction of HIF1 α and its target gene VEGF were attenuated in p22phox-depleted HMEC-1.

Surprisingly, we could observe slightly elevated mRNA levels of VEGF under normoxic conditions in p22phox depleted HMEC-1, whereas the knockdown of p22phox had no influence on HIF1 α and PGK1 mRNA levels, what seems rather unlikely in the above discussed context. However, the interactions between ROS and VEGF are not unilateral, since VEGF is not only described to be induced by hypoxia and ROS, but VEGF can also activate ROS production by NOX2 [191]. Therefore, it just might be, that VEGF expression is enhanced under normoxic conditions in order to compensate for the reduced ROS production due to the p22phox silencing in an attempt to maintain basal levels of ROS as second messengers.

5.3.2. P22phox and pulmonary hypertension

Chronic hypoxia is a common model to induce pulmonary hypertension. To verify pulmonary hypertension, we performed haemodynamic measurements using a transthoracic approach with tip catheterization of the heart. The advantage of this method lies in the short time which is required for the measurements and the access to the left and right heart during one measurement. Indeed, we were able to acquire reproducible pressure values, depicting the development of PH by showing a clear increase in right ventricular systolic, diastolic and mean arterial pressure in mice exposed to chronic hypoxia.

Another, more frequently used approach, is the catheterization of the jugular vein and facultatively of the carotid artery [178, 183]. When comparing pressure values, that are obtained by jugular vein and transthoracic catheterization, higher values have been reported in normoxic as well as in hypoxic WT mice by jugular vein access [33, 183]. On the other hand, pressure data acquired with the transthoracic approach by Chalupsky et. al correspond well with our results (RV sys NX 16 mmHg, RV sys HX 30 mmHg [28]), suggesting a lower pressure record by the transthoracic approach. However, a review that compared right ventricular systolic pressure values, which were measured in context of hypoxia induced pulmonary hypertension between 1996 and 2011, describes a range between 10 to 27 mmHg for normoxic and 14 to 35 mmHg for hypoxic WT mice [69]. We find our values within this range, speaking for the validity of our method. Furthermore, it demonstrates the great

variance of absolute values acquired by different measurement techniques, confirming that individual values must be seen in context of the applied method. Another point we observed is, that we recorded ventricular diastolic pressure values, which fit more to the diastolic values of the arteries. The diastolic pressure measured in the right ventricle should be around 1 mmHg at normoxia and 3 mmHg under hypoxic conditions [183], whereas we measured values around 8 mmHg at normoxia and 14 mmHg at hypoxia. Under physiologic conditions, the semilunar valves close when the pressure in the ventricles falls below the diastolic pressure of the circulation, preventing a backflow of blood. The intraventricular pressure falls around zero, ensuring an easy ventricular refilling during the diastole. The proper closing of the valves and the relaxation of the ventricular wall might be disturbed by the invasiveness of our method, so that we possibly measured diastolic values of the arteries instead of the ventricles. Interestingly, when carefully searching the literature, the pulmonary arterial diastolic pressure is usually not measured. In most cases, only the right ventricular systolic pressure is reported as marker for pulmonary hypertension [28, 33, 39, 178], whereas only in few studies the diastolic right ventricular pressure was additionally measured [41, 183]. Visovatti et al. recorded a pressure curve of the pulmonary arteries with a diastolic value of about 15 mmHg for hypoxic WT mice [196], corresponding well with our own measurements. Though the transthoracic approach delivers stable and reliable systolic values, the diastolic values can only be seen as surrogate parameter for pulmonary arterial diastolic pressure.

As expected from previous findings, the left ventricular pressure values were not influenced by chronic hypoxia [183]. However, a few studies report an increased systemic pressure in rats and humans exposed to hypoxic conditions [25, 193]. We found an elevated diastolic and mean arterial pressure in the left ventricle in hypoxic WT mice, whereas the systolic value remained stable. Though this increase proved to be of statistical significance, it appears to be of no biological relevance, since a systemic mean arterial pressure up to 79 mmHg for WT mice under isoflurane anaesthesia is reported [216]. The elevated MAP in our study was calculated with 49 mmHg compared to 44 mmHg under normoxia. Furthermore, all hypertrophy parameters which were assessed in the left ventricle were not affected by chronic hypoxic exposure.

One of the key questions in this study was, whether p22phox, which we could show to be upregulated by hypoxia, is involved in the development of hypoxia-induced pulmonary arterial hypertension. And indeed, the results of our pressure measurements showed a clearly reduced increase in right ventricular systolic, diastolic and mean arterial pressure in

NMF333 mice compared to WT mice after three weeks of hypoxia. Though the values did not completely reach normoxic levels, they demonstrate that NMF333 mice are at least partially protected against the development of pulmonary arterial hypertension, indicating p22phox and NOX derived ROS are important factors in the pathogenesis of hypoxic PH. Mechanistically, increased levels of ROS have been shown to decrease the bioavailability of NO, which mediates a vasodilatory effect [182]. Moreover, the HIF1 α pathway is known to be involved in the development of hypoxic PAH, since HIF1 α heterozygote knockout mice showed an attenuated pulmonary response to chronic hypoxia as well [213]. As discussed above, NOX- and HIF1 signalling are strongly connected and the integrity of p22phox seems to be important for an adequate HIF response. Thus, it is conceivable, that p22phox and NOX stand at an early position on the way from hypoxia to PH, scavenging the dilatatory NO as well as promoting and enhancing the accumulation of HIF1 α and the expression of its target genes.

Furthermore, NMF333 mice showed no alterations of statistical significance concerning any left ventricular values. These findings confirm the observations made in WT mice, that chronic hypoxia influences the pulmonary circulation, whereas the systemic circulation remains unaffected.

Similar to our study, hypoxic NOX2-K.O. mice, were protected against hypoxia-induced pulmonary hypertension with right ventricular pressure values nearly reaching normoxic levels [120]. This seems surprising, since in NMF333 mice a range of NOX homologues (NOX1-3) is affected by the mutation, which would suggest a greater effect in these mice instead of mice carrying only a knockout of NOX2. So why seem NOX2-K.O. mice to be better protected than p22phox-deficient NMF333 mice? The NOX2-K.O. mouse strain, that was used in this study, carried a complete null-allele of the gp91 gene (*Cybb*) which is located on the X-chromosome. Therefore, male hemizygote mice will already have a complete loss of NOX2 protein [94]. In contrast, the Y121H mutation most likely does not produce a complete knockout like a null allele. As discussed before (5.1.3) it is assumed, that the Y121H mutation leads to an impaired interaction of mutated p22phox with NOX1, NOX2 and NOX3, resulting in a decreased p22phox protein stability and protein half life time [215]. Therefore, it is conceivable, that the penetrance of the NOX2 knockout is higher than the Y121H point mutation at least in cells where NOX2 dominates, which could explain the stronger phenotype observed in the NOX2-K.O. mouse strain. In support of this hypothesis, the EPR measurement from NMF333 leucocytes showed a reduced superoxide production, not a complete abolishment. On the other hand, a stronger inhibitory effect of

the Y121H mutation on ROS production, compared to our observations, was described in the publication by Nakano et al. [144]. However, different measurement methods have been used, therefore a direct comparison might not be valid.

The theory, that NOX4, which is presumably not affected by Y121H [201], could compensate for the loss of the other NOXes in NMF333 mice seems to be irrelevant in the context of the single knockout in the NOX2-K.O. mouse strain and the intactness of the remaining isoforms. Moreover, NOX4-K.O. mice were described not to be protected against hypoxia-induced pulmonary hypertension [195].

5.3.3. P22phox and pulmonary vascular remodelling

The morphological correlate for the increased right ventricular or pulmonary arterial pressure, respectively, in pulmonary hypertension is found in an increased resistance in the lung circulation, caused by the remodelling of small pulmonary arteries [37]. Almost always, pulmonary vascular remodelling includes an increase in vessel muscularization [166]. We could clearly observe in our study, that the number of small muscularized vessels is increased in lungs of WT mice by chronic hypoxia. In accordance with our findings of reduced pressure in the pulmonary circulation, we found a reduced number of neomuscularized vessels in hypoxic p22phox-deficient mice. But, correlating with the pressure values, the vessel number did not reach normoxic levels, hence showing only a reduction of the hypoxic effect, not an abolishment. The process of neomuscularisation is primarily characterized by proliferation of pulmonary artery smooth muscle cells (PASMCs) located in the media [38]. In addition to endothelial cells, ROS are important regulators of proliferation of vascular smooth muscle cells of different vascular beds including the pulmonary vasculature [40, 89]. Thereby, many pathways, including the induction of ET-1, TXA2, PPAR and HIF1 and its target genes, are involved [4]. Moreover, p22phox-dependent NADPH oxidases have been shown to promote proliferation of PASMC in response to hypoxia and many non-hypoxic stimuli [15, 157, 194]. However, these data have been mainly obtained in cultivated PASMCs.

In hypoxic WT lungs we could show indications of proliferation in neomuscularized vessels by staining with the proliferation marker Ki67 [180] while this response was diminished in the absence of p22phox in NMF333 mice [215]. These observations underline, that p22phox can promote proliferation of pulmonary artery smooth muscle cells also in vivo in the context of hypoxia-induced pulmonary hypertension. However, no KI67 could be detected in

endothelial cells. These observations are in line with the absence of plexiform lesions of the endothelial layer in murine lungs, which are typically found in human PAH [2, 177].

This study further showed that the metabolic activity in the lungs of WT-mice was increased by chronic hypoxia as determined by an increased uptake of ^{18}F -FDG. These effects were not present in the absence of p22phox. ^{18}F -FDG PET was described as useful tool in the diagnosis and monitoring of PAH in hypoxic and/ or Sugen rat and mouse models [109, 131]. Furthermore, a higher metabolic activity was measured in lungs and right ventricles of patients with idiopathic PAH [78].

It was suggested that HIF1 α -mediated Glut1 up-regulation in proliferating vascular cells in PAH accounts for increased lung ^{18}F -FDG PET uptake [131], correlating well with the regulation of HIF1 α by p22phox in our model. Together, these findings suggest, that p22phox is mechanistically involved in the process of hypoxic vascular remodelling, the morphological correlate for PAH [166].

5.3.4. P22phox and right ventricular hypertrophy

This study further showed that wildtype mice exposed to chronic hypoxia developed right ventricular hypertrophy as demonstrated by an increased Fulton's index, a widely used tool to assess the amount of RV hypertrophy [123]. Additionally, the ventricular wall diameter index in histological heart sections was increased. Myocyte WGA staining and reexpression of fetal genes such as β -MHC and α -skeletal muscle actin (α SKA) which have been described as sensitive markers for cardiac hypertrophy [99] [125] further confirmed the development of right ventricular hypertrophy in hypoxic wildtype mice. However, right ventricular hypertrophy was markedly reduced in hypoxic NMF333 mice, though not reaching normoxic levels.

Generally, right ventricular hypertrophy is seen as direct reaction of the myocardium to increased pressure of the pulmonary circulation, being the life-limiting factor when eventually leading to cardiac failure. The question is, if the reduced hypertrophy in NMF333 mice is only due to the fact of reduced pulmonary arterial pressure, or if the depletion of p22phox, which was shown to be present in right ventricular tissue, too, also leads to autonomous alterations of the myocardium. Thereby, the first possibility seems to be supported by the fact, that the pressure values and hypertrophy indices always showed the same pattern of regulation, speaking for a strong connection of both. Interestingly, a higher baseline expression level of α SKA was detected in NMF333 mice already under normoxic

conditions. After exposure to chronic hypoxia it did not further increase, suggesting a persistently high expression in p22phox-deficient NMF333 mice. α SKA is usually expressed during fetal development of the heart and is subsequently replaced by the α -cardiac actin (α CA) isoform [50]. Its appearance in adult hearts is associated with increased cardiac contractility in the context of a diseased heart [83], that must maintain the demanded blood supply [125]. A re-expression is therefore correlated with cardiac pathologies, for instance in patients suffering from hypertrophic cardiomyopathy (HCM) [119]. So far, no morphological or functional alterations of the heart were described in NMF333 mice. Moreover, in this study, all cardiac parameters did not substantially differ between normoxic WT and NMF333 mice. However, there is evidence that ROS play a role in the differentiation and maturation of cardiomyocytes [7, 207]. Further research is necessary to evaluate the effect of p22phox on cardiac maturation and differentiation in the *in vivo* context. This might allow to better evaluate whether reduced RV hypertrophy in the absence of p22phox in NMF333 mice might not only be a result of reduced pulmonary vascular remodelling and pressure, but also a result of alterations in the heart itself.

However, ^{18}F -FDG PET studies did not show differences in glucose uptake of the RV and LV between normoxic WT and NMF333 mice arguing against a role of p22phox in controlling basal cardiac glucose metabolism. In response to chronic hypoxia, ^{18}F -FDG uptake was increased in WT mice, confirming previous studies indicating that ^{18}F -FDG PET is sensitive to detect an increased metabolic activity in right ventricles in piglets and rats with early stages of PAH [51, 98]. However, also under hypoxic conditions, p22phox did not contribute to glucose uptake as ^{18}F -FDG uptake was not significantly lower in the RV of NMF333 mice than in the RV of WT mice. In contrast, induction of HIF1 α as one of the drivers of glucose uptake under hypoxia was abolished in the RV of NMF333 mice. Thus, additional, HIF1-independent mechanisms might also contribute to ^{18}F -FDG uptake in the hypoxic heart.

Interestingly, the ^{18}F -FDG uptake was increased by hypoxia not only in the right, but also in the left ventricles of WT and NMF333 mice, although it has been stated, that chronic hypoxia would not affect the left ventricle. It is true, that the left ventricle is not opposed with a pressure overload, therefore no hypertrophic reaction is triggered. Still, the myocardium has to deal with the reduced oxygen partial pressure, just like the right ventricle, resulting in a metabolic shift with increased glucose uptake in both ventricles [109]. Thereby our observations were confirmed by other studies, reporting similar results in mice [92, 109].

5.4. Role of NOX1 in hypoxia-induced pulmonary hypertension

In addition to p22phox, the role of NOX1 in the response to chronic hypoxia was tested. In contrast to the data in NMF333 mice, however, NOX1-K.O. mice were not protected against the development of pulmonary hypertension, pulmonary vascular remodelling and right ventricular hypertrophy by hypoxia, although, similar to p22phox, NOX1 levels were enhanced in response to chronic hypoxia (as shown in recently published data by our group) [215].

In contrast, spontaneous development of pulmonary hypertension and right ventricular hypertrophy has been described in male NOX1-K.O. mice already under normoxic conditions [91]. However, although male NOX1-K.O. have been used in this study, no evidence for PH under normoxic conditions could be collected. When comparing different studies, many factors must be taken into account which can possibly influence the results. First, in our study the mouse strain C57BL/6N was used, a substrain of the widely used C57BL/6J strain. Indeed, several studies describe differences in metabolism and response in experimental settings between the two strains [54, 104]. Second, different approaches to create the knock-out were used in the studies. Finally, the age of the mice is of profound importance. The study used mice at the age of 9 to 18 weeks, while we used younger mice at the age of 9 to 11 weeks. However, additional studies are needed to resolve the role of NOX1 in hypoxia-induced pulmonary hypertension in male mice.

On the other hand, female NOX1-K.O. mice have been reported to be protected against hypoxic PAH [87], similar to NMF33 mice in our study [215] or to NOX2 knockout mice [120]. However, as in this study only male mice have been investigated, further studies are needed to evaluate whether there are also sex-dependent differences in the susceptibility towards hypoxia-induced pulmonary hypertension in this NOX1-K.O. strain. Moreover, NOX1 has been described to play a key role in monocrotaline-induced inflammatory pulmonary hypertension [194]. These findings lead to the idea, that different types of pulmonary hypertension might be influenced by different types of NOX homologues.

5.5. Limitations of the study

Although the NMF333 mouse strain is a good model of p22phox deficiency, it is not a complete knock out since p22phox mRNA levels are preserved. Moreover, not all NOX enzymes seem to be affected in the same way, thus leaving the possibility of a residual NOX4 activity. This NOX4-p22phox interaction should be studied in more detail in vivo and in vitro, using immunoprecipitation, bimolecular fluorescence complementation or the Förster resonance energy transfer for example. A complete knockout of the Cyba gene, produced for instance by a null allele, could clarify the question of incomplete penetrance of the Y121H point mutation. Moreover, it would be interesting to compare the role of p22phox in other PAH models like the monocrotaline injury model or the SUGEN 5416 model although it remains challenging to model human PAH in animals [35]. Since neither the hypoxia model nor any other mouse model available to date is able to fully recapitulate PH in the human, translation of the results to the human situation remains limited. It is thus necessary to further seek for models that match the different types of PH, represented by the clinical PH classification, in order to be able to model the different pathophysiological aspects of this complex disease as closely as possible.

5.6. Conclusion

In this study it was demonstrated that p22phox and NADPH oxidase derived ROS play a role in the development of chronic hypoxia induced pulmonary arterial hypertension in mice. We could show, that the hypoxia induced upregulation of p22phox protein expression was reduced by the Y121H mutation in NMF333 mice, resulting in a reduced ROS production rate. In consequence p22phox-deficient NMF333 mice exposed to chronic hypoxia were partially protected against the development of PAH, pulmonary vascular remodelling and right ventricular hypertrophy. Moreover, the modulation of proliferative and metabolic markers in NMF333 mice suggests the involvement of ROS in different pathways, including proliferation and angiogenesis. Of particular importance, p22phox contributes to the hypoxic regulation of HIF1 α , a major player in the cellular and systemic response to hypoxia and in the pathogenesis of hypoxia-induced pulmonary hypertension, in vitro and in vivo.

The role of p22phox-dependent NADPH oxidases, however, does not recapitulate in all NOX enzymes, since male NOX1-K.O. were not protected against hypoxia-induced pulmonary hypertension.

Further research and other models of PAH are necessary to complete the picture and uncover the complex mechanisms connecting NADPH oxidases, ROS and PAH. However, the pathway carries the potential to be targeted in new therapeutic approaches to find cure for this life-limiting disease.

6. References

1. Aaronson, P.I., Robertson, T.P., Knock, G.A., Becker, S., Lewis, T.H., Snetkov, V., and Ward, J.P., *Hypoxic pulmonary vasoconstriction: mechanisms and controversies*. J Physiol, 2006. **570**(Pt 1): p. 53-8.
2. Abe, K., Toba, M., Alzoubi, A., Ito, M., Fagan, K.A., Cool, C.D., Voelkel, N.F., Mcmurtry, I.F., and Oka, M., *Formation of plexiform lesions in experimental severe pulmonary arterial hypertension*. Circulation, 2010. **121**(25): p. 2747-54.
3. Ades, E.W., Candal, F.J., Swerlick, R.A., George, V.G., Summers, S., Bosse, D.C., and Lawley, T.J., *HMEC-1: establishment of an immortalized human microvascular endothelial cell line*. J Invest Dermatol, 1992. **99**(6): p. 683-90.
4. Aggarwal, S., Gross, C.M., Sharma, S., Fineman, J.R., and Black, S.M., *Reactive oxygen species in pulmonary vascular remodeling*. Compr Physiol, 2013. **3**(3): p. 1011-34.
5. Alturkistani, H.A., Tashkandi, F.M., and Mohammedsaleh, Z.M., *Histological Stains: A Literature Review and Case Study*. Glob J Health Sci, 2015. **8**(3): p. 72-9.
6. Ambasta, R.K., Kumar, P., Griendling, K.K., Schmidt, H.H., Busse, R., and Brandes, R.P., *Direct interaction of the novel Nox proteins with p22phox is required for the formation of a functionally active NADPH oxidase*. J Biol Chem, 2004. **279**(44): p. 45935-41.
7. Ateghang, B., Wartenberg, M., Gassmann, M., and Sauer, H., *Regulation of cardiotrophin-1 expression in mouse embryonic stem cells by HIF-1alpha and intracellular reactive oxygen species*. J Cell Sci, 2006. **119**(Pt 6): p. 1043-52.
8. Babelova, A., Avaniadi, D., Jung, O., Fork, C., Beckmann, J., Kosowski, J., Weissmann, N., Anilkumar, N., Shah, A.M., Schaefer, L., Schroder, K., and Brandes, R.P., *Role of Nox4 in murine models of kidney disease*. Free Radic Biol Med, 2012. **53**(4): p. 842-53.
9. Badlam, J.B. and Bull, T.M., *Steps forward in the treatment of pulmonary arterial hypertension: latest developments and clinical opportunities*. Ther Adv Chronic Dis, 2017. **8**(2-3): p. 47-64.
10. Banfi, B., Clark, R.A., Steger, K., and Krause, K.H., *Two novel proteins activate superoxide generation by the NADPH oxidase NOX1*. J Biol Chem, 2003. **278**(6): p. 3510-3.
11. Banfi, B., Malgrange, B., Knisz, J., Steger, K., Dubois-Dauphin, M., and Krause, K.H., *NOX3, a superoxide-generating NADPH oxidase of the inner ear*. J Biol Chem, 2004. **279**(44): p. 46065-72.
12. Baradaran, A., Nasri, H., and Rafieian-Kopaei, M., *Oxidative stress and hypertension: Possibility of hypertension therapy with antioxidants*. J Res Med Sci, 2014. **19**(4): p. 358-67.
13. Belaiba, R.S., Bonello, S., Zahringer, C., Schmidt, S., Hess, J., Kietzmann, T., and Gorlach, A., *Hypoxia up-regulates hypoxia-inducible factor-1alpha transcription by involving phosphatidylinositol 3-kinase and nuclear factor kappaB in pulmonary artery smooth muscle cells*. Mol Biol Cell, 2007. **18**(12): p. 4691-7.
14. Berthelot, E., Bailly, M.T., Hatimi, S.E., Robard, I., Rezgui, H., Bouchachi, A., Montani, D., Sitbon, O., Chemla, D., and Assayag, P., *Pulmonary hypertension due to left heart disease*. Arch Cardiovasc Dis, 2017. **110**(6-7): p. 420-431.
15. Biasin, V., Chwalek, K., Wilhelm, J., Best, J., Marsh, L.M., Ghanim, B., Klepetko, W., Fink, L., Schermuly, R.T., Weissmann, N., Olschewski, A., and Kwapiszewska, G., *Endothelin-1 driven proliferation of pulmonary arterial smooth muscle cells is c-fos dependent*. Int J Biochem Cell Biol, 2014. **54**: p. 137-48.

16. Biberstine-Kinkade, K.J., Yu, L., Stull, N., Leroy, B., Bennett, S., Cross, A., and Dinauer, M.C., *Mutagenesis of p22(phox) histidine 94. A histidine in this position is not required for flavocytochrome b558 function.* J Biol Chem, 2002. **277**(33): p. 30368-74.
17. Birks, J.W., Klassen, L.W., and Gurney, C.W., *Hypoxia-induced thrombocytopenia in mice.* J Lab Clin Med, 1975. **86**(2): p. 230-8.
18. Bitesize Bio. *How Histology Slides are Prepared 2017* [cited 2018 March 19]; Available from: <https://bitesizebio.com/13398/how-histology-slides-are-prepared/>.
19. Block, M.L., Zecca, L., and Hong, J.S., *Microglia-mediated neurotoxicity: uncovering the molecular mechanisms.* Nat Rev Neurosci, 2007. **8**(1): p. 57-69.
20. Bonekamp, N.A., Volkl, A., Fahimi, H.D., and Schrader, M., *Reactive oxygen species and peroxisomes: struggling for balance.* Biofactors, 2009. **35**(4): p. 346-55.
21. Brieger, K., Schiavone, S., Miller, F.J., Jr., and Krause, K.H., *Reactive oxygen species: from health to disease.* Swiss Med Wkly, 2012. **142**: p. w13659.
22. Brown, D.I. and Griendling, K.K., *Nox proteins in signal transduction.* Free Radic Biol Med, 2009. **47**(9): p. 1239-53.
23. Burke, D.L., Frid, M.G., Kunrath, C.L., Karoor, V., Anwar, A., Wagner, B.D., Strassheim, D., and Stenmark, K.R., *Sustained hypoxia promotes the development of a pulmonary artery-specific chronic inflammatory microenvironment.* Am J Physiol Lung Cell Mol Physiol, 2009. **297**(2): p. L238-50.
24. Cafaro, R.P., *Hypoxia: Its Causes and Symptoms.* J Am Dent Soc Anesthesiol, 1960. **7**(4): p. 4-8.
25. Calbet, J.A., *Chronic hypoxia increases blood pressure and noradrenaline spillover in healthy humans.* J Physiol, 2003. **551**(Pt 1): p. 379-86.
26. Campian, M.E., Hardziyenka, M., Michel, M.C., and Tan, H.L., *How valid are animal models to evaluate treatments for pulmonary hypertension?* Naunyn Schmiedebergs Arch Pharmacol, 2006. **373**(6): p. 391-400.
27. Carreno, J.E., Apablaza, F., Ocaranza, M.P., and Jalil, J.E., *[Cardiac hypertrophy: molecular and cellular events].* Rev Esp Cardiol, 2006. **59**(5): p. 473-86.
28. Chalupsky, K., Kracun, D., Kanchev, I., Bertram, K., and Gorlach, A., *Folic Acid Promotes Recycling of Tetrahydrobiopterin and Protects Against Hypoxia-Induced Pulmonary Hypertension by Recoupling Endothelial Nitric Oxide Synthase.* Antioxid Redox Signal, 2015. **23**(14): p. 1076-91.
29. Chang, T.C., Huang, C.J., Tam, K., Chen, S.F., Tan, K.T., Tsai, M.S., Lin, T.N., and Shyue, S.K., *Stabilization of hypoxia-inducible factor-1{alpha} by prostacyclin under prolonged hypoxia via reducing reactive oxygen species level in endothelial cells.* J Biol Chem, 2005. **280**(44): p. 36567-74.
30. Chen, H. and Costa, M., *Iron- and 2-oxoglutarate-dependent dioxygenases: an emerging group of molecular targets for nickel toxicity and carcinogenicity.* Biometals, 2009. **22**(1): p. 191-6.
31. Chen, K.C., Zhou, Y., Zhang, W., and Lou, M.F., *Control of PDGF-induced reactive oxygen species (ROS) generation and signal transduction in human lens epithelial cells.* Mol Vis, 2007. **13**: p. 374-87.
32. Chester, A.H. and Yacoub, M.H., *The role of endothelin-1 in pulmonary arterial hypertension.* Glob Cardiol Sci Pract, 2014. **2014**(2): p. 62-78.
33. Ciuculan, L., Bonneau, O., Hussey, M., Duggan, N., Holmes, A.M., Good, R., Stringer, R., Jones, P., Morrell, N.W., Jarai, G., Walker, C., Westwick, J., and Thomas, M., *A novel murine model of severe pulmonary arterial hypertension.* Am J Respir Crit Care Med, 2011. **184**(10): p. 1171-82.
34. Coleman, J.L., Brennan, K., Ngo, T., Balaji, P., Graham, R.M., and Smith, N.J., *Rapid Knockout and Reporter Mouse Line Generation and Breeding Colony*

- Establishment Using EUCOMM Conditional-Ready Embryonic Stem Cells: A Case Study.* Front Endocrinol (Lausanne), 2015. **6**: p. 105.
35. Colvin, K.L. and Yeager, M.E., *Animal Models of Pulmonary Hypertension: Matching Disease Mechanisms to Etiology of the Human Disease.* J Pulm Respir Med, 2014. **4**(4).
 36. Cottrell, M.B., Jackson, C.W., and McDonald, T.P., *Hypoxia increases erythropoiesis and decreases thrombocytopoiesis in mice: a comparison of two mouse strains.* Proc Soc Exp Biol Med, 1991. **197**(3): p. 261-7.
 37. Crnkovic, S., Hrszenjak, A., Marsh, L.M., Olschewski, A., and Kwapiszewska, G., *Origin of neomuscularized vessels in mice exposed to chronic hypoxia.* Respir Physiol Neurobiol, 2011. **179**(2-3): p. 342-5.
 38. Crosswhite, P. and Sun, Z., *Molecular mechanisms of pulmonary arterial remodeling.* Mol Med, 2014. **20**: p. 191-201.
 39. Cruz, J.A., Bauer, E.M., Rodriguez, A.I., Gangopadhyay, A., Zeineh, N.S., Wang, Y., Shiva, S., Champion, H.C., and Bauer, P.M., *Chronic hypoxia induces right heart failure in caveolin-1-/- mice.* Am J Physiol Heart Circ Physiol, 2012. **302**(12): p. H2518-27.
 40. Day, R.M. and Suzuki, Y.J., *Cell proliferation, reactive oxygen and cellular glutathione.* Dose Response, 2006. **3**(3): p. 425-42.
 41. Dayeh, N.R., Tardif, J.C., Shi, Y., Tanguay, M., Ledoux, J., and Dupuis, J., *Echocardiographic validation of pulmonary hypertension due to heart failure with reduced ejection fraction in mice.* Sci Rep, 2018. **8**(1): p. 1363.
 42. Decicco-Skinner, K.L., Henry, G.H., Cataisson, C., Tabib, T., Gwilliam, J.C., Watson, N.J., Bullwinkle, E.M., Falkenburg, L., O'Neill, R.C., Morin, A., and Wiest, J.S., *Endothelial cell tube formation assay for the in vitro study of angiogenesis.* J Vis Exp, 2014(91): p. e51312.
 43. Demoncheaux, E.A., Higenbottam, T.W., Kiely, D.G., Wong, J.M., Wharton, S., Varcoe, R., Siddons, T., Spivey, A.C., Hall, K., and Gize, A.P., *Decreased whole body endogenous nitric oxide production in patients with primary pulmonary hypertension.* J Vasc Res, 2005. **42**(2): p. 133-6.
 44. Dengler, V.L., Galbraith, M., and Espinosa, J.M., *Transcriptional regulation by hypoxia inducible factors.* Crit Rev Biochem Mol Biol, 2014. **49**(1): p. 1-15.
 45. Diebold, B.A. and Bokoch, G.M., *Molecular basis for Rac2 regulation of phagocyte NADPH oxidase.* Nat Immunol, 2001. **2**(3): p. 211-5.
 46. Diebold, I., Flugel, D., Becht, S., Belaiba, R.S., Bonello, S., Hess, J., Kietzmann, T., and Gorlach, A., *The hypoxia-inducible factor-2alpha is stabilized by oxidative stress involving NOX4.* Antioxid Redox Signal, 2010. **13**(4): p. 425-36.
 47. Diebold, I., Petry, A., Hess, J., and Gorlach, A., *The NADPH oxidase subunit NOX4 is a new target gene of the hypoxia-inducible factor-1.* Mol Biol Cell, 2010. **21**(12): p. 2087-96.
 48. Diebold, I., Petry, A., Sabrane, K., Djordjevic, T., Hess, J., and Gorlach, A., *The HIF1 target gene NOX2 promotes angiogenesis through urotensin-II.* J Cell Sci, 2012. **125**(Pt 4): p. 956-64.
 49. Djordjevic, T., Pogrebniak, A., Belaiba, R.S., Bonello, S., Wotzlaw, C., Acker, H., Hess, J., and Gorlach, A., *The expression of the NADPH oxidase subunit p22phox is regulated by a redox-sensitive pathway in endothelial cells.* Free Radic Biol Med, 2005. **38**(5): p. 616-30.
 50. Driesen, R.B., Verheyen, F.K., Debie, W., Blaauw, E., Babiker, F.A., Cornelussen, R.N., Ausma, J., Lenders, M.H., Borgers, M., Chaponnier, C., and Ramaekers, F.C., *Re-expression of alpha skeletal actin as a marker for dedifferentiation in cardiac pathologies.* J Cell Mol Med, 2009. **13**(5): p. 896-908.

51. Drozd, K., Ahmadi, A., Deng, Y., Jiang, B., Petryk, J., Thorn, S., Stewart, D., Beanlands, R., Dekemp, R.A., Dasilva, J.N., and Mielniczuk, L.M., *Effects of an endothelin receptor antagonist, Macitentan, on right ventricular substrate utilization and function in a Sugen 5416/hypoxia rat model of severe pulmonary arterial hypertension*. J Nucl Cardiol, 2017. **24**(6): p. 1979-1989.
52. Dumitrascu, R., Koebrich, S., Dony, E., Weissmann, N., Savai, R., Pullamsetti, S.S., Ghofrani, H.A., Samidurai, A., Traupe, H., Seeger, W., Grimminger, F., and Schermuly, R.T., *Characterization of a murine model of monocrotaline pyrrole-induced acute lung injury*. BMC Pulm Med, 2008. **8**: p. 25.
53. E, A.M., *Hypoxic pulmonary vasoconstriction*. Essays Biochem, 2007. **43**: p. 61-76.
54. Enriquez, J.A., *Mind your mouse strain*. Nat Metab, 2019. **1**: p. 5-7.
55. Eun, H.S., Cho, S.Y., Joo, J.S., Kang, S.H., Moon, H.S., Lee, E.S., Kim, S.H., and Lee, B.S., *Gene expression of NOX family members and their clinical significance in hepatocellular carcinoma*. Sci Rep, 2017. **7**(1): p. 11060.
56. Falcetti, E., Flavell, D.M., Staels, B., Tinker, A., Haworth, S.G., and Clapp, L.H., *IP receptor-dependent activation of PPARgamma by stable prostacyclin analogues*. Biochem Biophys Res Commun, 2007. **360**(4): p. 821-7.
57. Finkel, T. and Holbrook, N.J., *Oxidants, oxidative stress and the biology of ageing*. Nature, 2000. **408**(6809): p. 239-47.
58. Fiorentino, T.V., Prioleta, A., Zuo, P., and Folli, F., *Hyperglycemia-induced oxidative stress and its role in diabetes mellitus related cardiovascular diseases*. Curr Pharm Des, 2013. **19**(32): p. 5695-703.
59. Fischer, A.H., Jacobson, K.A., Rose, J., and Zeller, R., *Hematoxylin and eosin staining of tissue and cell sections*. CSH Protoc, 2008. **2008**: p. pdb prot4986.
60. Fischer, M.H., *The Toxic Effects of Formaldehyde and Formalin*. J Exp Med, 1905. **6**(4-6): p. 487-518.
61. Garibyan, L. and Avashia, N., *Polymerase chain reaction*. J Invest Dermatol, 2013. **133**(3): p. 1-4.
62. Geiszt, M., Kopp, J.B., Varnai, P., and Leto, T.L., *Identification of renox, an NAD(P)H oxidase in kidney*. Proc Natl Acad Sci U S A, 2000. **97**(14): p. 8010-4.
63. Gene [Internet]. Bethesda (Md): National Library of Medicine (Us), N.C.F.B.I., *Cyba cytochrome b-245, alpha polypeptide [Mus musculus (house mouse)]*; Gene ID: 13057, updated on 12-Aug-2019. 2019.
64. Ghio, A.J., Nozik-Grayck, E., Turi, J., Jaspers, I., Mercatante, D.R., Kole, R., and Piantadosi, C.A., *Superoxide-dependent iron uptake: a new role for anion exchange protein 2*. Am J Respir Cell Mol Biol, 2003. **29**(6): p. 653-60.
65. Giaid, A. and Saleh, D., *Reduced expression of endothelial nitric oxide synthase in the lungs of patients with pulmonary hypertension*. N Engl J Med, 1995. **333**(4): p. 214-21.
66. Giaid, A., Yanagisawa, M., Langleben, D., Michel, R.P., Levy, R., Shennib, H., Kimura, S., Masaki, T., Duguid, W.P., and Stewart, D.J., *Expression of endothelin-1 in the lungs of patients with pulmonary hypertension*. N Engl J Med, 1993. **328**(24): p. 1732-9.
67. Gladyshev, V.N., *The free radical theory of aging is dead. Long live the damage theory!* Antioxid Redox Signal, 2014. **20**(4): p. 727-31.
68. Goldberg, A.B., Mazur, W., and Kalra, D.K., *Pulmonary hypertension: diagnosis, imaging techniques, and novel therapies*. Cardiovasc Diagn Ther, 2017. **7**(4): p. 405-417.
69. Gomez-Arroyo, J., Saleem, S.J., Mizuno, S., Syed, A.A., Bogaard, H.J., Abbate, A., Taraseviciene-Stewart, L., Sung, Y., Kraskauskas, D., Farkas, D., Conrad, D.H., Nicolls, M.R., and Voelkel, N.F., *A brief overview of mouse models of pulmonary*

- arterial hypertension: problems and prospects*. Am J Physiol Lung Cell Mol Physiol, 2012. **302**(10): p. L977-91.
70. Gorlach, A., Diebold, I., Schini-Kerth, V.B., Berchner-Pfannschmidt, U., Roth, U., Brandes, R.P., Kietzmann, T., and Busse, R., *Thrombin activates the hypoxia-inducible factor-1 signaling pathway in vascular smooth muscle cells: Role of the p22(phox)-containing NADPH oxidase*. Circ Res, 2001. **89**(1): p. 47-54.
 71. Gorlach, A., Holtermann, G., Jelkmann, W., Hancock, J.T., Jones, S.A., Jones, O.T., and Acker, H., *Photometric characteristics of haem proteins in erythropoietin-producing hepatoma cells (HepG2)*. Biochem J, 1993. **290 (Pt 3)**: p. 771-6.
 72. Gorlach, A. and Kietzmann, T., *Superoxide and derived reactive oxygen species in the regulation of hypoxia-inducible factors*. Methods Enzymol, 2007. **435**: p. 421-46.
 73. Graham, A.M. and Presnell, J.S., *Hypoxia Inducible Factor (HIF) transcription factor family expansion, diversification, divergence and selection in eukaryotes*. PLoS One, 2017. **12**(6): p. e0179545.
 74. Gray, S.P., Di Marco, E., Okabe, J., Szyndralewicz, C., Heitz, F., Montezano, A.C., De Haan, J.B., Koulis, C., El-Osta, A., Andrews, K.L., Chin-Dusting, J.P., Touyz, R.M., Winkler, K., Cooper, M.E., Schmidt, H.H., and Jandeleit-Dahm, K.A., *NADPH oxidase 1 plays a key role in diabetes mellitus-accelerated atherosclerosis*. Circulation, 2013. **127**(18): p. 1888-902.
 75. Groemping, Y. and Rittinger, K., *Activation and assembly of the NADPH oxidase: a structural perspective*. Biochem J, 2005. **386**(Pt 3): p. 401-16.
 76. Haase, V.H., *Mechanisms of hypoxia responses in renal tissue*. J Am Soc Nephrol, 2013. **24**(4): p. 537-41.
 77. Haase, V.H., *Regulation of erythropoiesis by hypoxia-inducible factors*. Blood Rev, 2013. **27**(1): p. 41-53.
 78. Hagan, G., Southwood, M., Treacy, C., Ross, R.M., Soon, E., Coulson, J., Sheares, K., Screatton, N., Pepke-Zaba, J., Morrell, N.W., and Rudd, J.H., *(18)FDG PET imaging can quantify increased cellular metabolism in pulmonary arterial hypertension: A proof-of-principle study*. Pulm Circ, 2011. **1**(4): p. 448-55.
 79. Hahne, M., Schumann, P., Mursell, M., Strehl, C., Hoff, P., Buttgereit, F., and Gaber, T., *Unraveling the role of hypoxia-inducible factor (HIF)-1alpha and HIF-2alpha in the adaption process of human microvascular endothelial cells (HMEC-1) to hypoxia: Redundant HIF-dependent regulation of macrophage migration inhibitory factor*. Microvasc Res, 2018. **116**: p. 34-44.
 80. Hankinson, O., *Why does ARNT2 behave differently from ARNT?* Toxicol Sci, 2008. **103**(1): p. 1-3.
 81. Harvard Apparatus Uk. *Fluovac System*. 2018 [cited 2018 11 March]; Available from: http://www.harvardapparatus.co.uk/webapp/wcs/stores/servlet/haisku3_10001_115_55_33525_-1_HAUK_ProductDetail_N_37326_37327_37331.
 82. Hensley, K., Robinson, K.A., Gabbita, S.P., Salsman, S., and Floyd, R.A., *Reactive oxygen species, cell signaling, and cell injury*. Free Radic Biol Med, 2000. **28**(10): p. 1456-62.
 83. Hewett, T.E., Grupp, I.L., Grupp, G., and Robbins, J., *Alpha-skeletal actin is associated with increased contractility in the mouse heart*. Circ Res, 1994. **74**(4): p. 740-6.
 84. Hoepfer, M.M., Ghofrani, H.A., Grunig, E., Klose, H., Olschewski, H., and Rosenkranz, S., *Pulmonary Hypertension*. Dtsch Arztebl Int, 2017. **114**(5): p. 73-84.

85. Hoepfer, M.M., Humbert, M., Souza, R., Idrees, M., Kawut, S.M., Sliwa-Hahnle, K., Jing, Z.C., and Gibbs, J.S., *A global view of pulmonary hypertension*. *Lancet Respir Med*, 2016. **4**(4): p. 306-22.
86. Hoepfer, M.M., Huscher, D., and Pittrow, D., *Incidence and prevalence of pulmonary arterial hypertension in Germany*. *Int J Cardiol*, 2016. **203**: p. 612-3.
87. Hood, K.Y., Montezano, A.C., Harvey, A.P., Nilsen, M., Maclean, M.R., and Touyz, R.M., *Nicotinamide Adenine Dinucleotide Phosphate Oxidase-Mediated Redox Signaling and Vascular Remodeling by 16alpha-Hydroxyestrone in Human Pulmonary Artery Cells: Implications in Pulmonary Arterial Hypertension*. *Hypertension*, 2016. **68**(3): p. 796-808.
88. Hordijk, P.L., *Regulation of NADPH oxidases: the role of Rac proteins*. *Circ Res*, 2006. **98**(4): p. 453-62.
89. Huetsch, J.C., Suresh, K., and Shimoda, L.A., *Regulation of Smooth Muscle Cell Proliferation by NADPH Oxidases in Pulmonary Hypertension*. *Antioxidants (Basel)*, 2019. **8**(3).
90. Human Protein Atlas. *Tissue expression of CYBA*. [cited 2020 7 March]; CYBA, gene available from v19.3.proteinatlas.org:[Available from: <https://www.proteinatlas.org/ENSG00000051523-CYBA/tissue/primary+data>].
91. Iwata, K., Ikami, K., Matsuno, K., Yamashita, T., Shiba, D., Ibi, M., Matsumoto, M., Katsuyama, M., Cui, W., Zhang, J., Zhu, K., Takei, N., Kokai, Y., Ohneda, O., Yokoyama, T., and Yabe-Nishimura, C., *Deficiency of NOX1/nicotinamide adenine dinucleotide phosphate, reduced form oxidase leads to pulmonary vascular remodeling*. *Arterioscler Thromb Vasc Biol*, 2014. **34**(1): p. 110-9.
92. Izquierdo-Garcia, J.L., Arias, T., Rojas, Y., Garcia-Ruiz, V., Santos, A., Martin-Puig, S., and Ruiz-Cabello, J., *Metabolic Reprogramming in the Heart and Lung in a Murine Model of Pulmonary Arterial Hypertension*. *Front Cardiovasc Med*, 2018. **5**: p. 110.
93. Jackson Laboratory. *How to time mouse pregnancy*. 2018 [cited 2018 11 March]; Available from: <https://www.jax.org/news-and-insights/2006/april/how-to-time-mouse-pregnancy#>.
94. Jackson Laboratory. *MOUSE STRAIN DATASHEET - 002365*. 2018 [cited 2018 23 Novembre]; Available from: <https://www.jax.org/strain/002365>.
95. Jackson Laboratory. *MOUSE STRAIN DATASHEET - 005445*. 2018 [cited 2018 30 Septembre]; Available from: <https://www.jax.org/strain/005445>.
96. Jasinska-Stroschein, M. and Orszulak-Michalak, D., *Novel strategies for treatment of pulmonary arterial hypertension*. *Postepy Hig Med Dosw (Online)*, 2017. **71**(0): p. 577-588.
97. Jelkmann, W., *Regulation of erythropoietin production*. *J Physiol*, 2011. **589**(Pt 6): p. 1251-8.
98. Jiang, Y.Y. and He, G.W., *Early Diagnostic Features of Left-to-Right Shunt-Induced Pulmonary Arterial Hypertension in Piglets*. *Ann Thorac Surg*, 2018. **106**(5): p. 1396-1405.
99. Jones, W.K., Grupp, I.L., Doetschman, T., Grupp, G., Osinska, H., Hewett, T.E., Boivin, G., Gulick, J., Ng, W.A., and Robbins, J., *Ablation of the murine alpha myosin heavy chain gene leads to dosage effects and functional deficits in the heart*. *J Clin Invest*, 1996. **98**(8): p. 1906-17.
100. Juhasz, A., Ge, Y., Markel, S., Chiu, A., Matsumoto, L., Van Balgooy, J., Roy, K., and Doroshov, J.H., *Expression of NADPH oxidase homologues and accessory genes in human cancer cell lines, tumours and adjacent normal tissues*. *Free Radic Res*, 2009. **43**(6): p. 523-32.

101. Jung, S.N., Yang, W.K., Kim, J., Kim, H.S., Kim, E.J., Yun, H., Park, H., Kim, S.S., Choe, W., Kang, I., and Ha, J., *Reactive oxygen species stabilize hypoxia-inducible factor-1 alpha protein and stimulate transcriptional activity via AMP-activated protein kinase in DU145 human prostate cancer cells*. *Carcinogenesis*, 2008. **29**(4): p. 713-21.
102. Kaelin, W.G., Jr. and Ratcliffe, P.J., *Oxygen sensing by metazoans: the central role of the HIF hydroxylase pathway*. *Mol Cell*, 2008. **30**(4): p. 393-402.
103. Kalantari, S. and Gombert-Maitland, M., *Group 5 Pulmonary Hypertension: The Orphan's Orphan Disease*. *Cardiol Clin*, 2016. **34**(3): p. 443-9.
104. Kang, S.K., Hawkins, N.A., and Kearney, J.A., *C57BL/6J and C57BL/6N substrains differentially influence phenotype severity in the Scn1a (+/-) mouse model of Dravet syndrome*. *Epilepsia Open*, 2019. **4**(1): p. 164-169.
105. Kawahara, T., Ritsick, D., Cheng, G., and Lambeth, J.D., *Point mutations in the proline-rich region of p22phox are dominant inhibitors of Nox1- and Nox2-dependent reactive oxygen generation*. *J Biol Chem*, 2005. **280**(36): p. 31859-69.
106. Kelton, J.G. and Blajchman, M.A., *Prostaglandin I2 (prostacyclin)*. *Can Med Assoc J*, 1980. **122**(2): p. 175-9.
107. Knowles, H.J., Raval, R.R., Harris, A.L., and Ratcliffe, P.J., *Effect of ascorbate on the activity of hypoxia-inducible factor in cancer cells*. *Cancer Res*, 2003. **63**(8): p. 1764-8.
108. Kohchi, C., Inagawa, H., Nishizawa, T., and Soma, G., *ROS and innate immunity*. *Anticancer Res*, 2009. **29**(3): p. 817-21.
109. Komniski, M.S., Yakushev, S., Bogdanov, N., Gassmann, M., and Bogdanova, A., *Interventricular heterogeneity in rat heart responses to hypoxia: the tuning of glucose metabolism, ion gradients, and function*. *Am J Physiol Heart Circ Physiol*, 2011. **300**(5): p. H1645-52.
110. Korsholm, K., Andersen, A., Kirkfeldt, R.E., Hansen, K.N., Mellekjær, S., and Nielsen-Kudsk, J.E., *Survival in an incident cohort of patients with pulmonary arterial hypertension in Denmark*. *Pulm Circ*, 2015. **5**(2): p. 364-9.
111. Kotch, L.E., Iyer, N.V., Laughner, E., and Semenza, G.L., *Defective vascularization of HIF-1alpha-null embryos is not associated with VEGF deficiency but with mesenchymal cell death*. *Dev Biol*, 1999. **209**(2): p. 254-67.
112. Krenz, M. and Robbins, J., *Impact of beta-myosin heavy chain expression on cardiac function during stress*. *J Am Coll Cardiol*, 2004. **44**(12): p. 2390-7.
113. Krock, B.L., Skuli, N., and Simon, M.C., *Hypoxia-induced angiogenesis: good and evil*. *Genes Cancer*, 2011. **2**(12): p. 1117-33.
114. Kruger, N.J., *The Bradford method for protein quantitation*. *Methods Mol Biol*, 1994. **32**: p. 9-15.
115. Lachant, D.J., Meoli, D.F., Haight, D., Lyons, J.A., Swarthout, R.F., and White, R.J., *Low dose monocrotaline causes a selective pulmonary vascular lesion in male and female pneumonectomized rats*. *Exp Lung Res*, 2018. **44**(1): p. 51-61.
116. Lahm, H., Doppler, S., Dressen, M., Werner, A., Adamczyk, K., Schrambke, D., Brade, T., Laugwitz, K.L., Deutsch, M.A., Schiemann, M., Lange, R., Moretti, A., and Krane, M., *Live fluorescent RNA-based detection of pluripotency gene expression in embryonic and induced pluripotent stem cells of different species*. *Stem Cells*, 2015. **33**(2): p. 392-402.
117. Law, R.B., H., *The physiology of oxygen delivery*. *Update in Anaesthesia*, 1999(10).
118. Li, R., Jia, Z., and Trush, M.A., *Defining ROS in Biology and Medicine*. *React Oxy Species (Apex)*, 2016. **1**(1): p. 9-21.

119. Lim, D.S., Roberts, R., and Marian, A.J., *Expression profiling of cardiac genes in human hypertrophic cardiomyopathy: insight into the pathogenesis of phenotypes*. J Am Coll Cardiol, 2001. **38**(4): p. 1175-80.
120. Liu, J.Q., Zelko, I.N., Erbynn, E.M., Sham, J.S., and Folz, R.J., *Hypoxic pulmonary hypertension: role of superoxide and NADPH oxidase (gp91phox)*. Am J Physiol Lung Cell Mol Physiol, 2006. **290**(1): p. L2-10.
121. Loukogeorgakis, S.P., Van Den Berg, M.J., Sofat, R., Nitsch, D., Charakida, M., Haiyee, B., De Groot, E., Macallister, R.J., Kuijpers, T.W., and Deanfield, J.E., *Role of NADPH oxidase in endothelial ischemia/reperfusion injury in humans*. Circulation, 2010. **121**(21): p. 2310-6.
122. Lundberg, Y.W., Xu, Y., Thiessen, K.D., and Kramer, K.L., *Mechanisms of otoconia and otolith development*. Dev Dyn, 2015. **244**(3): p. 239-53.
123. Ma, Z., Mao, L., and Rajagopal, S., *Hemodynamic Characterization of Rodent Models of Pulmonary Arterial Hypertension*. J Vis Exp, 2016(110).
124. Maarman, G., Lecour, S., Butrous, G., Thienemann, F., and Sliwa, K., *A comprehensive review: the evolution of animal models in pulmonary hypertension research; are we there yet?* Pulm Circ, 2013. **3**(4): p. 739-56.
125. Machackova, J., Barta, J., and Dhalla, N.S., *Myofibrillar remodeling in cardiac hypertrophy, heart failure and cardiomyopathies*. Can J Cardiol, 2006. **22**(11): p. 953-68.
126. Malinda, K.M., *In vivo matrigel migration and angiogenesis assay*. Methods Mol Biol, 2009. **467**: p. 287-94.
127. Mandl, M. and Depping, R., *Hypoxia-inducible aryl hydrocarbon receptor nuclear translocator (ARNT) (HIF-1beta): is it a rare exception?* Mol Med, 2014. **20**: p. 215-20.
128. Manea, A., Manea, S.A., Gafencu, A.V., and Raicu, M., *Regulation of NADPH oxidase subunit p22(phox) by NF-kB in human aortic smooth muscle cells*. Arch Physiol Biochem, 2007. **113**(4-5): p. 163-72.
129. Maranchie, J.K. and Zhan, Y., *Nox4 is critical for hypoxia-inducible factor 2-alpha transcriptional activity in von Hippel-Lindau-deficient renal cell carcinoma*. Cancer Res, 2005. **65**(20): p. 9190-3.
130. Maron, B.A. and Galie, N., *Diagnosis, Treatment, and Clinical Management of Pulmonary Arterial Hypertension in the Contemporary Era: A Review*. JAMA Cardiol, 2016. **1**(9): p. 1056-1065.
131. Marsboom, G., Wietholt, C., Haney, C.R., Toth, P.T., Ryan, J.J., Morrow, E., Thenappan, T., Bache-Wiig, P., Piao, L., Paul, J., Chen, C.T., and Archer, S.L., *Lung (1)(8)F-fluorodeoxyglucose positron emission tomography for diagnosis and monitoring of pulmonary arterial hypertension*. Am J Respir Crit Care Med, 2012. **185**(6): p. 670-9.
132. Martyn, K.D., Frederick, L.M., Von Loehneysen, K., Dinauer, M.C., and Knaus, U.G., *Functional analysis of Nox4 reveals unique characteristics compared to other NADPH oxidases*. Cell Signal, 2006. **18**(1): p. 69-82.
133. Mason, N.A., Springall, D.R., Burke, M., Pollock, J., Mikhail, G., Yacoub, M.H., and Polak, J.M., *High expression of endothelial nitric oxide synthase in plexiform lesions of pulmonary hypertension*. J Pathol, 1998. **185**(3): p. 313-8.
134. Massart, C., Hoste, C., Virion, A., Ruf, J., Dumont, J.E., and Van Sande, J., *Cell biology of H2O2 generation in the thyroid: investigation of the control of dual oxidases (DUOX) activity in intact ex vivo thyroid tissue and cell lines*. Mol Cell Endocrinol, 2011. **343**(1-2): p. 32-44.

135. Matsumoto, H., Suzuki, N., Onda, H., and Fujino, M., *Abundance of endothelin-3 in rat intestine, pituitary gland and brain*. *Biochem Biophys Res Commun*, 1989. **164**(1): p. 74-80.
136. Mcgoon, M.D. and Kane, G.C., *Pulmonary hypertension: diagnosis and management*. *Mayo Clin Proc*, 2009. **84**(2): p. 191-207.
137. Medarov, B.I. and Judson, M.A., *The role of calcium channel blockers for the treatment of pulmonary arterial hypertension: How much do we actually know and how could they be positioned today?* *Respir Med*, 2015. **109**(5): p. 557-64.
138. Meitzler, J.L., Antony, S., Wu, Y., Juhasz, A., Liu, H., Jiang, G., Lu, J., Roy, K., and Doroshov, J.H., *NADPH oxidases: a perspective on reactive oxygen species production in tumor biology*. *Antioxid Redox Signal*, 2014. **20**(17): p. 2873-89.
139. Mitchell, J.A., Ahmetaj-Shala, B., Kirkby, N.S., Wright, W.R., Mackenzie, L.S., Reed, D.M., and Mohamed, N., *Role of prostacyclin in pulmonary hypertension*. *Glob Cardiol Sci Pract*, 2014. **2014**(4): p. 382-93.
140. Mittal, M., Roth, M., Konig, P., Hofmann, S., Dony, E., Goyal, P., Selbitz, A.C., Schermuly, R.T., Ghofrani, H.A., Kwapiszewska, G., Kummer, W., Klepetko, W., Hoda, M.A., Fink, L., Hanze, J., Seeger, W., Grimminger, F., Schmidt, H.H., and Weissmann, N., *Hypoxia-dependent regulation of nonphagocytic NADPH oxidase subunit NOX4 in the pulmonary vasculature*. *Circ Res*, 2007. **101**(3): p. 258-67.
141. Movafagh, S., Crook, S., and Vo, K., *Regulation of hypoxia-inducible factor-1 α by reactive oxygen species: new developments in an old debate*. *J Cell Biochem*, 2015. **116**(5): p. 696-703.
142. Mruk, D.D. and Cheng, C.Y., *Enhanced chemiluminescence (ECL) for routine immunoblotting: An inexpensive alternative to commercially available kits*. *Spermatogenesis*, 2011. **1**(2): p. 121-122.
143. Nagaoka, T., Muramatsu, M., Sato, K., Mcmurtry, I., Oka, M., and Fukuchi, Y., *Mild hypoxia causes severe pulmonary hypertension in fawn-hooded but not in Tester Moriyama rats*. *Respir Physiol*, 2001. **127**(1): p. 53-60.
144. Nakano, Y., Longo-Guess, C.M., Bergstrom, D.E., Nauseef, W.M., Jones, S.M., and Banfi, B., *Mutation of the Cyba gene encoding p22phox causes vestibular and immune defects in mice*. *J Clin Invest*, 2008. **118**(3): p. 1176-85.
145. Noble, P.B., Cutts, J.H., and Carroll, K.K., *Ficoll flotation for the separation of blood leukocyte types*. *Blood*, 1968. **31**(1): p. 66-73.
146. Norel, X., De Montpreville, V., and Brink, C., *Vasoconstriction induced by activation of EP1 and EP3 receptors in human lung: effects of ONO-AE-248, ONO-DI-004, ONO-8711 or ONO-8713*. *Prostaglandins Other Lipid Mediat*, 2004. **74**(1-4): p. 101-12.
147. Nozik-Grayck, E., Huang, Y.C., Carraway, M.S., and Piantadosi, C.A., *Bicarbonate-dependent superoxide release and pulmonary artery tone*. *Am J Physiol Heart Circ Physiol*, 2003. **285**(6): p. H2327-35.
148. Ott, M., Gogvadze, V., Orrenius, S., and Zhivotovsky, B., *Mitochondria, oxidative stress and cell death*. *Apoptosis*, 2007. **12**(5): p. 913-22.
149. Pawlus, M.R., Wang, L., and Hu, C.J., *STAT3 and HIF1 α cooperatively activate HIF1 target genes in MDA-MB-231 and RCC4 cells*. *Oncogene*, 2014. **33**(13): p. 1670-9.
150. Petry, A., *Characterization of novel NADPH oxidases in endothelial cells under basal and stress conditions*, in *Fakultät für Chemie und Pharmazie der Ludwig-Maximilians-Universität München*. 2009, LMU: Munich.
151. Petry, A., Weitnauer, M., and Gorch, A., *Receptor activation of NADPH oxidases*. *Antioxid Redox Signal*, 2010. **13**(4): p. 467-87.

152. Phaniendra, A., Jestadi, D.B., and Periyasamy, L., *Free radicals: properties, sources, targets, and their implication in various diseases*. Indian J Clin Biochem, 2015. **30**(1): p. 11-26.
153. Pollock, D.M. and Schneider, M.P., *Clarifying endothelin type B receptor function*. Hypertension, 2006. **48**(2): p. 211-2.
154. Pugh, C.W. and Ratcliffe, P.J., *The von Hippel-Lindau tumor suppressor, hypoxia-inducible factor-1 (HIF-1) degradation, and cancer pathogenesis*. Semin Cancer Biol, 2003. **13**(1): p. 83-9.
155. Qutub, A.A. and Popel, A.S., *Reactive oxygen species regulate hypoxia-inducible factor 1alpha differentially in cancer and ischemia*. Mol Cell Biol, 2008. **28**(16): p. 5106-19.
156. Raica, M. and Cimpean, A.M., *Platelet-Derived Growth Factor (PDGF)/PDGF Receptors (PDGFR) Axis as Target for Antitumor and Antiangiogenic Therapy*. Pharmaceuticals (Basel), 2010. **3**(3): p. 572-599.
157. Rathore, R., Zheng, Y.M., Niu, C.F., Liu, Q.H., Korde, A., Ho, Y.S., and Wang, Y.X., *Hypoxia activates NADPH oxidase to increase [ROS]i and [Ca2+]i through the mitochondrial ROS-PKCepsilon signaling axis in pulmonary artery smooth muscle cells*. Free Radic Biol Med, 2008. **45**(9): p. 1223-31.
158. Ray, P.D., Huang, B.W., and Tsuji, Y., *Reactive oxygen species (ROS) homeostasis and redox regulation in cellular signaling*. Cell Signal, 2012. **24**(5): p. 981-90.
159. Sada, K., Nishikawa, T., Kukidome, D., Yoshinaga, T., Kajihara, N., Sonoda, K., Senokuchi, T., Motoshima, H., Matsumura, T., and Araki, E., *Hyperglycemia Induces Cellular Hypoxia through Production of Mitochondrial ROS Followed by Suppression of Aquaporin-1*. PLoS One, 2016. **11**(7): p. e0158619.
160. Sara Gargiulo, A.G., Matteo Gramanzini, Silvia Esposito, Andrea Affuso, Arturo Brunetti, Giancarlo Vesce. *Mice Anesthesia, Analgesia, and Care, Part I: Anesthetic Considerations in Preclinical Research*. 2018 [cited 2018 13 March]; Available from: <http://nas-sites.org/ilarjournal/previous-issues/neurobiology-of-addictive-behaviors/mice-anesthesia-analgesia-and-care-part-i-anesthetic-considerations-in-preclinical-research/>.
161. Sarkar, M., Niranjana, N., and Banyal, P.K., *Mechanisms of hypoxemia*. Lung India, 2017. **34**(1): p. 47-60.
162. Schaffer, A.A. and Klein, C., *Animal models of human granulocyte diseases*. Hematol Oncol Clin North Am, 2013. **27**(1): p. 129-48, ix.
163. Schieber, M. and Chandel, N.S., *ROS function in redox signaling and oxidative stress*. Curr Biol, 2014. **24**(10): p. R453-62.
164. Semenza, G.L., *Hypoxia-inducible factor 1 and cardiovascular disease*. Annu Rev Physiol, 2014. **76**: p. 39-56.
165. Semenza, G.L., *Hypoxia-inducible factors in physiology and medicine*. Cell, 2012. **148**(3): p. 399-408.
166. Shimoda, L.A. and Laurie, S.S., *Vascular remodeling in pulmonary hypertension*. J Mol Med (Berl), 2013. **91**(3): p. 297-309.
167. Sim, J.Y., *Nitric oxide and pulmonary hypertension*. Korean J Anesthesiol, 2010. **58**(1): p. 4-14.
168. Simonneau, G., Gatzoulis, M.A., Adatia, I., Celermajer, D., Denton, C., Ghofrani, A., Gomez Sanchez, M.A., Krishna Kumar, R., Landzberg, M., Machado, R.F., Olschewski, H., Robbins, I.M., and Souza, R., *Updated clinical classification of pulmonary hypertension*. J Am Coll Cardiol, 2013. **62**(25 Suppl): p. D34-41.
169. Sitbon, O., Humbert, M., Nunes, H., Parent, F., Garcia, G., Herve, P., Rainisio, M., and Simonneau, G., *Long-term intravenous epoprostenol infusion in primary*

- pulmonary hypertension: prognostic factors and survival*. J Am Coll Cardiol, 2002. **40**(4): p. 780-8.
170. Skonieczna, M., Hejmo, T., Poterala-Hejmo, A., Cieslar-Pobuda, A., and Buldak, R.J., *NADPH Oxidases: Insights into Selected Functions and Mechanisms of Action in Cancer and Stem Cells*. Oxid Med Cell Longev, 2017. **2017**: p. 9420539.
171. Sommer, N., Dietrich, A., Schermuly, R.T., Ghofrani, H.A., Gudermann, T., Schulz, R., Seeger, W., Grimminger, F., and Weissmann, N., *Regulation of hypoxic pulmonary vasoconstriction: basic mechanisms*. Eur Respir J, 2008. **32**(6): p. 1639-51.
172. Sorce, S. and Krause, K.H., *NOX enzymes in the central nervous system: from signaling to disease*. Antioxid Redox Signal, 2009. **11**(10): p. 2481-504.
173. Stacher, E., Graham, B.B., Hunt, J.M., Gandjeva, A., Groshong, S.D., McLaughlin, V.V., Jessup, M., Grizzle, W.E., Aldred, M.A., Cool, C.D., and Tuder, R.M., *Modern age pathology of pulmonary arterial hypertension*. Am J Respir Crit Care Med, 2012. **186**(3): p. 261-72.
174. Stasch, J.P. and Evgenov, O.V., *Soluble guanylate cyclase stimulators in pulmonary hypertension*. Handb Exp Pharmacol, 2013. **218**: p. 279-313.
175. Stasia, M.J., *CYBA encoding p22(phox), the cytochrome b558 alpha polypeptide: gene structure, expression, role and physiopathology*. Gene, 2016. **586**(1): p. 27-35.
176. Stenmark, K.R., Fagan, K.A., and Frid, M.G., *Hypoxia-induced pulmonary vascular remodeling: cellular and molecular mechanisms*. Circ Res, 2006. **99**(7): p. 675-91.
177. Stenmark, K.R., Meyrick, B., Galie, N., Mooi, W.J., and Mcmurtry, I.F., *Animal models of pulmonary arterial hypertension: the hope for etiological discovery and pharmacological cure*. Am J Physiol Lung Cell Mol Physiol, 2009. **297**(6): p. L1013-32.
178. Steudel, W., Scherrer-Crosbie, M., Bloch, K.D., Weimann, J., Huang, P.L., Jones, R.C., Picard, M.H., and Zapol, W.M., *Sustained pulmonary hypertension and right ventricular hypertrophy after chronic hypoxia in mice with congenital deficiency of nitric oxide synthase 3*. J Clin Invest, 1998. **101**(11): p. 2468-77.
179. Suliman, H.B., Ali, M., and Piantadosi, C.A., *Superoxide dismutase-3 promotes full expression of the EPO response to hypoxia*. Blood, 2004. **104**(1): p. 43-50.
180. Sun, X. and Kaufman, P.D., *Ki-67: more than a proliferation marker*. Chromosoma, 2018. **127**(2): p. 175-186.
181. Svegliati, S., Canello, R., Sambo, P., Luchetti, M., Paroncini, P., Orlandini, G., Discepoli, G., Paterno, R., Santillo, M., Cuzzo, C., Cassano, S., Avvedimento, E.V., and Gabrielli, A., *Platelet-derived growth factor and reactive oxygen species (ROS) regulate Ras protein levels in primary human fibroblasts via ERK1/2. Amplification of ROS and Ras in systemic sclerosis fibroblasts*. J Biol Chem, 2005. **280**(43): p. 36474-82.
182. Tabima, D.M., Frizzell, S., and Gladwin, M.T., *Reactive oxygen and nitrogen species in pulmonary hypertension*. Free Radic Biol Med, 2012. **52**(9): p. 1970-86.
183. Tabima, D.M., Hacker, T.A., and Chesler, N.C., *Measuring right ventricular function in the normal and hypertensive mouse hearts using admittance-derived pressure-volume loops*. Am J Physiol Heart Circ Physiol, 2010. **299**(6): p. H2069-75.
184. Tang, P., Dang, H., Huang, J., Xu, T., Yuan, P., Hu, J., and Sheng, J.F., *NADPH oxidase NOX4 is a glycolytic regulator through mROS-HIF1alpha axis in thyroid carcinomas*. Sci Rep, 2018. **8**(1): p. 15897.
185. Taraseviciene-Stewart, L., Kasahara, Y., Alger, L., Hirth, P., Mc Mahon, G., Waltenberger, J., Voelkel, N.F., and Tuder, R.M., *Inhibition of the VEGF receptor 2 combined with chronic hypoxia causes cell death-dependent pulmonary endothelial*

- cell proliferation and severe pulmonary hypertension*. FASEB J, 2001. **15**(2): p. 427-38.
186. Thermo Fischer Scientific. *Avidin-Biotin Complex Method for IHC Detection*. 2018 [cited 2018 March 22]; Available from: <https://www.thermofisher.com/de/de/home/life-science/protein-biology/protein-biology-learning-center/protein-biology-resource-library/pierce-protein-methods/avidin-biotin-complex-method-ihc-detection.html#3>.
187. Thomas, D.C., Clare, S., Sowerby, J.M., Pardo, M., Juss, J.K., Goulding, D.A., Van Der Weyden, L., Storisteanu, D., Prakash, A., Espeli, M., Flint, S., Lee, J.C., Hoenderdos, K., Kane, L., Harcourt, K., Mukhopadhyay, S., Umrana, Y., Antrobus, R., Nathan, J.A., Adams, D.J., Bateman, A., Choudhary, J.S., Lyons, P.A., Condliffe, A.M., Chilvers, E.R., Dougan, G., and Smith, K.G., *Eros is a novel transmembrane protein that controls the phagocyte respiratory burst and is essential for innate immunity*. J Exp Med, 2017. **214**(4): p. 1111-1128.
188. Toba, M., Alzoubi, A., O'neill, K.D., Gairhe, S., Matsumoto, Y., Oshima, K., Abe, K., Oka, M., and Mcurmury, I.F., *Temporal hemodynamic and histological progression in Sugen5416/hypoxia/normoxia-exposed pulmonary arterial hypertensive rats*. Am J Physiol Heart Circ Physiol, 2014. **306**(2): p. H243-50.
189. Tuder, R.M., *Pulmonary vascular remodeling in pulmonary hypertension*. Cell Tissue Res, 2017. **367**(3): p. 643-649.
190. Uniprot. *Cytochrome b-245 light chain*. UniProt: a worldwide hub of protein knowledge February 26, 2020 [cited 2020 7 March]; Available from: www.uniprot.org/uniprot/Q61462.
191. Ushio-Fukai, M., *VEGF signaling through NADPH oxidase-derived ROS*. Antioxid Redox Signal, 2007. **9**(6): p. 731-9.
192. Ushio-Fukai, M. and Nakamura, Y., *Reactive oxygen species and angiogenesis: NADPH oxidase as target for cancer therapy*. Cancer Lett, 2008. **266**(1): p. 37-52.
193. Vaziri, N.D. and Wang, Z.Q., *Sustained systemic arterial hypertension induced by extended hypobaric hypoxia*. Kidney Int, 1996. **49**(5): p. 1457-63.
194. Veit, F., Pak, O., Egemazarov, B., Roth, M., Kosanovic, D., Seimetz, M., Sommer, N., Ghofrani, H.A., Seeger, W., Grimminger, F., Brandes, R.P., Schermuly, R.T., and Weissmann, N., *Function of NADPH oxidase 1 in pulmonary arterial smooth muscle cells after monocrotaline-induced pulmonary vascular remodeling*. Antioxid Redox Signal, 2013. **19**(18): p. 2213-31.
195. Veith, C., Kraut, S., Wilhelm, J., Sommer, N., Quanz, K., Seeger, W., Brandes, R.P., Weissmann, N., and Schroder, K., *NADPH oxidase 4 is not involved in hypoxia-induced pulmonary hypertension*. Pulm Circ, 2016. **6**(3): p. 397-400.
196. Visovatti, S.H., Hyman, M.C., Goonewardena, S.N., Anyanwu, A.C., Kanthi, Y., Robichaud, P., Wang, J., Petrovic-Djergovic, D., Rattan, R., Burant, C.F., and Pinsky, D.J., *Purinergic dysregulation in pulmonary hypertension*. Am J Physiol Heart Circ Physiol, 2016. **311**(1): p. H286-98.
197. Vitali, S.H., Hansmann, G., Rose, C., Fernandez-Gonzalez, A., Scheid, A., Mitsialis, S.A., and Kourembanas, S., *The Sugen 5416/hypoxia mouse model of pulmonary hypertension revisited: long-term follow-up*. Pulm Circ, 2014. **4**(4): p. 619-29.
198. Voelkel, N.F. and Tuder, R.M., *Hypoxia-induced pulmonary vascular remodeling: a model for what human disease?* J Clin Invest, 2000. **106**(6): p. 733-8.
199. Volpe, C.M.O., Villar-Delfino, P.H., Dos Anjos, P.M.F., and Nogueira-Machado, J.A., *Cellular death, reactive oxygen species (ROS) and diabetic complications*. Cell Death Dis, 2018. **9**(2): p. 119.

200. Von Lohneysen, K., Noack, D., Jesaitis, A.J., Dinauer, M.C., and Knaus, U.G., *Mutational analysis reveals distinct features of the Nox4-p22 phox complex*. J Biol Chem, 2008. **283**(50): p. 35273-82.
201. Von Lohneysen, K., Noack, D., Wood, M.R., Friedman, J.S., and Knaus, U.G., *Structural insights into Nox4 and Nox2: motifs involved in function and cellular localization*. Mol Cell Biol, 2010. **30**(4): p. 961-75.
202. Wagner, E.M., *Monitoring gene expression: quantitative real-time rt-PCR*. Methods Mol Biol, 2013. **1027**: p. 19-45.
203. Wang, S., Ji, L.Y., Li, L., and Li, J.M., *Oxidative stress, autophagy and pyroptosis in the neovascularization of oxygeninduced retinopathy in mice*. Mol Med Rep, 2019. **19**(2): p. 927-934.
204. Wang, X., Pinto-Duarte, A., Sejnowski, T.J., and Behrens, M.M., *How Nox2-containing NADPH oxidase affects cortical circuits in the NMDA receptor antagonist model of schizophrenia*. Antioxid Redox Signal, 2013. **18**(12): p. 1444-62.
205. Wang, Z., Schreier, D.A., Hacker, T.A., and Chesler, N.C., *Progressive right ventricular functional and structural changes in a mouse model of pulmonary arterial hypertension*. Physiol Rep, 2013. **1**(7): p. e00184.
206. Waris, G. and Ahsan, H., *Reactive oxygen species: role in the development of cancer and various chronic conditions*. J Carcinog, 2006. **5**: p. 14.
207. Wei, H. and Cong, X., *The effect of reactive oxygen species on cardiomyocyte differentiation of pluripotent stem cells*. Free Radic Res, 2018. **52**(2): p. 150-158.
208. Wijeratne, D.T., Lajkosz, K., Brogly, S.B., Lougheed, M.D., Jiang, L., Housin, A., Barber, D., Johnson, A., Doliszny, K.M., and Archer, S.L., *Increasing Incidence and Prevalence of World Health Organization Groups 1 to 4 Pulmonary Hypertension: A Population-Based Cohort Study in Ontario, Canada*. Circ Cardiovasc Qual Outcomes, 2018. **11**(2): p. e003973.
209. Wilson, D.W., Segall, H.J., Pan, L.C., and Dunston, S.K., *Progressive inflammatory and structural changes in the pulmonary vasculature of monocrotaline-treated rats*. Microvasc Res, 1989. **38**(1): p. 57-80.
210. Wong, C.M., Bansal, G., Pavlickova, L., Marcocci, L., and Suzuki, Y.J., *Reactive oxygen species and antioxidants in pulmonary hypertension*. Antioxid Redox Signal, 2013. **18**(14): p. 1789-96.
211. Xiao, Y., Peng, H., Hong, C., Chen, Z., Deng, X., Wang, A., Yang, F., Yang, L., Chen, C., and Qin, X., *PDGF Promotes the Warburg Effect in Pulmonary Arterial Smooth Muscle Cells via Activation of the PI3K/AKT/mTOR/HIF-1alpha Signaling Pathway*. Cell Physiol Biochem, 2017. **42**(4): p. 1603-1613.
212. Xue, C. and Johns, R.A., *Endothelial nitric oxide synthase in the lungs of patients with pulmonary hypertension*. N Engl J Med, 1995. **333**(24): p. 1642-4.
213. Yu, A.Y., Shimoda, L.A., Iyer, N.V., Huso, D.L., Sun, X., McWilliams, R., Beaty, T., Sham, J.S., Wiener, C.M., Sylvester, J.T., and Semenza, G.L., *Impaired physiological responses to chronic hypoxia in mice partially deficient for hypoxia-inducible factor 1alpha*. J Clin Invest, 1999. **103**(5): p. 691-6.
214. Yu, B., Meng, F., Yang, Y., Liu, D., and Shi, K., *NOX2 Antisense Attenuates Hypoxia-Induced Oxidative Stress and Apoptosis in Cardiomyocyte*. Int J Med Sci, 2016. **13**(8): p. 646-52.
215. Zhang, Z., Trautz, B., Kracun, D., Vogel, F., Weitnauer, M., Hochkogler, K., Petry, A., and Gorlach, A., *Stabilization of p22phox by Hypoxia Promotes Pulmonary Hypertension*. Antioxid Redox Signal, 2019. **30**(1): p. 56-73.
216. Zhao, X., Ho, D., Gao, S., Hong, C., Vatner, D.E., and Vatner, S.F., *Arterial Pressure Monitoring in Mice*. Curr Protoc Mouse Biol, 2011. **1**: p. 105-122.

217. Ziello, J.E., Jovin, I.S., and Huang, Y., *Hypoxia-Inducible Factor (HIF)-1 regulatory pathway and its potential for therapeutic intervention in malignancy and ischemia*. Yale J Biol Med, 2007. **80**(2): p. 51-60.
218. Zuo, L., Rose, B.A., Roberts, W.J., He, F., and Banes-Berceli, A.K., *Molecular characterization of reactive oxygen species in systemic and pulmonary hypertension*. Am J Hypertens, 2014. **27**(5): p. 643-50.

7. Appendix

7.1. List of figures

Figure 1 Pathways involved in the development of pulmonary hypertension	11
Figure 2 Reaction of ROS	18
Figure 3 Structure of phagocyte NADPH oxidase complex	19
Figure 4 Schematic overview of the functional NOX domains	20
Figure 5 Y121H point mutation in NMF333 mice	51
Figure 6 Genotyping results of NMF33	52
Figure 7 Schematic illustration of the "knockout-first" allele	53
Figure 8 Genotyping results of NOX1-K.O. mice	54
Figure 9 Pressure curves as displayed in Haemodyn Software	58
Figure 10 Density based PBMC purification	61
Figure 11 Autoradiography of mouse organs	63
Figure 12 Schematic illustration of the ABC-staining method	72
Figure 13 Hypoxia decreases p22phox mRNA levels in mESC	77
Figure 14 Hypoxia increases p22phox protein levels	78
Figure 15 The Y121H mutation does not affect p22phox mRNA levels	79
Figure 16 P22phox protein levels are reduced in different organs from NMF333 mice	80
Figure 17 Basal superoxide generation is decreased in NMF333 peripheral blood mononuclear cells	81
Figure 18 Vessel forming capacity is reduced in NMF333 mice	82
Figure 19 P22phox mRNA levels are not affected by hypoxia or the Y121H mutation	84
Figure 20 Hypoxic induction of p22phox protein is reduced in NMF333 mice	85
Figure 21 NMF333 mice do not develop hypoxia-induced pulmonary hypertension ..	87
Figure 22 Hypoxic induction of right ventricular mass is reduced in NMF333 mice ..	89
Figure 23 Right ventricular wall thickness is reduced in hypoxic NMF333 mice	90
Figure 24 Hypoxic increase in cardiomyocyte diameter is reduced in NMF333 mice .	91
Figure 25 Hypertrophy associated gene expression in right ventricles of wildtype and NMF333 mice	92
Figure 26 Hypoxia- induced pulmonary vascular remodelling is diminished in NMF333 mice	94

Figure 27 Ki67 staining is reduced in small muscularized vessels in hypoxic NMF333 mice	95
Figure 28 ¹⁸F-FDG uptake is reduced in lungs of hypoxic NMF333 mice	96
Figure 29 Hypoxia does not affect HIF1α mRNA levels	98
Figure 30 HIF1α protein levels are induced by hypoxia	99
Figure 31 HIF1α mRNA expression is not influenced by chronic hypoxia or the Y121H mutation in the lung and right ventricle	100
Figure 32 Hypoxic upregulation of HIF1α is diminished in NMF333 mice	101
Figure 33 Depletion of p22phox decreases hypoxic induction of HIF1 target genes in hypoxic HMEC-1	102
Figure 34 NOX1-K.O. mice are not protected against hypoxia-induced pulmonary hypertension	103
Figure 35 NOX1 K.O. mice develop hypoxia-induced right ventricular hypertrophy	104
Figure 36 Hypoxia-induced pulmonary vascular remodelling is not affected in NOX1-K.O. mice	105
Figure 37 Illustration of the suggested pathway	110

7.2. List of abbreviations

AA	Arachidonic acid	GRx	Glutathione-reductase
ARNT	aryl hydrocarbon receptor nuclear translocator	GSH	Glutathione
ATP	Adenosine triphosphate	GSSG	Glutathione disulphide
Bp	Base pair	GTP	Guanosine triphosphate
BSA	Bovine serum albumin	HBG	haemoglobin
BW	Bodyweight	HCT	haematocrit
cAMP	Cyclic adenosine monophosphate	H&E	Haematoxylin and Eosin
cDNA	Complementary DNA	HIER	Heat induced epitope retrieval
CGD	chronic granulomatous disease	HIF	Hypoxia-inducible factor
cGMP	Cyclic guanosine monophosphate	HIF1 α	Hypoxia-inducible factor 1 α
COX	Cyclooxygenase	HMEC	Human microvascular endothelial cells
CTEPH	Chronic thromboembolic pulmonary hypertension	HPF	High power field
CYP	cytochrome	HRP	Horseradish peroxidase
Dias	Diastolic	HX	Hypoxia
DMSO	Dimethyl sulfoxide	K.O.	Knockout
DMPO	5,5-Dimethyl-1-pyrroline N-oxidase	LV	Left ventricle
DNA	Deoxyribonucleic acid	LVP	Left ventricular pressure
DPG	Diastolic pulmonary vascular pressure gradient	m	Mass
ECL	enhanced chemiluminescence	MAP	Mean arterial pressure
EDTA	Ethylenediaminetetraacetic acid	MCH	Mean corpuscular haemoglobin
EGTA	Ethylene glycol-bis(β -aminoethyl ether)- <i>N,N,N',N'</i> -tetraacetic acid	MCHC	Mean corpuscular haemoglobin concentration
eNOS	Endothelial nitric oxide synthase	MCT	Monocrotaline
EPO	Erythropoietin	MCV	Mean corpuscular volume
EPR	Electron paramagnetic resonance	mESC	Mouse embryonic stem cells
ET-1	Endothelin-1	MHC	Myosin heavy chain
FAD	Flavin adenine dinucleotide	miRNA	Micro RNA
FDG	Fludeoxyglucose-18	M.o.M. kit	Mouse on mouse kit
FELASA	Federation for Laboratory Animal Science Associations	mRNA	Messenger RNA
FFPE	formalin fixed paraffin embedded	NADPH	Nicotinamide Adenine Dinucleotide Phosphate Oxidase
Fig.	Figure	NF- κ B	nuclear factor kappa-light-chain-enhancer of activated B cells
FW	Forward	NO	Nitric oxide
GPx	Glutathione-peroxidase	NX	normoxia
		PAH	Pulmonary arterial hypertension
		PAI-1	Plasminogen activator inhibitor Typ 1
		PASMCs	Pulmonary artery smooth muscle cells

List of abbreviations

PAWP	Pulmonary arterial wedge pressure	WBC	white blood count
PBMC	Peripheral blood mononuclear cell	WGA	Wheat germ agglutinin
PBS	Phosphate buffered saline	WU	Wood units
PCR	Poly chain reaction	WT	Wildtype
PDGF	Platelet derived growth factor		
PET	Positron emission tomography		
PGI ₂	Prostaglandin-I ₂		
PGK-1	Phosphoglycerate kinase 1		
PH	Pulmonary hypertension		
PHD	Prolyl hydroxylases		
PLT	Platelets		
PPAR	Proliferator-activated receptor		
pVHL	Von Hippel-Lindau protein		
PVR	Pulmonary vascular resistance		
qPCR	Quantitative PCR		
RBC	red blood count		
RE	restriction enzyme		
RHC	Right heart catheterization		
RNA	Ribonucleic acid		
Rpm	rotations per minute		
ROS	reactive oxygen species		
RT	Room temperature		
RT-PCR	Reverse transcriptase PCR		
RV	right ventricle		
RV primer	Reverse primer		
RVP	right ventricular pressure		
S	Septum		
SD	Standard deviation		
SDS	Sodium dodecyl sulphate		
SEM	Standard error of the mean		
siRNA	Small interfering RNA		
SKA	Skeletal muscle actin		
SOD	Superoxide dismutase		
Sys	systolic		
TAE	Tris-acetic acid-EDTA buffer		
TBS	Tris-buffered saline		
TBST	Tris-buffered saline w. Tween		
TEMED	Tetramethylethylenediamin		
VEGF	Vascular endothelial growth factor		
vs.	versus		
VSMC	Vascular smooth muscle cell		